A STUDY OF IMPROVED OPTICAL SENSING PERFORMANCES BASED ON NANOSCALE POROUS SUBSTRATES

By

Yang Jiao

Dissertation

Submitted to the Faculty of the

Graduate School of Vanderbilt University

in partial fulfillment of the requirements

for the degree of

DOCTOR OF PHILOSOPHY

in

Electrical Engineering

May, 2013

Nashville, Tennessee

Approved:

Prof. Sharon M. Weiss

Prof. Bharat Bhuva

Prof. Daniel M. Fleetwood

Prof. G. Kane Jennings

Prof. Ronald D. Schrimpf

To my family

ACKNOWLEDGEMENTS

This work would not have been possible without the financial support of the National Science Foundation (NSF) and Army Research Office (ARO), the financial and technical support of the Vanderbilt Institute of Nanoscale Science and Engineering (VINSE), and the opportunities to conduct part of the research at the Center for Nanophase Materials Sciences (CNMS) at Oak Ridge National Laboratory (ORNL).

I am grateful to all of those with whom I have had the pleasure to work during my Ph.D study. Each member of my dissertation committee provided professional comments and guidance on this scientific research. I would especially express my gratitude to my academic advisor, Dr. Sharon M. Weiss, for her patience, encouragement, and advice throughout my Ph.D. study. She showed me the qualities and scientific attitude a good scientist should possess. I would also thank Dr. Dmitry Koktyshe of the Department of Chemistry for his scientific insights and pertinent suggestions on some of the experiments. I really appreciate the pleasant cooperation with Dr. John E. Sipe of the University of Toronto and Dr. Marco Liscidini of Università degli Studi di Pavia. I would also like to acknowledge Dr. Nsoki Phambu of the Department of Chemistry of Tennessee State Univeristy for the assistance with SERS microscope.

I have had the pleasure to work with a number of post-docs, graduate students, and undergraduate students during my time at Vanderbilt University. I would especially like to thank Judson Ryckman from the Weiss group who always provided great help and critical technical discussion. I also would like to thank Dr. Peter Ciesielski and Carlos Escobar for the sample preparation and technical discussion. I would like to thank other members of the Weiss Group, past and present, particularly Dr. Guoguang Rong, Dr. Jenifer Lawrie, Dr. Xing Wei, Dr. Jeremy Mares, Shuren Hu, Gilbert Rodriguez, Girija Gaur, Shweta Bhandaru, Yiliang Zhao, and Peter Markov.

Last, I would like to thank my wife for her understanding, endless love and encouragement. Her support and help was in the end to make this dissertation possible. My parents receive my deepest gratitude for love, support and education ever since I was born.

CONTENTS

LIST OF FIGURES

LIST OF TABLES

CHAPTER 1.

INTRODUCTION

1.1 Optical label-free biosensors

Optical biosensors are powerful detection and analysis devices for monitoring environmental changes, the presence of target analytes, and light-matter interaction. They have recently attracted much attention due to their vast applications in biomedical research, water contamination monitoring, and homeland security. Optical signals, such as reflection, transmission, and absorption are utilized as the transduction signal to transform an environmental change to a detectible optical change. There are many advantages of optical biosensors. For example, due to the ability of detecting single photons, optical biosensors can provide ultra high detection sensitivity including single molecule detection. Also, due to the independent, non-interfering operation at different wavelengths, optical biosensors are immune to electromagnetic interference and enable multiplexed detection within a single chip. Generally, optical biosensors can be divided in two categories: fluorescence based detection and label-free detection. In fluorescence based detection, target molecules need to first be tagged with fluorophors/dyes, and the intensity of fluorescence indicates the presence of molecules as well as the binding strength between probe and target molecules.[1] While some fluorescence based sensing platforms demonstrate ultrahigh detection sensitivity down to single-molecule detection,[2] laborious labeling processes are usually required which might limit their practical use beyond a clinical facility with trained personnel. In label-free sensing, on the contrary, target molecules do not need to be altered or labeled so molecules can be directly detected in their original form. Therefore, label-free biosensing is a fast and powerful approach for measuring and analyzing the quantitative as well as kinetic interaction of molecules. In the category of label-free sensing, various detection mechanisms exist such as refractive index, light absorption, near infrared (NIR), and Raman scattering based detection.[1, 3] This thesis will mainly focus on refractive index and Raman scattering based label-free sensing.

1.1.1 Refractive index based (bio)sensing

Refractive index based sensing is one of the most commonly used methods to quantify target molecules. For most label-free biosensors, a strong optical (or electromagnetic) field is located at the sensor surface where most of molecules tend to be immobilized. When molecules are captured on the surface, they interact with the optical field leading to an overall refractive index change within a small region. The refractive index change subsequently leads to a change of the optical transduction signal such as reflection, transmission or scattering spectrum, which can be directly collected by detectors and analyzed. Quantifying the magnitude of the change in the optical spectrum can provide information about molecular surface coverage. By applying specific mathematical models relating to the sensing structures, it is possible to quantify the number of molecules captured by the sensor.[4] In the development of label-free biosensors, strong demand on smaller, faster and more sensitive biosensors has driven enormous progress in the sensing field. One of the most important criteria to evaluate the sensing performance is detection sensitivity, which for optical biosensing is often described as the magnitude of the optical signal change in response to a given refractive index change. Therefore, sensitivity can be quantified by a spectral change per refractive index unit (RIU) change. For example, in the angle interrogation based measurement, the introduction of molecules results in a spectral angular shift. Therefore, detection sensitivity is defined in the unit of degree/RIU. For the wavelength interrogation based measurement, detection sensitivity is defined as nm/RIU where the nm corresponds to the shift in wavelength of a particular spectral feature. Sensitivity can also be described by quantifying a spectral change per number of molecules (in the unit of degree/mole or nm/mole) and detection limit (in the unit of molar)

Refractive index based methods can provide high detection sensitivity. However, the sensing mechanism is based on refractive index change, and therefore cannot provide detailed molecular information for unknown molecules. In order to detect various target molecules, corresponding probe molecules need to be first immobilized on the sensor surface in order to capture specific target molecules. Hence appropriate surface chemistry is necessary to provide selectivity for refractive index-based sensors.

1.1.2 Raman scattering and surface enhanced Raman scattering (SERS)

Unlike refractive index based sensing, Raman scattering is an optical detection method based on inelastic scattering between a photon and a molecule. When the incident photons are scattered from a molecule, most of the scattered photons have the same frequency as the incident photons. This type of elastic scattering process is called the Rayleigh scattering (Figure 1-1). However, there is a very small fraction of scattered photons (approximately 1 out of 10 million photons) that will have different frequencies from the incident photons, which indicates an energy shift. Raman scattering is based on this type of inelastic scattering processes and leads to two possible outcomes: Stokes scattering and anti-Stokes scattering. For the Stokes scattering, molecules absorb energy and emit photons which have lower energy (lower frequency or higher wavelength components) than the incident photons. For the anti-Stokes scattering, molecules lose energy and emit photons with higher energy (higher frequency or lower wavelength components) than the incident photons. This energy shift between an incident and a scattered photon gives information about the energy difference between two vibrational energy states of a molecule as shown in Figure 1-1.

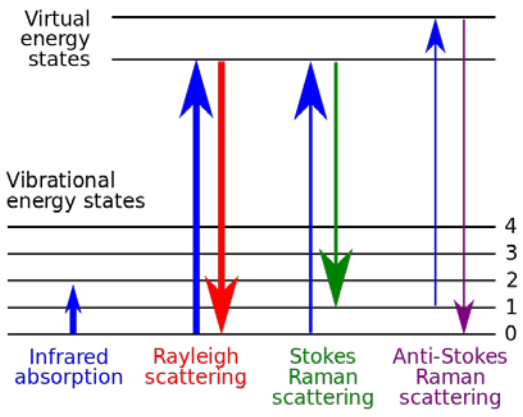

Figure 1-1 Energy level diagram showing principle of Raman scattering

Figure 1-2 shows a typical Raman spectrum of benzenethiol and all the Raman peaks are labeled with red arrows. In the Raman spectrum, peaks appearing at different wave numbers correspond to

different frequency components scattered from a Raman-active molecule due to the presence of different molecular chemical bonds. The energy differences between the incident and scattered photons are determined by the vibrational states of molecular species and therefore can be directly utilized to identify the molecules.[5] Raman spectroscopy is a powerful tool to analyze the composition of molecules and therefore can be incorporated with refractive index based sensing or utilized as an independent technique to provide important molecular information. Raman spectra are commonly called the fingerprints of molecules and have been widely used for uniquely identifying molecules.[6-8] However, because Raman scattering is intrinsically weak, practical use of Raman spectroscopy has been limited.

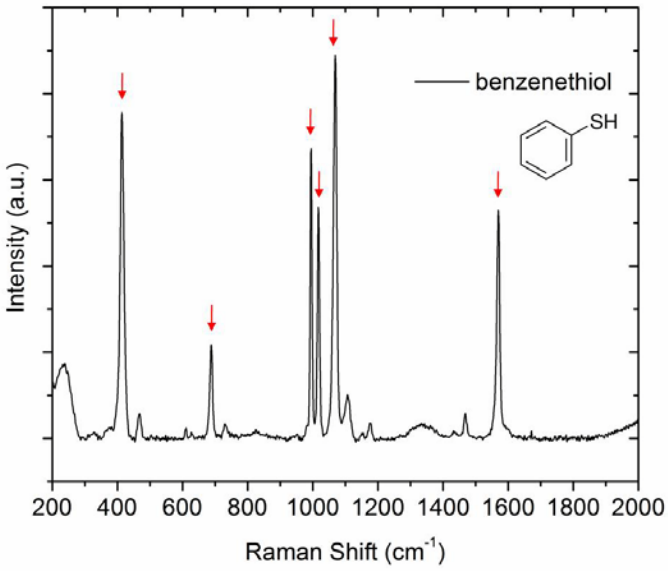

Figure 1-2 Raman spectrum of benzenethiol

Surface enhanced Raman scattering (SERS) is a surface sensitive technique that provides a drastic enhancement in scattering efficiency over traditional Raman scattering, therefore is an excellent platform for low-concentration chemical and biological sensing and has been recently widely investigated.[9] Figure 1-3 shows a typical SERS measurement setup. The enhancement is primarily due to the presence of intense electromagnetic fields, e.g., the plasmonic effect on both incident laser frequency and scattered Raman frequency localized at a rough metal surface where molecules are adsorbed,

although chemical enhancement mechanisms may also play a minor role.[5, 9] In the electromagnetic enhancement mechanism, the SERS enhancement factor (*EF*) can be theoretically described via the following equation

$$EF \propto \frac{\left|E_{loc}(\omega_0)\right|^2 \left|E_{loc}(\omega_s)\right|^2}{\left|E_0(\omega_0)\right|^2 \left|E_0(\omega_s)\right|^2}, \quad (1.\ 1)$$

where ω_0 and ω_s are excitation and Raman scattering frequency respectively, E_0 (ω_0) is the incident electric field with excitation frequency, E_{loc} (ω_0) is the localized electric field at excitation frequency, E_0 (ω_s) is the electric field radiated by the attached molecules at Raman scattered frequency, and E_{loc} (ω_s) is localized electric field at Raman scattered frequency.

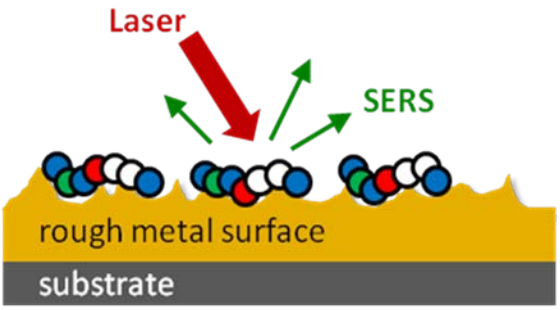

Figure 1-3 Schematic configuration for excitation of SERS at a single interface between a rough metal and a dielectric medium where the colorful circles represent molecules on the rough surface.

Numerous SERS substrates with self-organized metallic nanoscale surface morphologies have been demonstrated to enable high detection sensitivity and even single molecule detection,[8-11] including porous templates coated with metal films, [12, 13] electrochemically roughened metal surfaces,[9, 14] colloidal metal nanoparticles,[15, 16] metal nanoshells,[17, 18] metal nanowires,[19] and nanoporous gold (NPG) films.[20-23] The self-organized substrates achieving the highest SERS intensities rely on highly localized regions with extremely high field concentration that do not occur uniformly across the substrate. Hence, there is a significant challenge for practical use of such substrates since measurements away from these so-called "hot spot" regions yield comparably lower SERS intensities, and thus the ensemble average intensity is

also much lower than the hotspot regions. In contrast to these SERS substrates that are characterized by random structures, highly reproducible nanofabrication techniques have been used to produce SERS substrates that exhibit large enhancement factors at spatially-defined locations, including nanoparticles of various shapes,[24-26] nanogratings,[27, 28] nanodomes,[7] nanoslits,[29] nanobowties,[30, 31] and nanohole arrays.[32, 33] While nanofabricated SERS templates often obviate the need to search for a hot spot, where a maximum in the signal enhancement is observed, the required fabrication processes such as electron beam lithography and reactive ion etching tend to be expensive and time consuming, which limits both the cost-effectiveness and potential for mass production. For the above reasons, fabricating cost-effective and highly reproducible SERS substrates recently has become a topic of critical importance in the sensing field.

1.2 Layered structures in optical label-free sensing

As discussed in section 1.1, most refractive index and SERS based label-free sensors require a strong field to enhance the light matter interaction with molecules. For this purpose, layered structures have been demonstrated to be excellent candidates for the fabrication of optical sensors. These layered optical structures can be easily fabricated with micro-and nanoscale features by using standard deposition, etching, and lithography methods. Most importantly, the band structures of these layered media can be systematically designed and characterized by properly choosing design parameters (e.g., material, dimension, and periodicity). Therefore, the experimentally detected far field optical signal, such as reflection or transmission, as well as the near field distribution of optical waves can be precisely controlled. Figure 1-4 (a) shows a schematic four-layer configuration. Via appropriate choice of thickness and material of each layer, the resonance dip position can be precisely controlled to occur at a specific angle as shown in Figure 1-4 (b), and correspondingly most of the field intensity (the shaded area) can also be confined in a specific layer as shown in Figure 1-4 (c).

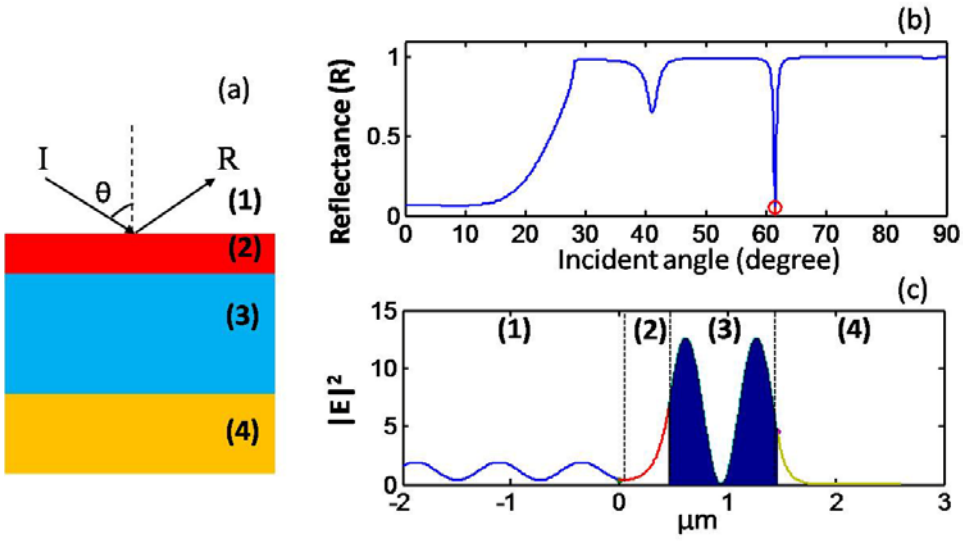

Figure 1-4 (a) A schematic four-layer structure. (b) Far field reflectance spectrum. (c) Near electric field distribution in each layer at resonance angle marked with red spot in (b).

Layered structures play a very important role in a wide variety of applications of modern optics. For example, layered optical structures have been widely utilized for fabricating high performance interferometers,[34] anti-reflectors,[35] filters,[36] modulators,[37] and sensors.[34] In this thesis, the main focus is on the sensing applications of these layered structures, which have been demonstrated to be an effective engineering approach for improving sensor performance. Biosensors based on three simple layered structures including (a) single-layer interferometer, (b) two-layer waveguide, and (c) surface plasmon structures are the focus of this thesis.

1.2.1 Interferometer based biosensors

A single-layer interferometer is the simplest form for layered structures. It utilizes the optical path difference at each interface to generate a sinusoidal reflected/transmitted interference pattern as a function of wavelength or angle. As shown in Figure 1-5 (a), an optical wave is initially incident on the top surface of the film (interface between medium 1 and 2). The incident wave is partially reflected back into medium 1 with refractive index n_1 and partially transmitted to medium 2 with refractive index n_2. The transmitted wave is subsequently reflected back and forth between the top and bottom surfaces of the film, and

therefore any two successive reflected or transmitted waves in medium 1 and 3 experience a different phase change that is directly related to the different optical paths. By considering the phase factor associated with the amplitude of each wave component and adding all the reflected and transmitted waves at the top and bottom surfaces, reflected and transmitted interference patterns in sinusoidal forms can be respectively collected in the far field from medium 1 and 3, as shown in Figure 1-5 (c). In the sensing application, the attachment of molecules on either interferometer surface leads to a different phase change between two successive waves, and thus shifts the interference pattern. The interference pattern shift (from red curve to blue curve) can be subsequently converted to an overall refractive index change and thus used to quantify molecules. Although this single layer interferometer is simple, it does not support strong field confinement. Therefore, single layer interferometric-based sensors are challenged by relatively low sensitivity and broad spectral features that limit the resolution of detection.

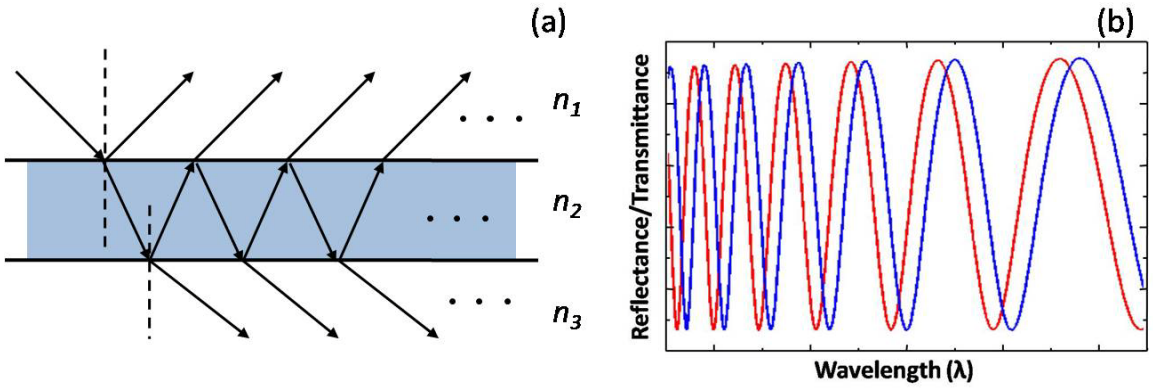

Figure 1-5: (a) Schematic of a single layer interferometer and (b) typical reflectance or transmittance spectra before (red curve) and after (blue curve) the molecule absorption

1.2.2 Waveguide based biosensors

Optical biosensors based on waveguide geometry are explored extensively in this thesis. The waveguide is a specific type of layered structure. Compared to the single layer interferometer structure, typical waveguides consist of a higher refractive index middle or core layer, which is sandwiched between two surrounding lower refractive index cladding layers (i.e. $n_2>n_1$ and $n_2>n_3$). Due to the refractive index contrast between waveguide and cladding layers, light can be confined in the waveguide by total internal

reflection at the interfaces. In order to effectively couple light into the waveguide layer, the incident light needs to be phase-matched to a guided mode, which is different from the above discussed interferometer structure, in which case no phase-matching is required. Essentially, if light is incident on a waveguide from above, it will not be able to couple into a guided mode, regardless of the incident angle. A widely used method to enable coupling of light into the waveguide is to utilize a high index prism, since the tangential component of the incident wave vector can be continuously changed by tuning the incident angle. At the resonance condition, the tangential component of the incident wave vector is equal to the propagation constant of a guided mode, and light is coupled from the prism into the waveguide. Therefore, the wave vector of a guided mode can be calculated via the following equation

$$k_{WG}=k_0 n_p \sin\theta, \quad (1.\ 2)$$

where k_{WG} is the tangential wave vector of a guided mode, k_0 is the wave vector of incident light in free space, n_p is the index of the prism and θ is the resonant angle. The electric field propagates in the waveguide layer and decays exponentially in both cladding layers, which confines the electric field tightly inside the core layer.[38-43] A detailed mathematical formalism to simulate the reflectance and transmittance spectra of these waveguides will be described in section 1.2.4. Figure 1-6 (a, b) show schematic diagrams of optical waveguide structures based on the (a) Otto configuration and (b) Kretschmann configuration, which are the two most common configurations for prism coupling. In the Otto configuration, the layer with higher refractive index acts as the waveguide layer, and air and a second layer with lower refractive index than the waveguide layer act as cladding layers. In the Kretschmann configuration, a low index dielectric or metal layer is deposited directly on the high index prism and acts as a cladding layer. A film with higher refractive index is deposited on top of the cladding layer, and acts as the waveguide layer. Figure 1-6 (c) shows another commonly used coupling method, grating coupling, where the mis-matching between incident light and guided mode is overcome through the higher order diffracted light via periodic gratings. Even though a strongly confined field is associated with a waveguide at the resonance condition, conventional waveguide biosensors can only utilize the evanescent field (or the leaky field) in the

cladding region to interact with molecules immobilized on the waveguide surface, which limits the detection sensitivity since molecules can only interact with a small portion of the strong field. Therefore, waveguide structures with thinner waveguide layers are usually used to enable a greater part of field to leak out to the cladding layer and interact with target molecules.[44]

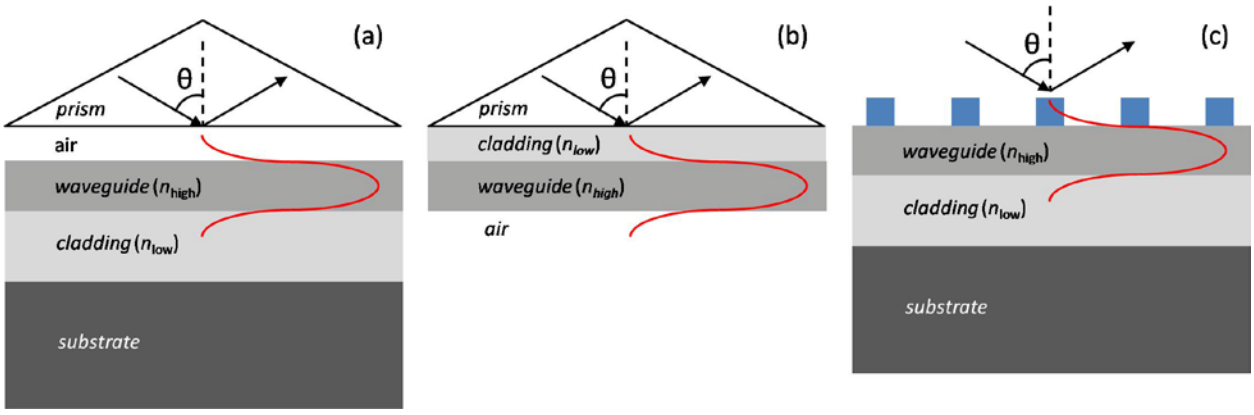

Figure 1-6: Schematic diagrams of waveguides in the (a) Otto configuration and (b) Kretschmann configuration. For both cases, a high refractive index prism is used to couple light into the waveguide layer at a particular resonant angle. (c) Schematic diagram of grating coupled waveguide, where light is coupled into the waveguide layer via the higher order diffraction.

1.2.3 Surface plasmon resonance based biosensors

Surface plasmon resonances (SPR), which are due to surface charge density oscillations at optical frequencies, are evanescently confined waves existing at metal-dielectric interfaces as shown in Figure 1-7. SPR can only be activated under transverse magnetic- (TM) or *p*-polarized light, and can only exist on the surface of noble metals such as gold and silver. The wave vector of a SPR mode only relies on the dielectric constants of two media, which can be described via the following equations:

$$k_{SPR,x} = k_0 \sqrt{\frac{\varepsilon_1 \varepsilon_2}{\varepsilon_1 + \varepsilon_2}}, \tag{1. 3}$$

$$k_{SPR,z} = k_0 \sqrt{\frac{\varepsilon_j^{\,2}}{\varepsilon_1 + \varepsilon_2}}, \quad j = 1, 2. \tag{1. 4}$$

where ε_1 and ε_2 are dielectric constants of the metal and dielectric material, respectively, and k_0, $k_{SPR,x}$, and $k_{SPR,z}$ are the wave vectors of incident light in free space, the tangential component of the SPR mode, and the normal component of the SPR mode in the two media. From the above equations, in order to activate a propagating and vertically confined SPR mode, a real $k_{SPR,x}$ and an imaginary $k_{SPR,x}$ need to be simultaneously satisfied. Therefore, for such a mode to exist, following two conditions need to be simultaneously satisfied:

$$\varepsilon_1 \cdot \varepsilon_2 < 0, \tag{1. 5}$$

$$\varepsilon_1 + \varepsilon_2 < 0. \tag{1. 6}$$

Therefore, only noble metals with a relatively large negative real part (along with a small imaginary part) of the dielectric constant with an absolute value exceeding that of the dielectric material can support the existence of the SPR mode. Analogous to the sensing operation of the conventional evanescent waveguide structure, SPR based biosensors similarly utilize the evanescent field to interact with immobilized molecules on the surface (represented by red dots in Figure 1-7); however, molecules can interact with the strongest part of electromagnetic field at the surface. Since the first SPR based biosensor was demonstrated by Liedberg in 1983,[45] numerous SPR based biosensors have been explored and commercialized[46-48] and it has already become one of the most widely used sensing platforms due to the straightforward fabrication and molecule immobilization.

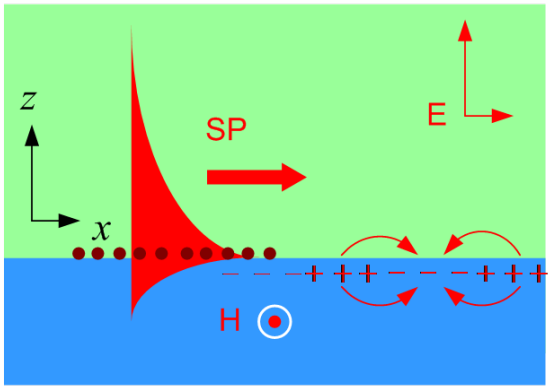

Figure 1-7 Schematic diagram of surface plasmon resonance (SPR) at a metal-dielectric interface.

The activation of SPR requires phase matching between the incident wave and SPR mode. Similar to light coupling to the waveguide mode, light coupling to the SPR mode can also be achieved via a high index prism associated with either the Otto or Kretschmann configuration, as shown in Figure 1-8 (a, b). Figure 1-8 (c) shows an integrated grating coupling method, where the phase mismatch is overcome by a periodic grating structure if the wave vector of higher order diffracted light matches the wave vector of the SPR. However, similar to the conventional waveguide structure, light-matter interaction between the light and target molecules is still not optimal. Even though molecules can interact with the peak field, the surface-attached molecules only interact with a small fraction of the overall confined strong field.

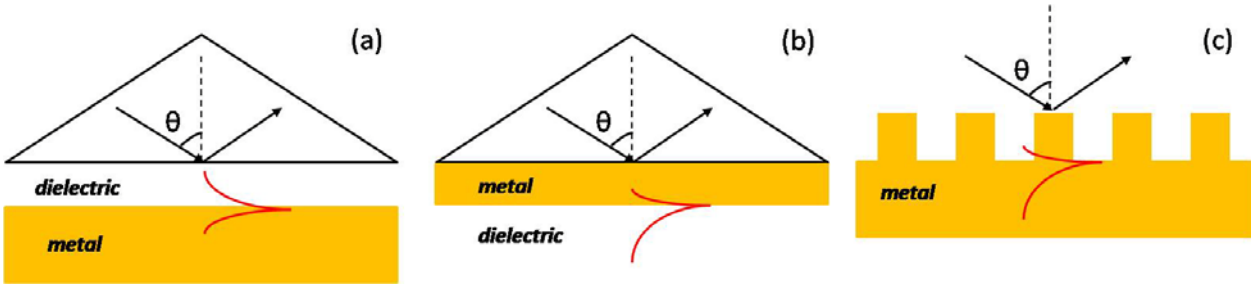

Figure 1-8 Schematic diagrams of prism-coupled SPR structure in (a) Otto configuration and (b) Kretschmann configuration. For both cases, a high refractive index prism is used to couple the light into a SPR mode at the metal surface at particular resonant angles. (c) Schematic diagram of grating-coupled SPR structure.

1.2.4 Modeling methods

1.2.4.1 Matrix formulation

A well-known method for modeling layered structures is the matrix formulation method, which is based on Maxwell's equations and boundary continuity conditions. In this method, each layer is uniquely described by a 2×2 matrix that contains information about the thickness and complex refractive index of the layer.[49] The matrix-based method is especially powerful when the number of layers being considered becomes large, e.g., for periodic multilayer structures. Compared to applying Fresnel's formulas, the matrix-based method is more systematic and does not involve a large number of complicated equations for multilayer structures. Moreover, computer programs such as MATLAB can be used to handle the matrix algebra to calculate the electromagnetic field within each layer as well as the overall reflection and transmission of the structure.

Figure 1-9 shows a unit calculation cell of an arbitrary multilayer structure. The unit cell consists of a layer with refractive index n_2 and finite thickness d sandwiched between two infinitely thick layers with refractive index n_1 and n_3, respectively. As an example, we assume that the light is transverse electric (TE) or *s*-polarized ($E \parallel$ y), and the electric field E(x) in each layer can be described as a superposition of a right-propagating wave $A(x)$ and a left-propagating wave $B(x)$. Therefore the electric field in each layer can be written in the form of

$$E_y(x) = Ae^{-ik_x x} + Be^{ik_x x} \equiv A(x) + B(x), \tag{1. 7}$$

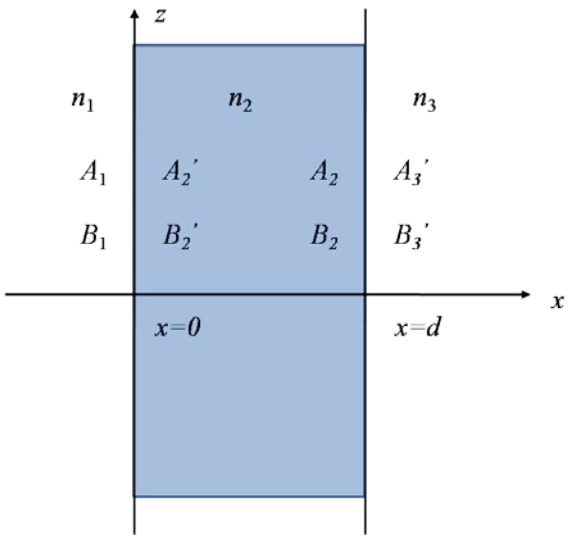

Figure 1-9 Unit cell of a multilayer structure

where *A* and *B* are the amplitudes of the electric field of the propagating waves. Based on Maxwell's equations, the magnetic field *H* can be calculated from

$$\vec{H} = \frac{i}{\omega\mu}\nabla \times \vec{E} \cdot \tag{1. 8}$$

Therefore, after plugging the electric field into Eq. (1.8) the tangential component (*z* component) of magnetic field can be described as

$$H_z(x) = -ik_x A e^{-ik_x x} + ik_x B e^{ik_x x} \cdot \tag{1. 9}$$

After applying the continuity conditions, that tangential electric field and magnetic field are both continuous at interfaces, the following two equations are satisfied at the interface, *x*=0.

$$A_1 + B_1 = A_2^{'} + B_2^{'}, \tag{1. 10}$$

$$-ik_{1x}A_1 + ik_{1x}B_1 = -ik_{2x}A_2^{'} + ik_{2x}B_2^{'}, \tag{1. 11}$$

where *A'* and *B'* are the electric amplitude on the right side of the same interface. These two equations can be also written in the form of a matrix equation

$$\begin{pmatrix} 1 & 1 \\ -ik_{1x} & ik_{1x} \end{pmatrix}\begin{pmatrix} A_1 \\ B_1 \end{pmatrix}=\begin{pmatrix} 1 & 1 \\ -ik_{2x} & ik_{2x} \end{pmatrix}\begin{pmatrix} A_2' \\ B_2' \end{pmatrix}. \tag{1. 12}$$

Therefore, the amplitudes of the electric field on each side of interface are related by Eq. (1.13)

$$\begin{pmatrix} A_1 \\ B_1 \end{pmatrix}=D_{12}\begin{pmatrix} A_2' \\ B_2' \end{pmatrix}, \tag{1. 13}$$

with a transmission matrix D_{12} at the interface from medium 1 to 2 (x=0) defined in Eq. (1.14)

$$D_{12}=\begin{pmatrix} 1 & 1 \\ -ik_{1x} & ik_{1x} \end{pmatrix}^{-1}\begin{pmatrix} 1 & 1 \\ -ik_{2x} & ik_{2x} \end{pmatrix}=\frac{1}{2}\begin{pmatrix} 1+\frac{k_{2x}}{k_{1x}} & 1-\frac{k_{2x}}{k_{1x}} \\ 1-\frac{k_{2x}}{k_{1x}} & 1+\frac{k_{2x}}{k_{1x}} \end{pmatrix}. \tag{1. 14}$$

Similarly, the transmission matrix at the interface from medium 2 to 3 (x=d) can be calculated to be

$$D_{23}=\frac{1}{2}\begin{pmatrix} 1+\frac{k_{3x}}{k_{2x}} & 1-\frac{k_{3x}}{k_{2x}} \\ 1-\frac{k_{1x}}{k_{2x}} & 1+\frac{k_{3x}}{k_{2x}} \end{pmatrix}. \tag{1. 15}$$

Next, both $A(x)$ and $B(x)$ propagating through the bulk of the layer with finite thickness d experiences a phase change of $\phi=k_{nx}d_n$, which is directly related to the refractive index and thickness of that layer. In the unit calculation cell, the two amplitudes of the electric field before and after traveling through the middle layer can be related via Eq (1.16)

$$\begin{pmatrix} A_2' \\ B_2' \end{pmatrix}=P_2\begin{pmatrix} A_2 \\ B_2 \end{pmatrix}, \tag{1. 16}$$

with propagation matrix P defined as

$$P_2=\begin{pmatrix} e^{i\phi_2} & 0 \\ 0 & e^{-i\phi_2} \end{pmatrix}. \tag{1. 17}$$

Based on Eqs. (1.13) - (1.17), the amplitudes in the incident region A_1, B_1 and the output region A_3', B_3' in the calculation cell are related by Eq. (1.18)

$$\begin{pmatrix} A_1 \\ B_1 \end{pmatrix} = D_{12} P_2 D_{23} \begin{pmatrix} A_3' \\ B_3' \end{pmatrix}. \tag{1. 18}$$

The above derivation can be extended to an arbitrary multilayer structure as shown in Figure 1-10

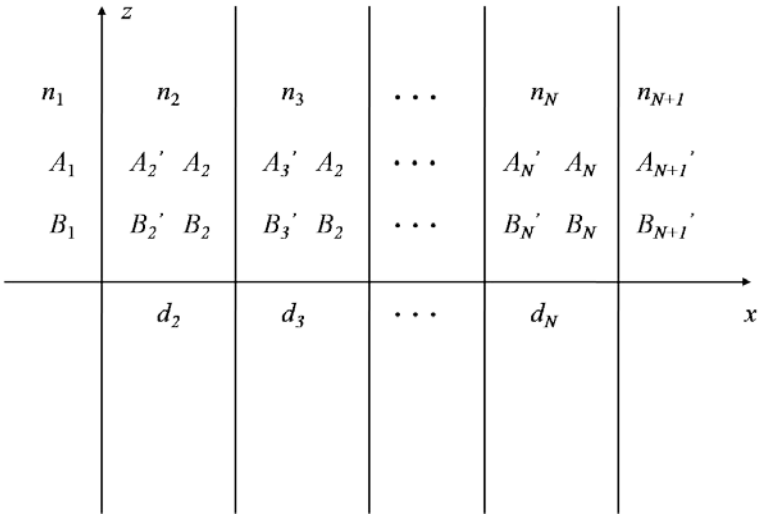

Figure 1-10 Arbitrary multilayer structure for matrix calculations

In the arbitrary multilayer case, the relationship between incident waves A_1, B_1 and output waves A_{N+1}', B_{N+1}' can be straightforwardly related via the multiplication of all the involved calculation cells in the following form

$$\begin{pmatrix} A_1 \\ B_1 \end{pmatrix} = D_{12} P_2 D_{23} P_3 D_{34} P_4 \cdots D_{N-1,N} P_N D_{N,N+1} \begin{pmatrix} A_{N+1}' \\ B_{N+1}' \end{pmatrix} = \begin{pmatrix} M_{11} & M_{12} \\ M_{21} & M_{22} \end{pmatrix} \begin{pmatrix} A_{N+1}' \\ B_{N+1}' \end{pmatrix}, \tag{1. 19}$$

where the matrix **M** is the system matrix describing the entire multilayer structure. From specific components of matrix **M**, the reflection and transmission coefficients can be extracted. Assuming light is incident from medium 1 and output from medium N+1 (i.e. B_{N+1}'=0), the reflection and transmission coefficients can be respectively described as

$$r = \left(\frac{B_1}{A_1} \right)_{B_{N+1}'=0} = \frac{M_{21}}{M_{11}}, \tag{1. 20}$$

$$t = \left(\frac{A_{N+1}'}{A_1} \right)_{B_{N+1}'=0} = \frac{1}{M_{11}}. \tag{1. 21}$$

Reflectance (R) and transmittance (T) are given, respectively, by

$$R = |r|^2 = \left| \frac{M_{21}}{M_{11}} \right|^2, \tag{1. 22}$$

and

$$T = |t|^2 = \left| \frac{1}{M_{11}} \right|^2. \tag{1. 23}$$

1.2.4.2 Rigorous coupled wave analysis (*RCWA*)

As described in section *1.2.4.1*, the matrix formation is an effective method to model horizontally stacked multilayer structures. However, in more complex micro- and nanoscale structures (mainly vertically oriented gratings), diffractive optics will play an important role. Therefore, the matrix formation method is no longer valid for calculating the electromagnetic fields in the grating regions. With the decrease of the grating feature size (e.g. period and width of grating ridge), it is impossible to obtain a general analytical formula to describe all grating structures, therefore a rigorous diffraction theory is required to accurately solve the electromagnetic field in each specific grating structure.

The rigorous coupled wave analysis (RCWA) method is a widely utilized numerical method, which relies on Fourier expansion to solve for the electromagnetic field in a periodic grating structure. Under the assumption that all grating structures are horizontally infinite, the electromagnetic field at each point of grating regions can be Fourier expanded in terms of a series of spatial harmonic components.[50, 51] While an individual spatial harmonic component does not satisfy Maxwell's equations, the sum of harmonic components will satisfy Maxwell's equation as well as the wave equation. In a multilayer system, the overall problem is similarly solved by matching boundary conditions (the tangential electric

and magnetic fields are continuous) at each of the interfaces between the layers. In practical cases, higher order diffraction might need to be cut off depending on the required calculation accuracy and convergence speed.

1.2.4.3 Finite difference time domain (*FDTD*)

The finite difference time domain (FDTD) method is a more accurate and powerful tool for numerically solving Maxwell's equations, which directly solves Maxwell's time dependent curl equations by a recursive algorithm.[52] Compared to the RCWA method, which is only valid for infinite periodic grating structures, the FDTD method is capable of analyzing light interaction in finite and aperiodic structures with wavelength scale features. Typically, the unknown electric and magnetic fields within a region of interest are first sampled into smaller unit cells over a required time period. By applying a time dependent incident electromagnetic field, the near electric and magnetic fields at each cell are repeatedly calculated via solving the finite difference equations. Therefore, the value of the electromagnetic field is updated at each time step. When the steady state is reached, the near field values can be accurately calculated.

In this thesis, the commercial software, Lumerical®, is utilized to perform FDTD simulations. This particular FDTD solution enables the direct import of measured material dispersion curves over wide wavelength ranges via its proprietary multi-coefficient material modeling capabilities, which enables the end user to efficiently and accurately calculate device response over wide bandwidths.

1.3 Nanoscale porous materials in optical biosensing

In order to overcome the limitations of bulk layered structures for biosensing, as discussed in section 1.2, and to further improve sensing performance, an increased surface area available for molecular binding is needed. For this purpose, porous dielectric and metallic materials are promising candidates for label-free sensing, and in particular for small molecule detection, due to their large available surface area[4, 34, 46, 53-55] for molecular binding, which is often >100 m^2/cm^2, and tunable pore diameters that enable size-selective molecule filtering. Molecular binding events inside the pores are often detected optically by monitoring thin film interference patterns using spectral reflectance,[56] waveguide resonances using angle-resolved

reflectance,[53, 54] or microcavity emission peaks using photoluminescence measurements.[57] In addition, unique identification of molecules is possible for sensors based on porous metals or porous materials that incorporate metal nanoparticles by measuring a surface enhanced Raman scattering (SERS) spectrum.[12, 13, 58, 59] While numerous porous materials have been utilized for sensing applications, including porous alumina,[40, 43, 60] porous titania,[38, 55] and porous silica,[61] this thesis will focus exclusively on porous silicon and porous gold films.

1.3.1 Porous silicon (PSi)

Porous silicon (PSi), as a cost-effective and easy-to-fabricate material, have been widely used for numerous applications including light emitting diodes (LEDs),[62] swithes,[63] and photodetectors.[64] Acting as a host material, PSi is an excellent material for biosensing due to the ease of tuning its pore depth, pore morphology, and pore diameter, which can range from micropores (<2 nm) to macropores (>50 nm), through straightforward tuning of the electrochemical etching parameters.[54, 65, 66] For example, the pore depth can be accurately controlled by the etching time and the porosity can be adjusted by applying different current densities. Figure 1-11 demonstrates the formation process of PSi. During electrochemical etching, the charge carriers in the silicon wafer and Fluorine ions (F^-) in the electrolyte meet at the silicon surface. Assisted by charged carriers in the silicon wafer, corrosion of silicon begins when one F^- replaces one hydrogen atom (H) bound to the silicon atom to form Si-F bond. The formed Si-F bond leads to a polarization effect allowing a second F^- to continue to attack and bind to silicon, and hydrogen gas (H_2) is generated. After all four bonds of a silicon atom are broken, the silicon atom becomes soluble in solution as SiF_6^{2-}, leaving behind an atomic vacancy. Note that the etching process is highly directional, and pores propagate preferentially into the silicon substrate from the pore tips where the electric field is strongest. Lateral etching is minimized because charge carriers become depleted between etched pores. Detailed descriptions of pore formation mechanisms can be found elsewhere.[67-69] The pore morphology can be tuned through appropriate choice of silicon substrate doping and applied current density during etching.

Top and side view of scanning electron microscopy (SEM) images of a typical single layer n-type PSi sample is shown in Figure 1-12.

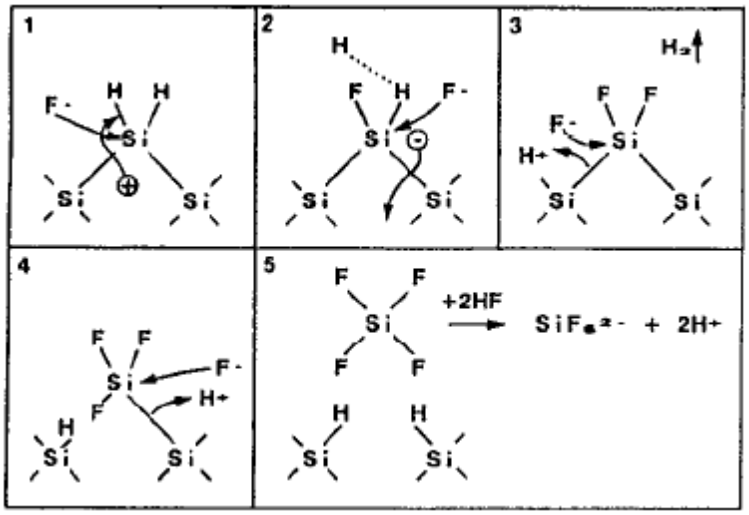

Figure 1-11 Dissolution mechanism of silicon electrodes in HF associated with PSi formation.(Adapted from Ref. [68])

Based on the characterizations of porosity and etching rate performed on single layer PSi samples, multiple layer PSi structures with appropriately designed dimensions for each layer can be straightforwardly fabricated. The formation of a new porous silicon layer beneath an existing porous silicon layer does not affect the properties of the previously etched layer. PSi films can also be straightforwardly removed from the silicon substrate to form a free standing membrane via applying a series of high current pulses in a short time period with appropriate current duty cycle.[4] The high current creates very high porosity porous silicon at the etch front, which becomes detached from the substrate as the porosity approaches 100%.

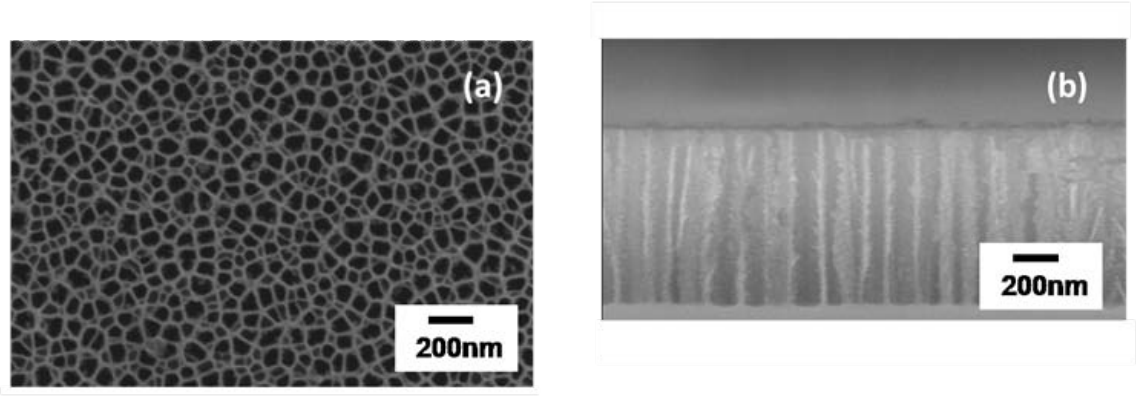

Figure 1-12 (a) Top and (b) cross-sectional SEM images of a typical n-type PSi sample. The dark regions are void space and the bright regions are the silicon pore walls.

1.3.2 Nanoporous gold (NPG)

Nanoporous gold (NPG) films consisting of unique 3D nanoscale sponge-like pore structures have been widely utilized for variety of research areas such as large area electrodes for immobilization of photosystem I in a photovoltaic device[70] and hybrid electrodes for electrochemical supercapcitors.[71] NPG films have also been demonstrated to be an excellent surface enhanced Raman scattering (SERS) substrates, as discussed further in Chapter 5, due to their self-organized and highly interacting nanoscale metal morphology.[20-22] Measured in the Kretschmann configuration, NPG films also have been reported to support both a propagating surface plasmon resonance (SPR) and a localized surface plasmon resonance (LSPR),[21, 72, 73] which can be exploited to achieve improved molecular detection sensitivity compared to conventional SPR sensors due to the enhanced mode overlap between SPR mode and the attached molecules.[46, 74] Top and side view SEM images of a typical NPG sample are shown in Figure 1-13.

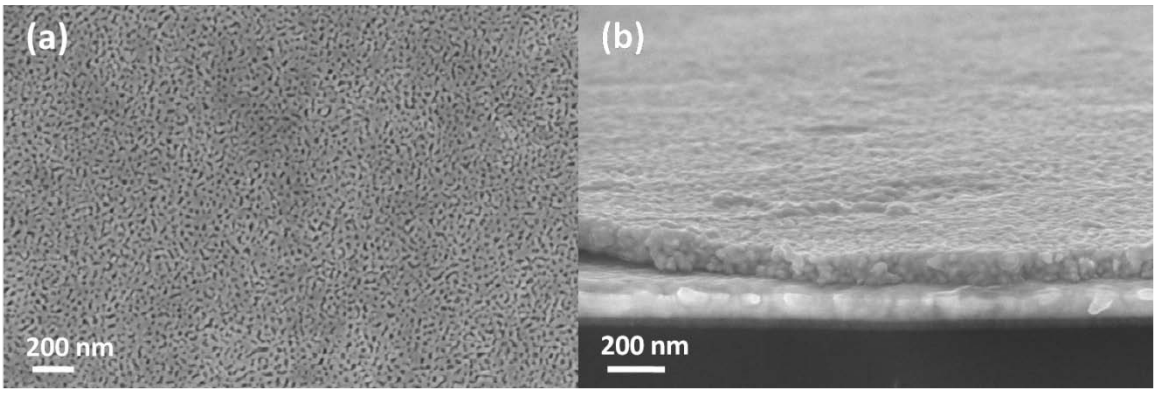

Figure 1-13 Top view (a) and side view (b) SEM images of a typical NPG sample on a gold-coated (100 nm) silicon wafer. The darker regions are void space and the bright regions are the interconnected gold.

NPG films are typically fabricated in a straightforward manner by dealloying silver in nitric acid (HNO_3) from a gold-silver (Au-Ag) alloyed leaf.[70] The Au-Ag alloyed leaf is first transferred from a glass slide to HNO_3, and the ~100 nm thick alloyed leaf is allowed to float on the surface of HNO_3. After 15 min soaking, the silver is completely dissolved and the NPG film is formed. Next, the formed NPG film is transferred from HNO_3 to DI water for rinsing by using a glass slide. Finally, the NPG is transferred from DI water onto an anchoring molecule functionalized hard substrate, such as a 1,6 hexanedithiol functionalized gold substrate or mercaptopropyltrimethoxysilane functionalized glass. Figure 1-14 illustrates the formation of the NPG film.

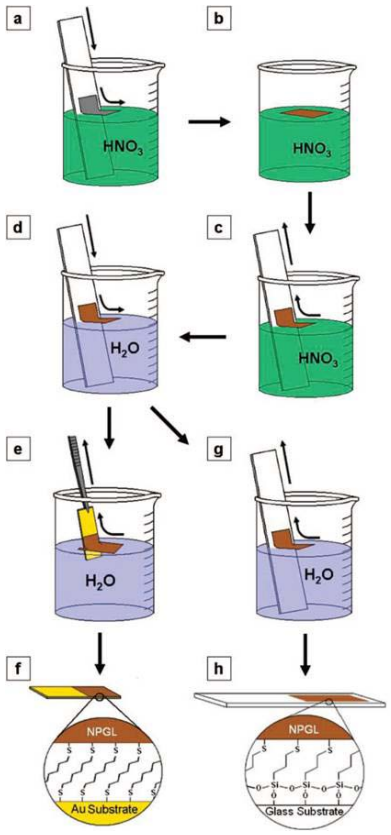

Figure 1-14 Formation of NPG film (a) Au-Ag leaf is transferred to Nitric acid (HNO_3). (b) The leaf is allowed to float on the surface of HNO_3 to resolve silver. (c) After NPG is formed, NPG film is removed from HNO_3. (d) NPG is transferred to DI water for the rinsing. (e) NPG is removed by a 1,6 hexanedithiol functionalized Au substrate. (f) NPG is deposited on Au substrate. (g) NPG is removed by a mercaptopropyltrimethoxysilane functionalized glass substrate. (h) NPG is deposited on glass substrate. (Adapted from Ref. [70])

1.4 Objective and Overview of the dissertation

The objective of this thesis is to combine the advantages of nanoscale porous materials with existing layered optical structures in order to design and fabricate compact, cost-effective, and highly reproducible sensing substrates with significantly improved sensing performance for both molecular quantification and identification.

In CHAPTER 2, a polymer-cladded PSi membrane waveguide biosensor in the Kretschmann configuration is demonstrated that has the potential to outperform traditional SPR sensors while maintaining compatibility for use in commercialized SPR measurement tools. Based on this structure, a

general analytical expression of detection sensitivity for prism-coupled porous waveguide structures is derived, which can be used in the future as a guide to optimize many other similar structures. By properly choosing the design parameters, optimized PSi waveguides show highly improved detection sensitivity in detecting chemical and biological molecules. Furthermore, the optimized infiltration efficiency of molecules with various sizes is also investigated based on the same sensing platform, which proves the filtering effect as well as the existence of an optimized ratio between pore opening and molecule size. In CHAPTER 3, a single-layer PSi interferometer coated with gold nanoparticles (Au NPs) is demonstrated as an effective dual mode sensing platform, which not only supports refractive index based detection to quantify target molecules, but also provides detailed molecular information via SERS. In order to improve the SERS enhancement, a grating coupled PSi waveguide structure coated with Au NPs is demonstrated in CHAPTER 4 with the focus on SERS applications. This waveguide based SERS substrate shows more than 20 times stronger SERS signal than that from the single layer interferometer based SERS substrate. In CHAPTER 5 a uniform, highly sensitive, and easy-to-fabricate NPG based SERS-active substrate is presented that combines the self-organized and highly interacting nanoscale morphology of NPG with the advantages of reproducibly nanopatterned periodic structures. Optimization of the SERS response based on the efficient activation of plasmonic effects is also discussed in this chapter. In CHAPTER 6, further optimizations of grating structures are performed on the NPG based SERS substrate introduced in CHAPTER 5, in order to activate stronger plasmonic effects, and thus the stronger SERS intensity. Final conclusions of the thesis and directions for future research are presented in CHAPTER 7.

CHAPTER 2.

POLYMER-CLADDED POROUS SILICON WAVEGUIDE BIOSENSORS

2.1 Overview

Dielectric and metal-cladded porous dielectric waveguides have recently attracted a great deal of attention for chemical and biological sensing applications. Porous dielectric waveguides provide a larger available surface area for biomolecule capture and an increased mode overlap between the electric field and target biomolecules compared to conventional sensors based on planar substrates, such as silicon-on-insulator waveguides and SPR sensors, which rely on detection using evanescent waves.[42] Gold-cladded porous TiO_2,[55] porous silica,[61] and porous alumina[40]waveguides, and aluminum-cladded porous alumina waveguides[43] in the Kretschmann configuration have been demonstrated for the detection of various small biomolecules and analytes with up to nine times higher sensitivity than bulk waveguide sensors.[61] Polymer-cladded porous silicon waveguides in the Kretschmann configuration were also recently introduced and demonstrated for high sensitivity detection of DNA molecules.[54] While these reports are promising for the emergence of metal and dielectric-cladded porous dielectric waveguides for enhanced small molecule detection, a comprehensive study to determine optimal waveguide parameters for best biosensing performance is needed. In this section, we quantitatively demonstrate, through both theory and experiment, how the choice of porous dielectric waveguide porosity and mode order directly impacts the waveguide sensor performance. The influence of the cladding and waveguide layer thickness are also discussed.

Further improvement in sensor performance can be expected from appropriately tuning the pore size to permit efficient infiltration of target molecules. Here, we also investigate the infiltration efficiencies of variously sized molecules in pores of different sizes in order to achieve an optimal balance

between the detection sensitivity and filtering capabilities of the porous material. We expect that the surface coverage of molecules in porous media will strongly depend on the ratio of the pore size to the molecule size. Beyond sensing applications, understanding the infiltration of target species exposed to porous media is of great importance for a variety of other applications ranging from drug delivery to photovoltaics, fuel cells, and optical interconnects.[60, 75-82]

2.2 High sensitivity porous material based waveguide sensor

2.2.1 Materials and methods

Polymer-cladded porous silicon (PSi) waveguides in Kretschmann configuration are defined as shown in Figure 2-1. Transverse electric (TE) polarized light from a 1550 nm diode laser with the electric field oriented in the *y*-direction is incident on a prism. If the tangential component of the incident wave vector in the prism matches the wave vector of a guided mode in the porous silicon waveguide, then light can evanescently couple through the cladding into the waveguide, and there is a decrease in the measured intensity of reflected light at that resonance angle.

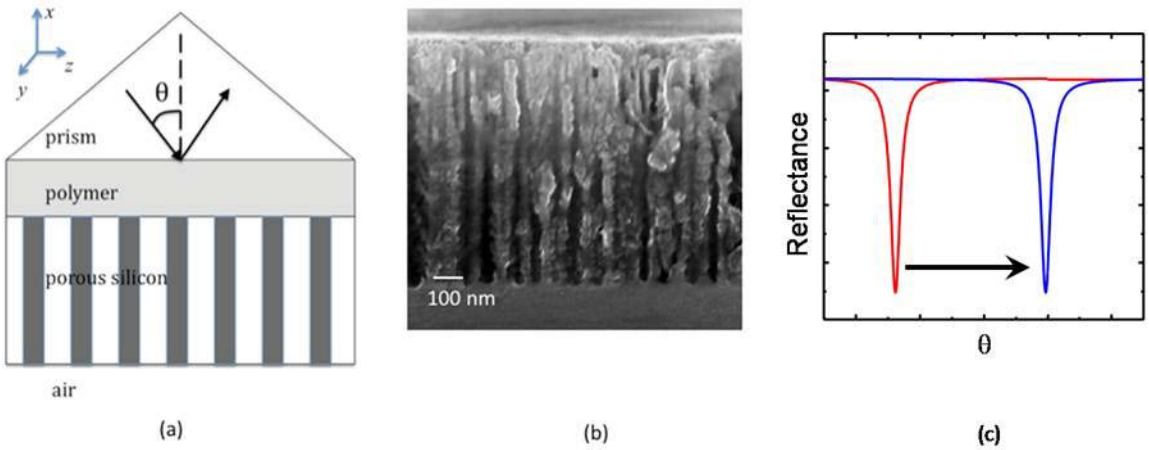

Figure 2-1 (a) Schematic diagram of polymer-cladded PSi membrane waveguide sensor. A prism is used to couple the light into the PSi waveguide layer at particular resonant angles. (b) Cross-sectional SEM of a PSi layer. (c) Schematic illustration of a typical angle-resolved reflectance spectrum before and after molecule attachment. (Adapted from Ref. 4)

In order to determine how the detection sensitivity of polymer-cladded PSi waveguides depends on

the waveguide design parameters, transfer matrix theory[49] in 0 and first order perturbation theory[83, 84] are employed. Here, detection sensitivity is defined as the angular shift of the waveguide resonance divided by the refractive index change of the PSi layer due to attachment of small molecules to the pore walls. Figure 2-1 (c) schematically illustrates a typical angle-resolved reflectance spectrum before and after small molecule attachment in the pores. Molecules infiltrated into the pores induce an overall change in the refractive index of the porous dielectric medium. These dielectric function changes, $\Delta\varepsilon(x)$, also change the effective index of guided modes, N, in the waveguide. According to perturbation theory, the change of the effective index of a guided wave due to small molecule attachment can be calculated by

$$\Delta\left(N^2\right)=\frac{\int_{-\infty}^{\infty}\Delta\varepsilon(x)\left[E(x)\right]^2 dx}{\int_{-\infty}^{\infty}\left[E(x)\right]^2 dx} \tag{2. 1}$$

for TE waves.[83, 84] Note that this theory does not apply to the infiltration of liquids that fill the entire volume of the porous waveguide. The electric field in each layer of the waveguide structure is found based on transfer matrix theory,[49] and the thickness of the cladding layer is optimized to yield deep and narrow waveguide resonances based on the pole expansion method described in Refs.[42, 85]. With $\Delta\varepsilon(x) = 2n\Delta n$, $\Delta(N^2) = 2N\Delta N$, and $N=n_p\sin\theta$, we present an analytical expression of the sensitivity of the waveguide for TE modes

$$sensitivity=\frac{d\theta}{dn}=\frac{d\theta}{dN}\cdot\frac{dN}{dn}=\frac{\int_{PSi}\left[E(x)\right]^2 dx}{\int_{-\infty}^{\infty}\left[E(x)\right]^2 dx}\cdot\frac{n_{PSi}}{N}\cdot\frac{1}{n_p\cos\theta}, \tag{2. 2}$$

where n_p and n_{PSi} are the refractive index of the prism and PSi, respectively, and θ is the resonant angle in the prism. The first term on the right hand side of Eq. (2.2) is the power confinement factor, which is defined as the ratio of the power confined in the PSi layer to the total power distributed throughout the entire multilayer waveguide structure. The sensitivity is directly proportional to the power confinement factor and the incident angle in the prism.

2.2.2 PSi waveguide fabrication

PSi membranes with different porosities and pore sizes were fabricated by electrochemical etching of n-type (0.01Ω·cm) silicon wafers in a 5.5% HF electrolyte (25 mL 50% aqueous HF + 200 mL deionized water). By applying different current densities and etching times during the etching process, PSi layers with distinct porosity and thickness can be fabricated.[65] Current densities from 15 to 30 mA/cm^2 were applied for corresponding etching times of 78 to 72 seconds in order to achieve PSi membranes with approximately the same thickness of 1.55 μm (± 50 nm) and porosities between 37% and 58%. The detailed etching conditions (current density and etching time) and the resulting porosities and pore sizes are given in Table 2-1.We note that the porosities were determined directly from the refractive indices of the PSi membranes using Maxwell-Garnett effective medium theory.[86, 87] The refractive indices of the PSi membranes were determined through experiments, as explained in detail in section 2.2.4. The corresponding pore openings ranged from approximately 40 nm to 80 nm. Each PSi membrane was removed from the silicon substrate by applying a series of high current pulses (160mA/cm^2 for 4 s with 50% duty cycle). The PSi membranes were oxidized at 500˚C for 5 minutes in an Omegalux LMF-3550 oven, after insertion at 300˚C, in order to lower the waveguide loss[41] and to prepare the surface for subsequent small molecule attachment.

Current density (mA/cm^2)	Etching time (s) for thickness of 1.55 μm (± 50 nm)	Porosity	Average pore diameter (nm)
15	78	37%	40
20	75	48.5%	50
25	78	55%	60
30	72	58%	80

Table 2-1 PSi etching conditions (current density and etching time) and the resulting porosities and pore diameters

The polymer cladding layer was fabricated by dropping 0.15% formvar polymer in ethylene

dichloride (Ernest F. Fullam, Inc.) onto a cubic zirconium prism (Metricon, n=2.1252). The PSi membrane was placed on top of the polymer cladding before complete evaporation of the solvent to ensure robust adhesion. For all waveguide samples, an approximately 500 nm thick formvar polymer layer (n~1.49 measured by ellipsometry near 1550 nm) formed after solvent evaporation. Note that the thickness of the polymer layer can be controlled by adjusting the concentration of the formvar polymer solution. Other lower refractive index polymers such as fluorocarbon polymer (FCP) can also be utilized as the cladding materials for fabricating waveguides due to its low loss and high stability in a strong acid or alkali environment. With relatively low refractive index, better field confinement can be achieved due to the higher refractive index contrast between porous waveguide and cladding layer.

2.2.3 PSi waveguide surface functionalization

In order to confirm the predicted performance of the polymer-cladded PSi waveguide sensor, 4% 3-aminopropyltriethoxysilane (3-APTES) [3-APTES (99%, Aldrich): methanol: deionized water (DI water) = 4:46:50] was dropped onto the PSi surface and the sample was incubated in a humid environment for 20 minutes. The humid environment was created by placing Kimwipes soaked in DI water around the sample inside a sealed plastic container (e.g., large Petri dish). After incubation, the sample was rinsed with DI water, dried with nitrogen gas, and baked at 100°C for 10 minutes. The small molecule 3-APTES with a refractive index of 1.46 has been previously shown to form a uniform monolayer of thickness 0.8 nm on PSi walls.[88] We note that the choice of 3-APTES was motivated by the desire to select a well-characterized molecule for comparison to our theoretical calculations. Prior work has demonstrated selective detection of DNA, proteins, and other small molecules in PSi.[54, 56]

2.2.4 Results and discussion

2.2.4.1 Theoretical sensitivity calculation

Based on the mathematical methods described in section 2.2.1, we plot the theoretically calculated sensitivity as a function of the porosity for a 1.55 μm thick polymer-cladded PSi waveguide layer in

Figure 2-2 (a). The corresponding resonance angles are shown in Figure 2-2 (b). Each curve corresponds to one guided mode. Higher order modes can be supported at lower porosities. For each mode, the sensitivity decreases with increasing porosity of the PSi layer until the mode cutoff condition at the critical angle is satisfied. As the incident angle approaches 90°, the sensitivity theoretically goes to infinity. At very large incident angles, the $1/\cos\theta$ term dominates the power confinement factor in the sensitivity calculation, while the opposite is true at smaller incident angles. Note that if the thickness of the PSi waveguide layer is increased, the curves will be shifted upward and the number of modes supported by the waveguide might also be increased.

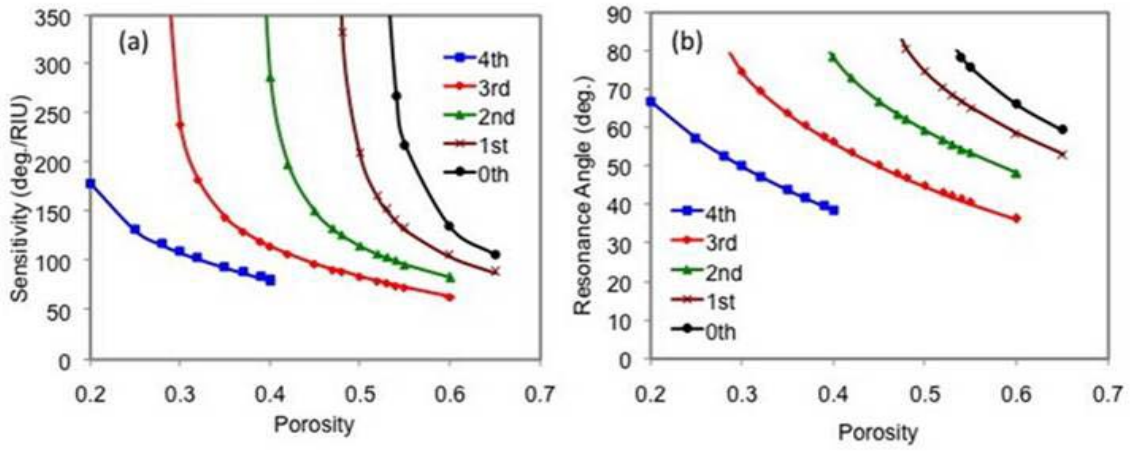

Figure 2-2 (a) Calculated detection sensitivity and (b) corresponding resonant coupling angle of polymer-cladded PSi waveguides as a function of the porosity of a 1.55 μm thick PSi membrane waveguide. Multiple orders of modes can be supported at a given porosity. (Adapted from Ref. 4)

2.2.4.2 Gold-cladded PSi waveguide

As a comparison, the detection sensitivity of a gold-cladded PSi waveguide was also theoretically investigated, since such a metal-cladded porous waveguide structure can be fabricated based on a conventional SPR sensor structure via straightforward addition of a porous layer on top of the metal film.

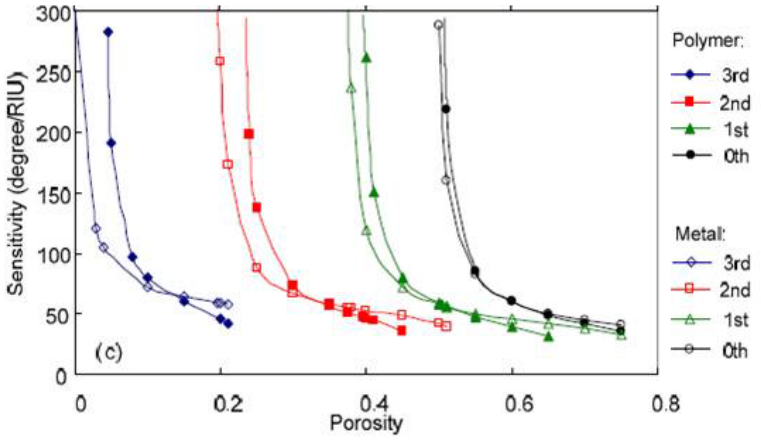

Figure 2-3 Calculated detection sensitivity of polymer-cladded PSi (solid symbols) waveguides and gold-cladded PSi waveguides as a function of the porosity of a 1 μm thick PSi membrane waveguide. The sensitivities of both cases are comparable. (Adapted from Ref. [89])

Figure 2-3 shows the sensitivity comparison between polymer-cladded PSi waveguides (solid symbols) and gold-cladded PSi waveguides as a function of the porosity of a 1 μm thick PSi membrane waveguide. Note that, compared to the 1.5 μm thick PSi membrane waveguide, the number of modes supported within the same PSi porosity range is decreased due to the reduced thickness of PSi waveguide layer. Based on Figure 2-3, we found that both cladding materials can provide ultra high detection sensitivity when the cut-off porosity for each mode can be approached. Therefore, there is no obvious advantage of using gold or polymer as the cladding material when considering the sensitivity of the waveguide sensor.

However, evaluation of the overall sensor performance is not limited to sensitivity. The accuracy of detecting resonance shifts due to molecular binding must also be considered. It is more challenging to accurately quantify small angular deviations of broad resonance dips compared to narrow resonances with steep slopes. Furthermore, the sensor response time should be considered as it is preferable to detect binding events as rapidly as possible. Therefore, we introduce a quality factor in Eq. (2.3) to compare the overall performance of optical biosensors.

$$Quality\ \ factor = \frac{sensitivity}{FWHM \cdot thickness} \tag{2. 3}$$

The quality factor takes into account the sensitivity of the sensor, full-width-at-half-maximum (FWHM) of the resonance, and thickness of the active sensor region where molecules interact with the electric field. We note that the units of quality factor are given as $(\text{RIU}\cdot\mu\text{m})^{-1}$. From Eq. (2.3), it is evident that a smaller FWHM and larger detection sensitivity are desired because a narrower resonance feature allows more efficient detection of the resonance shift and precise analysis of the sensitivity. In addition, thinner active sensor regions promote faster sensor response.

The FWHM of polymer and gold-cladded PSi waveguides is determined based on the resonance angle and total loss of the entire structure.[85] With an optimized cladding layer thickness, the FWHM of the resonance dip can be expressed by

$$FWHM = \frac{4\gamma}{(2\pi/\lambda)n_p \cos\theta}, \tag{2. 4}$$

where γ is the imaginary part of the wave vector, which describes the total loss of the entire structure and n_p is the refractive index of the prism. While it is clear from Eq. (2. 2) that sensitivity is independent of the loss of the multilayer waveguide structure, the FWHM of the resonance dip is highly dependent on losses. If the total losses go to zero, the FWHM of the resonance dip also goes to zero, and no resonance feature is observed in the attenuated total reflectance (ATR) spectrum. For polymer-cladded PSi waveguides, the only source of total loss is from absorption and scattering losses in the PSi layer because the polymer layer is assumed to be lossless (< 0.5 dB/cm). For gold-cladded waveguides, an additional loss mechanism introduced by the gold layer contributes to the total loss of the multilayer waveguide due to the large absorption loss of gold. In many cases, the gold absorption loss is the dominant loss of the entire structure.

In our evaluation of the quality factor, we include different effective PSi absorption losses, which take into account both material absorption and scattering losses, by directly adding different imaginary contributions to the complex refractive index of silicon $n\text{-}j\kappa$. The absorption loss coefficient α' (dB/cm) can be described by

$$\alpha' = \frac{10\gamma}{\ln(10)}, \tag{2. 5}$$

with $\gamma=(4\pi/\lambda)\kappa$. The FWHM, and therefore quality factor, change in accordance to the magnitude of different loss contributions. Figure 2-4 shows the quality factors of polymer and gold-cladded PSi waveguides as a function of the imaginary part of the silicon index. As expected, the quality factor decreases as the loss contribution increases. Although a particular order of guided mode is supported over a range of PSi waveguide porosities, in Figure 2-4, we choose one representative porosity for each mode (i.e., we choose porosities of 10%, 40%, 60% and 70% for 3rd, 2nd, 1st, and 0th order modes, respectively) at which the modes have approximately the same sensitivity. For a given PSi loss value, gold-cladded PSi waveguides have significantly lower quality factors compared to those of polymer-cladded PSi waveguides due to the large absorption loss from the gold film. For low-loss PSi waveguides approaching 1 dB/cm, the quality factor exceeds 10,000. The scaling of quality factor with effective PSi absorption losses is slightly different for the polymer and gold-cladded PSi waveguides because the gold-cladded PSi waveguides have an additional gold cladding thickness dependent absorption loss that contributes to quality factor calculation. The optimized gold cladding thickness changes with the optical thickness of the PSi layer and mode order supported by the PSi waveguide.

For comparison of the performance of polymer- and gold-cladded PSi waveguide sensors to traditional SPR sensors for small molecule detection, we additionally calculate the quality factor of SPR sensors based on first order perturbation theory.[83,84] In Figure 2-4 (b), the dashed line (quality factor ~ 100) and the dotted line (quality factor ~ 50) indicate the approximate quality factors of SPR sensors used to detect the attachment of thin molecular layers (<1-10nm) at wavelengths of 1550nm and 633nm, respectively. It is clear from comparing Figure 2-4 (a) and (b) that for effective PSi absorption losses below 1000 dB/cm, both gold- and polymer-cladded PSi waveguides have superior performance for small molecule detection compared to SPR sensors. Furthermore, we find that polymer-cladded PSi waveguides show the best performance for all conditions considered in this theoretical analysis.

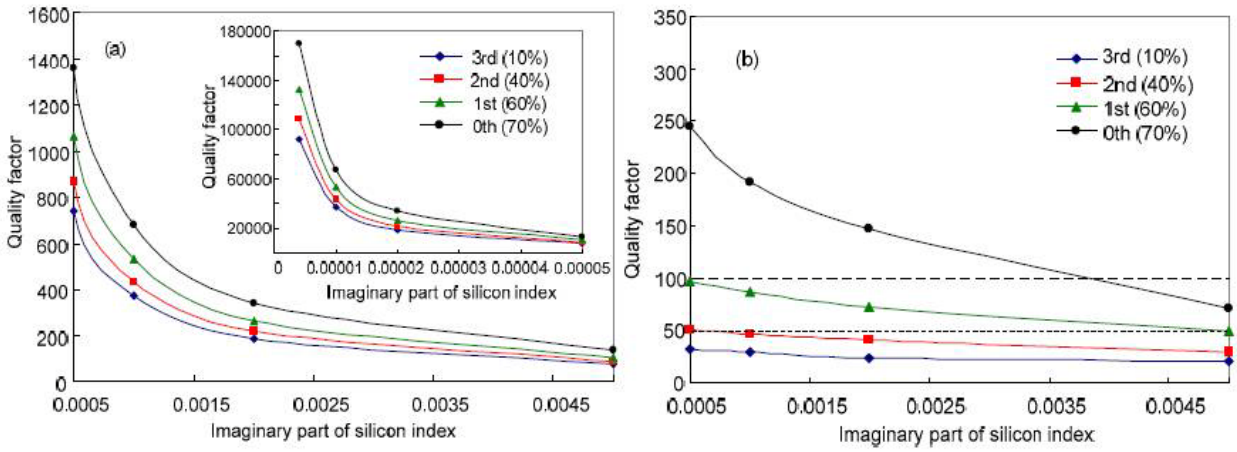

Figure 2-4 Quality factors of polymer-cladded waveguides (a) and gold-cladded waveguides (b) as a function of the imaginary part of the silicon index. The quality factor of SPR sensors at 1550 nm (dashed line) and 633 nm (dotted line) is shown in (b). Polymer-cladded PSi waveguides exhibit significantly higher quality factors than gold-cladded waveguides and conventional SPR sensors. The inset of (a) shows that very large quality factors can be achieved for low-loss PSi waveguides. (Adapted from Ref. [89])

2.2.4.3 Experimental sensitivity analysis of 3-APTES detection

Experimental verification of the predicted relationship between PSi waveguide porosity and small molecule detection sensitivity was performed by measuring the resonance angle of polymer-cladded PSi waveguides using a Metricon 2010 prism coupler before and after infiltration of 3-APTES. Since a different refractive index change results from monolayer 3-APTES coverage in PSi waveguides with different porosity and pore diameters, the PSi refractive index change due to monolayer 3-APTES coverage was determined separately for each sample. First, the PSi refractive index for each sample before 3-APTES addition was uniquely determined by fitting the experimentally measured guided and leaky mode angles to theoretical calculations using the experimentally measured refractive index of the polymer cladding from ellipsometry and the experimentally measured thickness of the PSi waveguide layer from SEM.[54] The corresponding porosity for each PSi sample was determined through 2D Maxwell-Garnett theory by modeling the pores as cylinders and assuming that there is a 1.6 nm thick silicon dioxide layer formed on the PSi pore walls after oxidization.[86, 87] The PSi refractive index for each sample after 3-APTES addition was determined by decreasing the pore radius by 0.8 nm; here we approximate the refractive index of 3-APTES to be the same as that of silicon dioxide and effectively increase the

thickness of the oxide layer on the modeled cylindrical pore walls.[90]

Typical ATR measurements of a 58% PSi waveguide before and after 3-APTES attachment are shown in Figure 2-5 (a). The PSi waveguide supports 3rd, 2nd, and 1st order modes in the limited angular range of the Metricon prism coupler (32° - 68°). After 3-APTES attachment, we observe 0.53°, 0.83° and 0.93° shifts for 3rd, 2nd, and 1st order modes, respectively. With a refractive index change of ~0.0125 induced by the monolayer of 3-APTES, the sensitivities are found to be 42.4, 66.4 and 74.4 deg./RIU for 3rd, 2nd, and 1st order modes, respectively. Hence, we can conclude that highest sensitivity small molecule detection occurs for lower order modes supported at larger resonance angles, which is in agreement with the theoretical results shown in Figure 2-2. We note that the slight difference in resonance width for each mode is likely due to the polymer cladding thickness. Since the data in Figure 2-5 (a) was taken from a single sample, the cladding thickness could not be optimum for all modes.[42, 85] Figure 2-5 (b) shows a summary of the experimentally determined sensitivities of the polymer-cladded PSi waveguides as a function of PSi porosity within the achievable angular measurement range of the Metricon prism coupler. There is a clear trend of increasing detection sensitivity with decreasing porosity for the 2nd and 3rd order modes, in good agreement with the predicted trends shown in Figure 2-2 (a). A closer comparison of the experimentally measured sensitivity curve shown in Figure 2-5 (b) with the theoretically calculated sensitivity curve in Figure 2-2 (a) reveals that the sensitivities based on the experimental measurements were higher than the sensitivities predicted by theoretical calculation. We attribute the increased sensitivity to the branches on the sidewalls of the pores, as shown in Figure 2-1 (b), that lead to a much larger available surface area for 3-APTES attachment than expected based on the perfect cylindrical pore model. Lower porosity samples have smaller pore openings and more branchy sidewalls,[66] which explains why there is a larger sensitivity discrepancy between experiment and theory at lower PSi porosities.

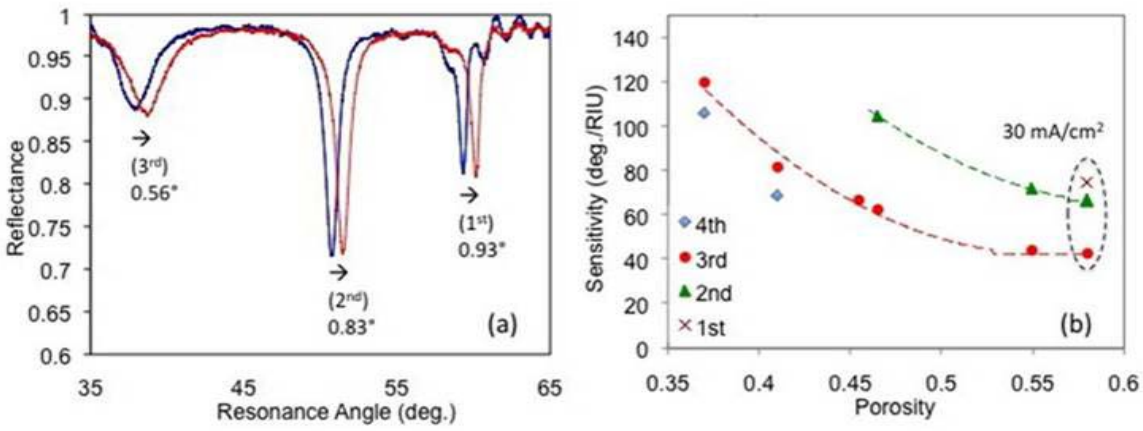

Figure 2-5 (a) Experimentally measured resonances of a 58% porosity, 1.55 μm thick PSi waveguide with polymer cladding before and after attachment of 3-APTES molecules. (b) Experimentally measured sensitivities of polymer-cladded PSi waveguides (solid symbols) as a function of the porosity of a 1.55 μm thick PSi waveguide layer at wavelength of 1550 nm. Curve fitting of the data points for 2nd and 3rd order modes clearly demonstrates the trend of increasing sensitivity with decreasing porosity. (Adapted from Ref. 4)

2.2.4.4 Experimental sensitivity analysis of 16mer PNA detection

The importance of waveguide design for achieving high detection sensitivity for small molecules was experimentally demonstrated via the non-specific attachment of 3-APTES in PSi waveguides. In this section, the specific detection of peptide nucleic acid (PNA) molecules is demonstrated based on the same ~58% porosity PSi waveguide shown in Figure 2-5 (a).

In order to detect a particular target biomolecule, special functionalization steps need to be carried out to link organic molecules to the inorganic silicon pore walls. Selective detection of a particular target biomolecule is achieved by proper choice of a complimentary probe molecule that is first immobilized in the pores. To enable the PNA detection after 3-APTES silane functionalization, the cross-linker sulfosuccinimidyl-4-N-maleimidomethyl)cyclohexane-1-carboxylate (sulfo-SMCC) in 50% water and 50% ethanol was attached to the silane monolayer to provide the necessary surface chemistry for probe DNA attachment (2 hour soaking in sulfo-SMCC followed by 1 hour soaking in HEPES buffer and a thorough rinsing by using DI water). Next, 200 μM of 16mer probe DNA with sequence of 5'-GGGG GGGG GGGG GGGG[ThiSS-Q]-3'(Eurofins MWG Operon) in HEPES buffer was mixed 1:1 by volume with tris(2-carboxyethyl)phosphine (TCEP) in water and ethanol[39] to obtain 100 μM probe

DNA solution, and this 100 μM 16mer probe DNA solution was infiltrated into the PSi sample via a 1 hour soaking followed by a thorough rinsing using HEPES buffer solution. For the sensing experiments, complimentary, uncharged 16mer PNA molecules with sequence of 5'-CCCC CCCC CCCC CCCC-3' (Biosynthesis, Inc.) were exposed and hybridized to the negatively charged probe DNA molecules in a humid environment for one hour. Here we used the PNA molecules to avoid the possible corrosion of the PSi pore walls caused by hybridizing negatively charged DNA molecules.[91] Figure 2-6 shows the experimentally measured changes of resonance angles of the polymer-cladded PSi waveguide due to the pore surface functionalization, including the infiltration of 3-APTES, sulfo-SMCC, and 100 μM probe DNA, and the specific attachment of 10 μM complimentary PNA. By matching the experimentally measured resonances with simulation results, the refractive index of the PSi film is calculated to be ~2.05, which corresponds to the porosity of ~57% based on the Maxwell-Garnett effective medium theory.[87] From Figure 2-6, it is clear that in the limited Metricon prism coupler measurement range (32°-68°) this PSi waveguide supports 3rd, 2nd, and 1st order modes, which are initially located at ~38°, ~51°, and ~62°, respectively, as shown by the black solid line in this figure. Each functionalization step was confirmed as the resonance angle shifts to the higher values. The magnitude of the resonance shift directly correlates to the size and number of molecules attached.

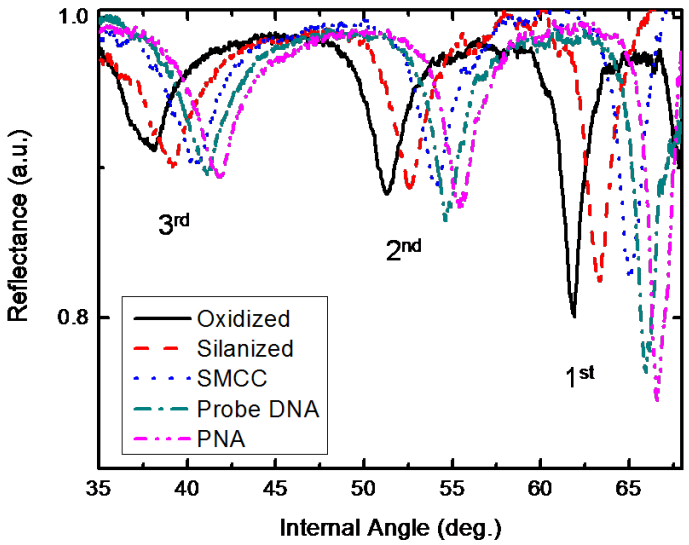

Figure 2-6 Attenuated total reflectance (ATR) spectra of a 1.55 μm thick, 57% porosity PSi waveguide after (from left to right) oxidation and infiltration of 3-APTES, sulfo-SMCC, 100 μM probe DNA and 10 μM target PNA. The resonances on the left, middle and right part of this figure are 3rd, 2nd and 1st order modes, respectively. The resonance dips at higher angle (lower order mode) show larger shifts for all infiltrated molecules. (Adapted from Ref. [92])

The resonance angle shifts from 16mer probe DNA to 16mer complimentary PNA for 3rd, 2nd, and 1st order modes are 0.46°, 0.67°, and 0.72° respectively, which shows the expected trend of increased sensitivity for higher angle resonances, as predicted by our perturbation theory calculations and the experimental results for the small 3-APTES molecule. We note that the 16mer complimentary PNA shows a smaller resonance shift compared to the resonance shift from oxidization to silanization although the length of PNA molecules is much larger than the size of 3-APTES molecules. This smaller magnitude resonance shift can be attributed to the much lower surface coverage of the larger 16mer probe PNA (~15%) compared to 3-APTES (~90%).[93]

2.3 Size-dependent infiltration in nanoscale pores

2.3.1 Materials and methods

Prism coupled polymer-cladded single layer PSi waveguide structures, as described in section CHAPTER

2, were utilized as the sensing substrate for the size dependent infiltration experiments. Similarly, single layer PSi samples with pore diameters of approximately 15, 30, or 60 nm, porosities of 30%, 35%, and 57%, respectively, and thicknesses of ~1.55 μm were formed on highly doped n-type (0.01 Ω·cm) silicon wafers using an electrolyte containing 5.5% HF in DI water and applied current densities of 8 mA/cm^2 (180 s), 10mA/cm^2 (82 s), and 30 mA/cm^2 (72 s), respectively. Figure 2-7 shows the side view SEM images revealing morphology of n-type PSi with various pore sizes. Following PSi formation, these PSi layers were removed from the silicon substrate by applying a series of high current pulses and attached to a prism using a low index polymer cladding layer, the same process as described in section 2.2.[4]

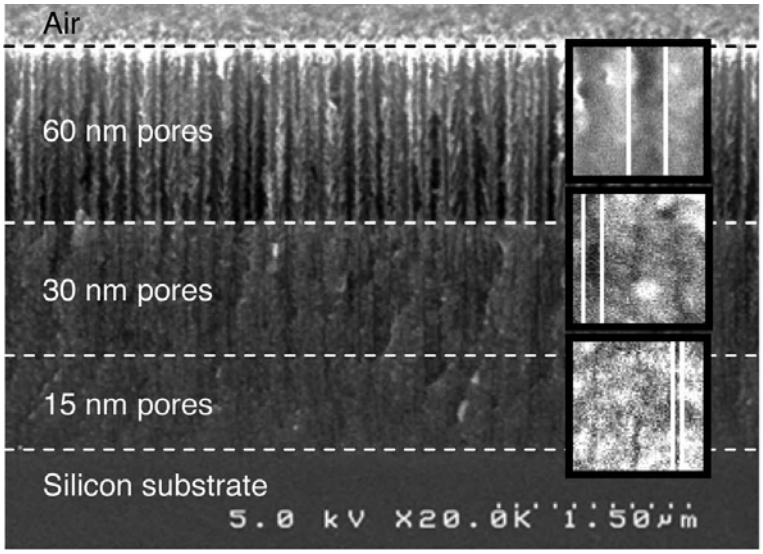

Figure 2-7 Side view SEM image showing the morphology of n-type PSi layers with various pore sizes (from top to bottom: 60, 30, 15 nm). This image was generated to provide ease of comparison for the three different pore sizes. Samples prepared for the study were formed by etching a single layer of porous silicon (uniform porosity) and lifting it off from the substrate. (Adapted from Ref. [93])

2.3.2 Results and discussion: Trends of size-dependent infiltration

Molecular infiltration efficiency was investigated via the shift of resonance position. Figure 2-8 illustrates the trend of molecular size-dependent infiltration in the porous silicon single layer waveguides for different pore diameters. The largest magnitude resonance shift for each pore size occurs for a different size molecule, with larger molecules more efficiently infiltrated in the larger pores. The molecule utilized in these experiments is DNA; the molecule size is easily adjusted based on the sequence length, given that

the length of single strand DNA is 2.2 Å/base. Figure 2-8 provides a convenient guide to determining an appropriate pore size for the detection of a particular sized molecule. Note that for the various pore sizes presented in Figure 2-8, we can compare the magnitude of the resonance shifts since all single layer waveguides were designed with similar initial resonance angle, following the results of the sensitivity analysis described in section 2.2. For example, the resonance shift upon infiltration of 100 μM 8mer DNA (~1.76 nm) is largest for the 15 nm pores, suggesting that the smallest pores offer the highest sensitivity detection for the smallest molecules considered in this study. We conclude that the 8 mer molecules are small enough that their infiltration is not significantly hindered by even the smallest pore opening studied in this work, and the additional surface area provided by the smaller, branchy pores allows for more DNA to be captured. For the larger DNA molecules investigated, the smallest pores are no longer suitable for high efficiency infiltration and a larger pore size should be utilized. The 60 nm diameter pores show the largest response upon infiltration of 100 μM 24mer DNA (~5.28 nm), indicating larger pore sizes are required for the detection of longer targets. For infiltration of 16 mer DNA, both the 30 nm and 60 nm pores give a large response; however, the 30 nm pore provides enhanced filtering capabilities to prevent larger contaminant particles from entering the pores. By balancing ease of molecular infiltration with pore volume fraction change upon immobilization of molecules, porous media can be optimally tuned for best sensing performance.

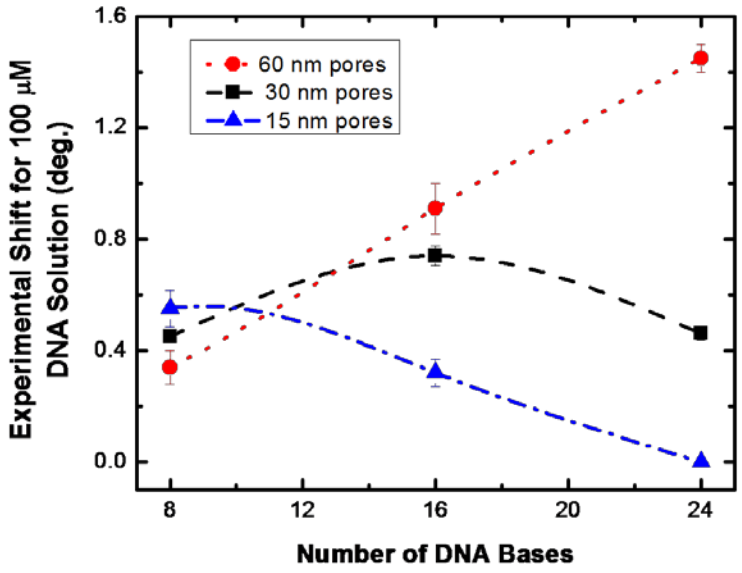

Figure 2-8 Resonance angle shifts for single-layer porous silicon waveguides with different average pore sizes for detection of 100 µM DNA molecules of different lengths (~2.2Å/base). For optimal performance as a sensor, the pore size must be appropriately tuned based on the size of the molecule of interest. (Adapted from Ref. [93])

2.4 Conclusions

We used a polymer-cladded PSi membrane waveguide biosensor to quantitatively demonstrate through both theory and experiment how the choice of porous dielectric waveguide porosity and mode order directly impact waveguide biosensor performance. The increased surface area available for molecular attachment and increased mode overlap between the electric field and biomolecules enable polymer-cladded PSi waveguides to perform high sensitivity small molecule detection. Perturbation theory calculations suggest that the sensitivity asymptotically approaches infinity as the porosity of the waveguide approaches a critical porosity for a given mode and the resonant coupling angle of light into the waveguide approaches 90°. For a given mode, decreasing the porosity of the PSi waveguide layer increases the small molecule detection sensitivity. Experimental measurements in which 3-APTES molecules are attached inside PSi waveguides of different porosities verify the porosity and mode order-dependent sensitivity trends predicted by perturbation theory. Furthermore, it was demonstrated that lower order waveguide modes, corresponding to higher resonance angles, provide higher sensitivity

detection of PNA molecules that are hybridized to a functionalized PSi waveguide. With the available measurement apparatus, which restricts the maximum coupling angle to 68°, small molecule detection sensitivity greater than 120 degrees/RIU was demonstrated; much higher sensitivities are predicted and should be achievable if the angular measurement range of the prism coupler is extended.

We also reported a clear size-dependent infiltration and surface coverage of molecules in porous silicon waveguides. Incremental increases in pore diameter allow for selectivity toward target molecules of a particular length (or size), as demonstrated in porous silicon waveguides with controllable pore diameters between 15 and 60 nm that are exposed to nucleic acids of length between approximately 1.76 and 5.28 nm. Appropriate choice of pore size will allow the infiltration of a molecule of interest while excluding larger contaminating molecules.

CHAPTER 3.

DUAL-MODE SENSING PLATFORM BASED ON GOLD NANOPATICLE COATED PSI SUBSTRATE

3.1 Overview

Typical sensors only operate in a single mode. For example, molecular binding events can be detected by monitoring thin film interference patterns using spectral reflectance,[34, 56] waveguide resonances using angle-resolved reflectance,[53, 54, 90] or microcavity emission peaks using photoluminescence measurements.[18, 57] In CHAPTER 2, we utilized a polymer-cladded PSi waveguide structure as an effective template to demonstrate that porous materials are promising candidates for label-free refractive index based sensing due to the large available surface area for molecular binding and their capability of size-selective molecule filtering. This refractive index based sensing method requires immobilization of a specific functional surface probe molecule for the target molecule. Raman scattering on the other hand is based on an inelastic scattering process, where a small fraction of incident photons experience scattering processes with energy shifts after interacting with molecular species. The energy differences between the incident and scattered photons are determined by the vibrational states of molecular species and therefore can be directly utilized to identify specific molecules.[5] Surface enhanced Raman scattering (SERS) provides a drastic enhancement in scattering efficiency over traditional Raman scattering primarily due to the presence of intense electromagnetic fields localized at the metal surface where molecules are adsorbed.[5, 94] Numerous SERS substrates have been demonstrated for highly sensitive detection, even down to single molecule detection.[10] In recent year, porous materials that incorporate metallic nanoparticles and porous metals have also been reported as promising SERS-active templates due to their unique nanoscale surface morphologies and the resulting strong localized surface plasmon (LSP) effect.[13,

[58, 95] Most of these porous material based SERS substrates do not require complex fabrication process, and the porous materials act as templates for the metal deposition to form the metallic rough surface.

In this work, we demonstrate a dual-mode sensing platform based on a single layer PSi film decorated with colloidal gold nanoparticles (Au NPs) to realize both molecular quantification and identification. Colloidal Au NPs are a convenient SERS platform due to their strong localized field confinement, controllable size, and chemical stability.[18] Numerous colloidal Au NPs based templates including Au NPs suspended in solution and nanostructures decorated with colloidal Au NPs have been reported as effective and controllable SERS substrates.[18, 96, 97] Our hybrid Au-PSi structure combines the advantages of molecular quantification via refractive index sensing in reflectance mode and molecular identification via SERS spectral analysis on a single substrate. Figure 3-1 shows the schematic of the Au NPs decorated single layer PSi, where small Au NPs are deposited on both the top surface and pore walls of PSi. In order to demonstrate the dual mode concept, the most straightforward single-layer PSi interferometer structure discussed in section 1.2.1 was firstly utilized.

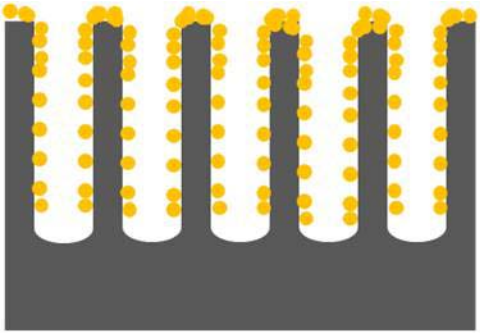

Figure 3-1 Schematic configuration of Au NPs coated single layer PSi

3.2 Materials and methods

3.2.1 PSi substrate fabrication

Single layer PSi films were fabricated by electrochemical etching of an n-type silicon wafer (<100>, 0.01 Ω·cm) in 5.5% aqueous hydrofluoric acid (HF).[54] A sacrificial layer was first etched with a current

density of 40 mA/cm^2 for 30 s, and removed from the silicon substrate by applying a high current density pulse (250 mA/cm^2 for 3 s) in a manner similar to what has been reported previously.[54] This electropolishing procedure not only led to wider pore openings (~80 nm) at the top of the PSi layer to facilitate infiltration of Au NPs and target molecules, but it also created a rough surface with approximately 40 nm deep silicon corrugations as shown in the atomic force microscopy (AFM) image in Figure 3-2 (a), which is beneficial for SERS measurements. A 2.3 μm (± 20 nm) thick PSi layer with 60 nm (±10 nm) pore openings was subsequently formed on the roughened silicon wafer by applying a current density of 35 mA/cm^2 for 150 s. The PSi dimensions were estimated based on cross-sectional SEM imaging. The PSi sample was then oxidized at 500°C in air ambient for 5 min (Omegalux LMF-3550 oven).

3.2.2 Colloidal gold nanoparticles (Au NPs)

Two different sizes of Au NPs were prepared by Dr. Dmitry Koktysh using synthetic procedures analogous to those reported elsewhere.[98, 99] Briefly, for synthesis of Au NPs with approximately 4.5 nm size, 1 mL of freshly prepared ice-cold solution of 0.3 M $NaBH_4$ was added to an aqueous solution (100 mL) of $HAuCl_4$ (0.25 mM) and trisodium citrate (0.25 mM) under vigorous stirring. The solution with formed Au NPs was stirred for 10 min. For synthesis of Au NPs with approximately 14.8 nm size, 1 mL of trisodium citrate (1.2 mM) was injected into 100 mL of boiling aqueous solution of $HAuCl_4$ (0.3 mM).[98, 99] After 10 min of vigorous boiling, the solution containing Au NPs was removed from the oil bath and left undisturbed for 1 hour. Transmission electron microscopy (TEM) imaging was performed to confirm the size of the NPs, as shown in the insets of Figure 3-2 (b) and (c). The Au NPs will be denoted further as small (4.5 nm) and large (14.8 nm) Au NPs, respectively.

3.2.3 Fabrication of Au NPs coated PSi substrate

In order to attach the colloidal Au NPs on the pore walls and top surface of the PSi sample, 4% 3-APTES solution in water and methanol was used as a linker molecule.[100] The silanized PSi samples were

immersed in solutions containing either the small (~4.5 nm) or large (~14.8 nm) colloidal Au NPs for 24 hours. After the infiltration, the PSi samples were rinsed with DI water and dried with compressed air. Figure 3-2 (b) and (c) show plan-view SEM images of PSi substrates coated with small and large Au NPs, respectively. The SEM images reveal that the Au NPs are attached to the silicon matrix and the pores remain sufficiently open to enable subsequent infiltration of target molecules.

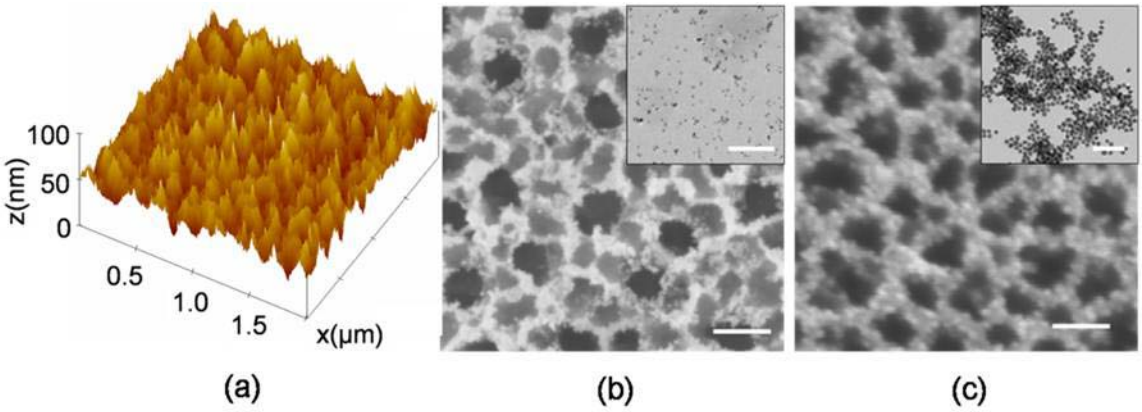

Figure 3-2(a) AFM image of roughened PSi surface after electropolishing. (b) Plan-view SEM image showing a PSi film coated with small (~4.5 nm) Au NPs. A TEM image of the small Au NPs is shown in the inset. (c) Plan-view SEM image of PSi coated with large (~14.8 nm) Au NPs. The inset shows a TEM image of the large Au NPs. All the scale bars indicate 100 nm. (Adapted from Ref. [101])

3.3 Results and discussions

The dual-mode sensing operation of the Au coated PSi substrate was demonstrated by detection of benzenethiol, a commonly used Raman-active molecule. Au-PSi samples were immersed in 0.2 mM benzenethiol in ethanol for 1 hour, and the samples were subsequently rinsed with ethanol and dried with nitrogen.

Reflectance spectra of PSi structures in this work were measured by a Cary 5000 spectrophotometer (Varian) at near normal incidence. SERS spectra were measured at normal incidence with an XploRA 730 Raman microscope (Horiba Jobin Yvon) utilizing a 780 nm diode laser (9 mW) and

100× magnification (NA = 0.9). Data was collected with an integration time of 20 s and averaging of 5 scans.

3.3.1 First sensing operation: reflectance measurements

The first sensing operation was probed by reflectance measurements. Thin film interference fringes undergo a spectral shift based on the Au NPs and benzenethiol molecule induced overall refractive index change of the PSi film. Figure 3-3 shows the reflectance spectra after each process step: after silanization, after attachment of Au NPs, and after adsorption of benzenethiol on the Au NPs. Figure 3-3 (a) shows an approximately 85 nm blue shift of the spectrum upon the infiltration of small Au NPs. The blue shift occurs since the refractive index of Au is smaller than air. A smaller blue shift of approximately 60 nm was observed after exposure of the PSi film to large Au NPs, as shown in Figure 3-3 (b), suggesting that fewer of the large particles infiltrate deep into the PSi film. This phenomenon can be explained as the size-dependent infiltration effect that we learned in section 2.3. We note that the reflectance intensity in both cases is low due to scattering from the rough PSi surface. An approximately 8 nm red shift was observed after benzenethiol adsorption on the small Au NPs while a negligible reflectance shift was observed for the PSi sample with large Au NPs. Benzenethiol naturally forms a monolayer on gold surfaces.[102] Control experiments performed by exposing PSi samples without Au NPs to benzenethiol showed no measurable fringe shift, since benzenethiol does not attach on silicon or silica.

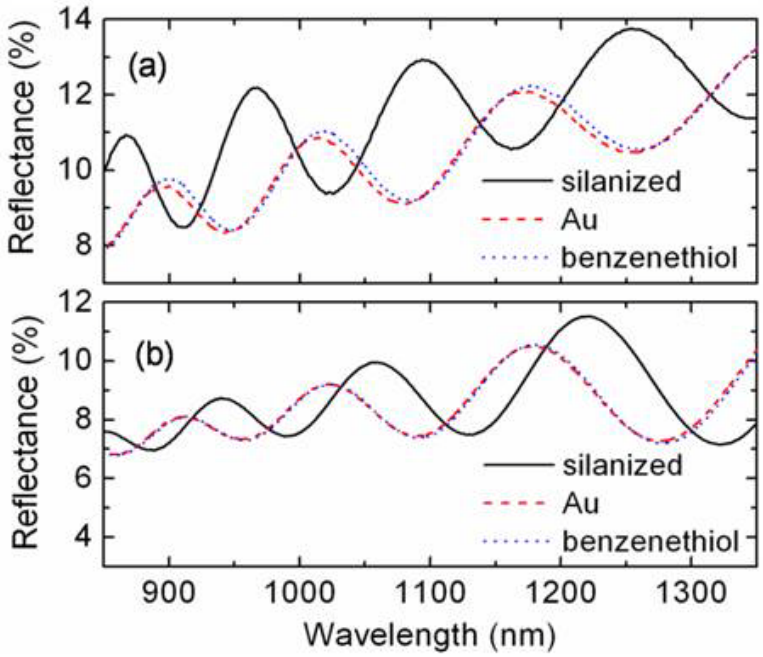

Figure 3-3 Reflectance spectra after each functionalization step: after silanization (solid line), after attachment of Au NPs (dashed line), and after adsorption of benzenethiol (dotted line) for a PSi sample coated with (a) small or (b) large Au NPs. (Adapted from Ref. [101])

Based on these reflectance measurements, we estimated the coverage and distribution of Au NPs and benzenethiol in both samples using the transfer matrix method and effective medium theory.[4] Following our prior work,[4, 54] we fit the measured 'silanized' interference fringes with a simulated spectrum: we assumed a PSi film thickness of 2.3 μm based on SEM measurements and then determined that the refractive index of silanized PSi was 1.88, which corresponds to a porosity of 64% calculated by the volume average method. In a similar manner, we determined the refractive index change of the PSi film after Au NPs decorated the surfaces and benzenethiol was attached to the Au NPs. In order to fit our simulated spectra to the measured reflectance curves, we found that the overall effective refractive index changes upon the infiltration of small Au NPs and subsequent adsorption of benzenethiol molecules on the NPs were 0.08 and 0.02, respectively, which suggests nearly 30% (±5%) Au NPs coverage inside the pores and approximately 60% benzenethiol coverage on the surface of the small Au NPs. Given the 8 nm (± 1 nm) spectral shift after benzenethiol attachment, we estimate the detection sensitivity of a sensor

based on a PSi film with small Au NPs is 400 (± 50) nm/RIU. For the larger Au NPs, simulations suggested that the 60 nm blue shift measured after infiltration was almost entirely due to complete Au NP coverage on top of the PSi film. With few large Au NPs infiltrated deep inside the pores, we expect negligible reflectance fringe shift after benzenethiol attachment, which is consistent with the measured result. The fringe shift is much more sensitive to small refractive index changes occurring inside the PSi film as opposed to on top of the film. Hence, the large Au NPs cannot be used for dual-mode sensing for the PSi sample with ~80 nm pore openings, but they do illustrate the size-selective filtering capabilities of PSi, as discussed in section 2.3.

3.3.2 Second sensing operation: SERS measurements

The second mode of sensing was investigated by SERS measurements to provide unique molecule identification.

Figure 3-4 (a) shows the experimental SERS spectra after adsorption of benzenethiol molecules on the small Au NPs coated PSi substrates. We believe the majority of the SERS signal originates from NPs on the top region of the PSi film because the SERS signal strength measured from separately prepared 100 nm thick PSi films infiltrated with Au NPs and benzenethiol was the same as the SERS signal strength from equivalent sized benzenethiol-coated Au NPs that impregnated the 2.3 μm thick PSi film as shown in Figure 3-5.

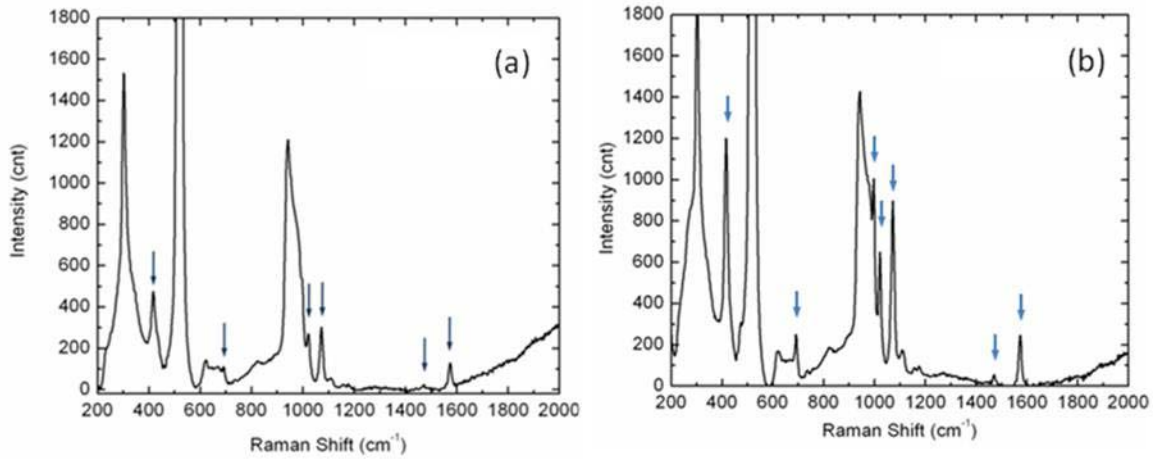

Figure 3-4 SERS spectra of benzenethiol molecules adsorbed on (a) small and (b) large Au NPs coated PSi sample. The substrates were immersed in 0.2 mM benzenethiol solution for 1 h. The benzenethiol peaks are indicated with arrows; other peaks are due to silicon. (Adapted from Ref. [101])

Moreover, by preparing an additional sample with only a roughened silicon surface, we found that only about 10% of the SERS signal was due to NPs on the surface as shown in Figure 3-5. For each sample that was prepared, five different spots were measured across the surface area. Similar SERS signal strengths were collected from all spots, indicating the uniformity of the functionalized surface of our SERS-active substrate. To examine the sensitivity of the SERS measurement, we exposed a small Au NPs coated PSi film to 1 μM benzenethiol in ethanol for 1 hour. A clear SERS signal was observed, which suggests that a detection limit below 1 μM is possible. We note that lower detection levels could be obtained by exposing the substrate to benzenethiol for a longer duration. Additionally, higher detection sensitivity and enhanced SERS signal may be achieved through further optimization of the ratio of Au NPs size and PSi pore size, or through utilizing an additional guided wave, such as waveguide mode (to be discussed in CHAPTER 4) in the vicinity of Au NPs.

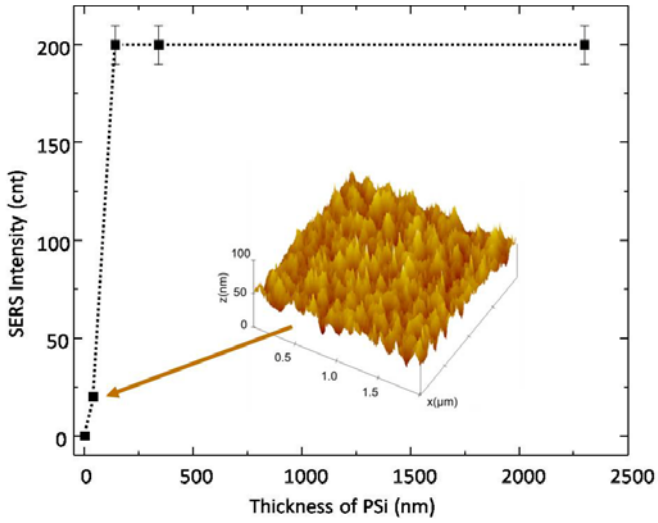

Figure 3-5 Dependence of SERS intensity with various thickness of PSi substrates

For comparison, the SERS spectra measured after adsorption of benzenethiol molecules on the large Au NPs-coated PSi substrate is shown in Figure 3-4 (b). The larger Au NPs give rise to a stronger SERS signal, as expected,[103] even though they do not significantly penetrate into the pores.

3.4 Conclusions

In summary, dual-mode sensing based on ~4.5 nm Au NPs coated PSi films has been presented. Measurements of the reflectance fringe pattern and SERS spectrum enabled both molecular quantification and identification. A detection sensitivity of ~400 nm/RIU was reported based on reflectance measurements after benzenethiol adsorption. Higher detection sensitivity may be achieved through utilizing resonant PSi structures such as microcavities and waveguides. The SERS spectrum showed that benzenethiol could be identified with a large area uniform intensity. The ease and low cost of fabrication, high detection sensitivity for small molecules, and integration of dual-modes of sensing using one substrate make the Au NPs coated PSi substrate attractive for use in a variety of sensing applications.

CHAPTER 4.

WAVEGUIDE MODE ENHANCED RAMAN SCATTERING ON GOLD NANOPARTICLE FUNCTIONALIZED POROUS SILICON WAVEGUIDES

4.1 Overview

Many SERS substrates solely utilize the localized surface plasmon (LSP) effect to enhance the electromagnetic field in the vicinity of nanoscale metallic structures. Aggregated metal nanoparticles, gold or silver coated nanoscale porous materials,[13, 101] carbon nanotubes,[104] as-prepared and modified nanoporous gold films[21, 22, 72, 73] have all been shown to be effective SERS substrates based on the strong LSP effect due to the random nanoscale features. Further, many LSP based artificially fabricated regular nanostructures containing periodic patterns such as precisely defined nanoscale metallic gratings,[27, 95, 105] tips,[58] gaps,[7, 29] holes,[32, 59] and other complex structures[30, 106] also have been demonstrated for SERS applications with significantly improved uniformity and reproducibility. Recently, using spatially confined guided modes to enhance the Raman scattering has attracted considerable attention, as they provide a more systematic and rational method for SERS substrate design with specific materials, and are also compatible with lithographic techniques and top-down approaches. Surface plasmon polaritons (SPP) are the most commonly utilized guided wave for SERS effects, and have been intensively investigated for enhancing the electromagnetic field close to the metallic planar surface and thus the Raman signal.[28, 107, 108] However, due to the large absorption loss induced by metals, such plasmonic based SERS substrates suffer from a broad resonance width and rapid field decay that limit the field intensity in the SERS active region. Guided modes from dielectric waveguide structures, however, can support a narrow resonance width with improved interaction times, and therefore are an effective, alternative approach for enhancing

Raman signals with low absorption loss. Under this principle, waveguide mode enhanced Raman scattering based on silicon and silicon nitride waveguides decorated with nanoparticles has been demonstrated to be an effective approach for achieving improved SERS substrates with narrow resonance linewidths.[109, 110] Recently, prism-coupled Bloch surface waves in a fully dielectric structure have also been theoretically investigated for potential SERS applications due to the similar strong localized field that can be generated and improved design freedom compared to SPP modes.[111] In this work, we demonstrate a hybrid substrate consisting of a grating-coupled porous silicon (PSi) waveguide decorated with colloidal gold nanoparticles (Au NPs) for SERS applications. In this structure, aggregated Au NPs on the top surface of a PSi waveguide provide a strong SERS signal due to the localized surface plasmon (LSP) effect, while the strongly confined guided wave in the waveguide layer can also be activated to further enhance the SERS signal at the resonance condition.

4.2 Materials and methods

4.2.1 SERS measurements

Benzenethiol was used as the test molecule for these SERS measurements. Benzenethiol is a Raman-active molecule that readily forms self-assembled monolayers (SAMs) on gold surfaces. SERS spectra were measured at normal incidence with a DXR Raman microscope (Thermo Scientific). A 0.9 mW diode laser with a wavelength of 780 nm was utilized for Raman excitation. A 10× magnification objective (NA = 0.25) with a large illumination spot (~3.1 μm) was used to focus the laser beam and collect the SERS signal over a large area, which promotes high reproducibility and uniformity of the SERS measurements. Data was collected with an integration time of 10 s and averaging of 5 scans.

4.2.2 Grating-coupled PSi waveguide functionalized with Au NPs

A schematic of the Au NPs coated PSi waveguide with a one dimensional (1D) grating coupler on the top surface is shown in Figure 4-1 (a), where *h* is the grating height, *d* is the thickness of waveguide layer,

Λ is the grating period, and f is the duty cycle, which is defined as the ratio between grating ridge width and the grating period. As discussed in section 1.2.2, a grating coupler is needed to couple incident light into a waveguide mode. For the Au NPs coated PSi waveguides, there is a momentum mismatch between both the incident laser light as well as the Stokes wavelengths from the Raman scattered light and the PSi waveguide mode. Here we design the periodic gratings on top of the samples such that the strongest 1st order diffracted light satisfies the coupling condition to allow light in/out of the waveguide mode near normal incidence. The two-layer PSi waveguide is fabricated by straightforward electrochemical etching of a p-type silicon wafer (<100>, 0.01 Ω cm). The top waveguide layer with d = ~130 nm is first etched at 5 mA/cm^2 current density for 20s resulting in an overall refractive index of ~2.05 and an approximately 15 nm average pore size. The bottom PSi layer, with a lower refractive index of ~1.26, is subsequently etched at 48 mA/cm^2 for 53s to form a ~1.5 μm thick cladding layer with ~40 nm pores. The PSi waveguide is then oxidized in an oven at 500℃ for 5 min to form a thin oxidation layer on pore walls for the subsequent attachment of 3-APTES. 1D grating lines are fabricated with a positive electron beam resist, ZEP 520A. ZEP is spin-coated at 6000 rpm on the oxidized PSi waveguide, followed by soft baking at 180℃ for 2 min, which results in a h = ~ 180 nm thick resist layer. The 1D grating coupler with f = ~35% is subsequently fabricated on top of the waveguide layer by a standard electron beam lithography procedure (JEOL JBX-9300FS, 100kV) at a dose of 300 μC/cm^2 and followed by development in Xylenes for 30 s.

The PSi waveguide is designed to only support the 0th order guided wave in transverse electric (TE) mode at 780 nm excitation for simplicity. The 5 nm Au NPs are chosen because this size Au NP can conform to the morphology of the silicon matrix of PSi very well, which guarantees a uniform Au NPs deposition on the PSi surface, while not substantially filling the pores and disrupting the guided mode. Importantly, as the size of Au NPs is small, they do not perturb the resonance condition of the waveguide mode significantly.

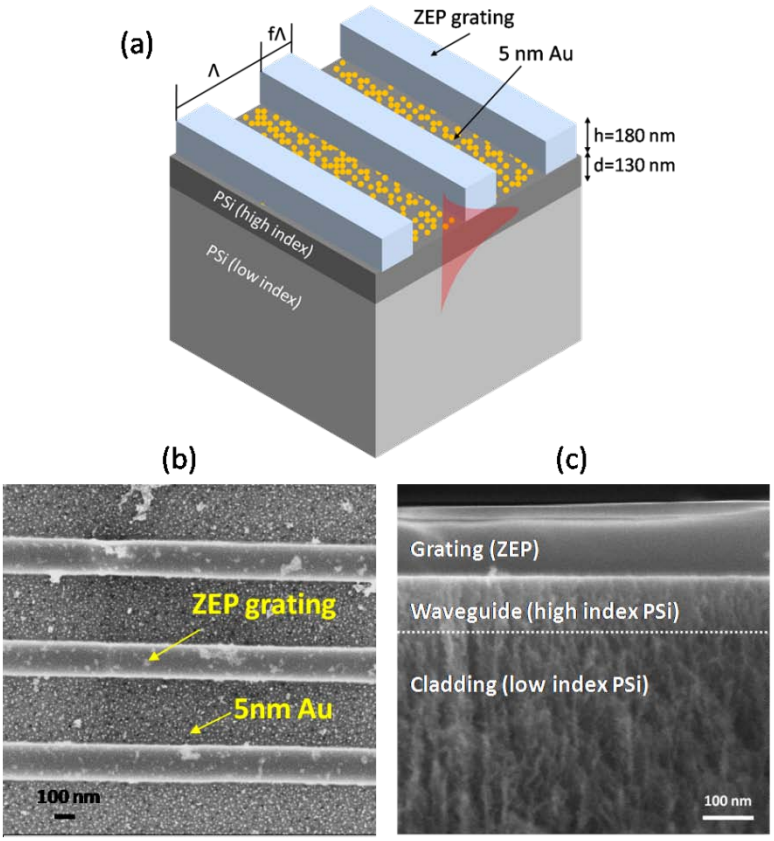

Figure 4-1 (a) Schematic configuration of a 1D grating-coupled Au-coated PSi waveguide. (b) Plan-view SEM image of 5 nm Au NPs coated grating coupled PSi waveguide. (c) Side view SEM image of the PSi waveguide covered with a ~180 nm thick ZEP resist layer. (Adapted from Ref. [112])

In order to attach Au NPs on top of the fabricated substrates, the oxidized samples with the grating couplers were exposed to a 4% 3-APTES solution in water and ethanol for 20 minutes followed by a baking process at 100℃, in a manner similar to what has been reported in CHAPTER 3, section 3.2.3.[100, 101] Here, the immobilized 3-APTES is acting as a linker molecule for the subsequent Au NPs attachment. The silanized samples were then immersed in the colloidal Au NPs solution for 12 hours to form a uniform deposition of Au NPs on top of the PSi waveguide. Note that the 15 nm pore openings of the waveguide layer are relatively small for the ~5 nm Au NPs, thus most Au NPs reside on the top surface and only few Au NPs can infiltrate deep inside the pores. After the deposition of Au NPs, samples were thoroughly rinsed with DI water and dried with nitrogen gas. A top view SEM image of a grating-coupled Au NPs coated PSi waveguide, shown in Figure 4-1 (b), reveals the large-area uniformity of

aggregated Au NPs on top of the PSi surface, which was not observed on the nonporous grating ridge regions due to the lack of porous structure. Figure 4-1 (c) shows side view SEM of the PSi waveguide with a ~180 nm ZEP photo resist layer on the top surface.

4.2.3 Results and discussions

4.2.3.1 Simulation and SERS measurements

Figure 4-2 (a) shows SERS spectrum of benzenethiol adsorbed on a sample of Au NPs coated PSi waveguide with a properly designed grating coupler (h=180 nm, Λ=525 nm, f=35%) on the top surface (red curve). As a comparison, the SERS spectrum of benzenethiol on the same Au NPs coated PSi substrate but with no grating coupler is also measured (blue curve). Both sample regions are immersed in a 10 mM benzenethiol solution for 1 hour to form a SAM of benzenethiol on the surface of the Au NPs. All resolvable Raman bands of benzenethiol are marked with arrows, and other bands are due to silicon. Note that for the sample with no grating coupler, the SERS signal is completely due to the LSP effect from the aggregated Au NPs on the top surface, similar to the single layer interferometer in CHAPTER 3. While with the presence of a grating coupler (Λ=525 nm), much stronger SERS signals for all Raman bands are observed, which indicates field enhancement from excitation of the waveguide mode. For example, the 1070 cm-1 band shows a 20 times higher peak intensity compared to that measured from the sample with no grating, even though 35% of the top surface is not used as a SERS active region due to the presence of the resist grating.

Note that with the current experimental configuration, Raman light with other Stokes wavelengths can also be coupled out and detected at other angles within the ~15 degree detection angular range, therefore the detected SERS spectrum from a single sample with specific grating period includes all the contributions from detectable Stokes wavelength resonances within the ~15 degree angular range. Figure 4-2 (b) shows the simulated wavelength-interrogated reflectance curve at normal incidence based on this SERS substrate without considering the presence of small NPs in the region of grating grooves. With the presence of Au NPs, the resonance will become wider, which will cover a broader wavelength

range and perhaps slightly blue shift the resonance peak closer towards 780 nm. A resonance position at 850 nm corresponds to the 1070 cm^{-1} Raman band for the 780 nm excitation, and the corresponding near field intensity distribution at resonance peak is shown in the inset of Figure 4-2 (b), indicating a strong confined field in the waveguide layer. Note that benzenethiol is only adsorbed on the Au NPs deposited on top of PSi, therefore cannot interact with the strongest part of the confined field. However, the intensity of the leaky field on the surface associated with the waveguide mode is still relatively strong compared to the peak field intensity in the waveguide layer. From the field distribution shown in the inset of Figure 4-2 (b), we notice that the Au NPs on top of grating ridges have no significant contribution to the strong SERS signal since the field intensity in those regions decays to a low level. We also notice from Figure 4-1 (b) that due to the lack of porous structure on grating ridges, no uniform Au NPs aggregation is formed. Therefore, relatively sparsely distributed small ~5 nm Au NPs on top of grating ridges will not lead to resolvable SERS signal.

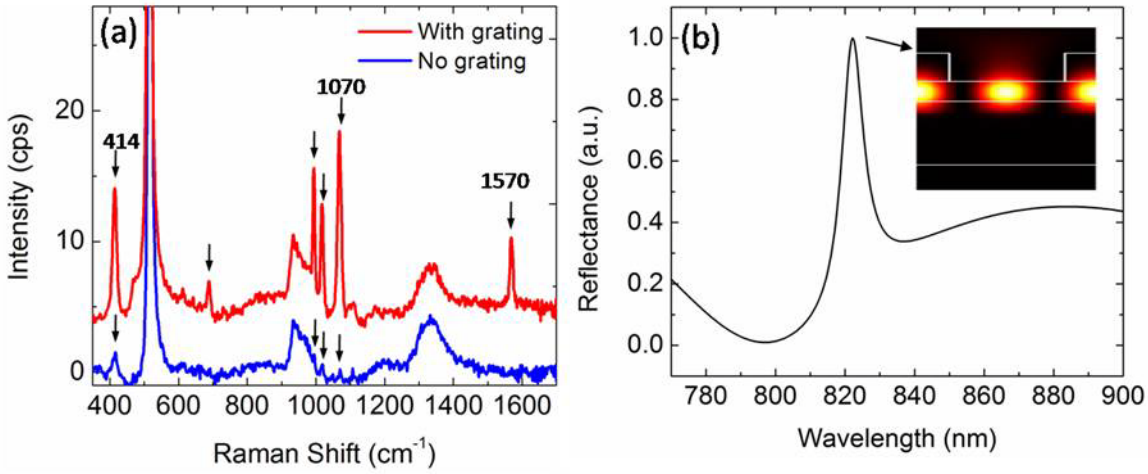

Figure 4-2 (a) SERS spectra of benzenethiol measured on Au NPs coated PSi waveguides with (red) and without (blue) grating coupler on the top surface. All the detectable Raman bands of benzenethiol are marked with arrows for both substrates, and the remaining bands are due to silicon. Three typical Raman bands of benzenethiol (414, 1070, 1570 cm^{-1}) are also indicated. (b) Simulated wavelength-interrogated reflectance of a grating-coupled PSi waveguide with 525 grating period. Inset shows the corresponding field intensity distribution at resonance peak. (Adapted from Ref. [112])

4.2.3.2 Selective amplification

Compared to the spectral resonance width of the waveguide mode, benzenethiol has a relatively broad Raman spectrum, which covers a wavelength range from 805 nm to 888 nm for excitation at λ_0 = 780 nm. Thus, the activated waveguide resonance is not be able to spectrally cover the entire Raman spectrum of benzenethiol. Therefore, various grating periods ranging from 400 nm to 600 nm are prepared in order to efficiently enhance various Stokes wavelength components using waveguide modes. Figure 4-3 (a) illustrates the trends of SERS intensities with various grating periods for three typical Raman bands of 414 cm^{-1} (squares), 1070 cm^{-1} (circles), and 1570 cm^{-1} (triangles), which respectively correspond to Stokes wavelengths of 805 nm, 857 nm, and 888 nm at λ_0=780 nm. It is clear that for grating periods smaller than 450 nm, Raman intensities of all three Raman bands are relatively low, which indicates that the momentum provided by the grating is too large to match the guided mode wave vector from normal incidence. By increasing the grating period, SERS intensities for all three Raman bands increase and the maximal intensity for each Raman band is respectively achieved at a specific grating period with higher grating periods being required for higher Stokes wavelengths. For example, the 414 cm^{-1} band corresponds to 805 nm at 780 nm excitation, and this wavelength is most efficiently activated near normal incidence with the choice of a 500 nm grating period. Similarly, the maximal band intensities for the higher wavelength Raman bands of 1070 and 1570 cm^{-1} are respectively achieved at the larger grating periods of 525 and 600 nm, which is clear evidence that the resonance wavelength of the waveguide mode red shifts with increasing grating period. Figure 4-3 (b) shows a zoomed-in view of three Raman bands for various grating periods: 500 nm (black), 525 nm (red), and 600 nm (green). A clear band-selective amplification of the various Raman bands can be observed from their relative band intensity at each grating period. In accordance with Figure 4-3 (a), the strongest band intensity for Λ = 500 nm is achieved at the 414 cm^{-1} band and decreasing band intensities are observed at higher Stokes wavelengths, while for Λ=525 nm and Λ=600 nm, the strongest band intensity is respectively achieved at 1070 and 1570 cm^{-1}, which is further strong evidence for the red-shift of resonance wavelength with increasing grating period.

We also notice that the 414 cm^{-1} band shows the strongest overall band intensity compared to the other two Raman bands at higher Stokes wavelength. This can be explained as the resonance at lower Stokes wavelengths also spectrally overlaps with the excitation wavelength, which also contributes to the SERS signal. More obvious selective amplification effects can be expected by using a microscope objective with a lower NA because fewer Stokes wavelength components can be excited or detected in the waveguide mode within a smaller angular range.

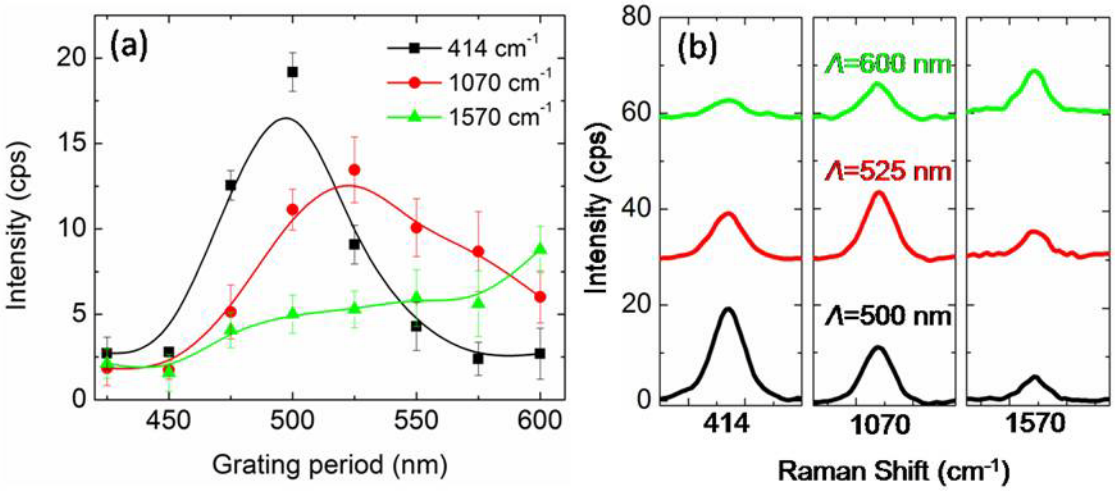

Figure 4-3 (a) Dependence of Raman intensities at 414 cm-1, 1070 cm-1, and 1570 cm-1 bands as a function of grating period. (b) Zoomed-in SERS spectra of various Raman bands of benzenethiol measured at various grating periods. A clear amplification of various Raman bands was observed at different grating periods due to the position of activated waveguide mode resonance. (Adapted from Ref. [112])

4.2.3.3 Detection limit

In order to characterize the sensing capability of this Au coated grating coupled PSi waveguide structure, diluted benzenethiol solutions with concentrations ranging from 5 µM to 1 mM were prepared. 2 µL of each diluted benzenethiol solution was drop-casted on the sample surfaces and dried in air to form a spot with ~1 cm diameter. Figure 4-4 shows a comparison of SERS spectra for benzenethiol measured from samples with Λ = 525 nm at various concentrations, and the inset shows the intensity (log scale) of the 1070 cm^{-1} band as a function of benzenethiol concentration, ranging from 0.01 - 1 mM. It can be seen that some of benzenethiol bands still can be resolved at a concentration as low as 5 µM which

indicates a detection limit of 5-10 μM of benzenethiol. Note that due to the reduced pore size of the PSi waveguide layer in this waveguide structure, the ~5 nm Au NPs can only be deposited on the top surface without a deep infiltration inside the pores, which results in a different metallic surface morphology compared to the Au NPs coated single layer PSi with larger pores (~80 nm) described in CHAPTER 3. In addition, the objectives used in the two cases are 100× and 10×, respectively, which provide different incident angular ranges. Therefore, the reported detection limits of benzenethiol on both structures cannot by directly compared between CHAPTER 3 and CHAPTER 4. The relevant comparison is made in Figure 4-2.

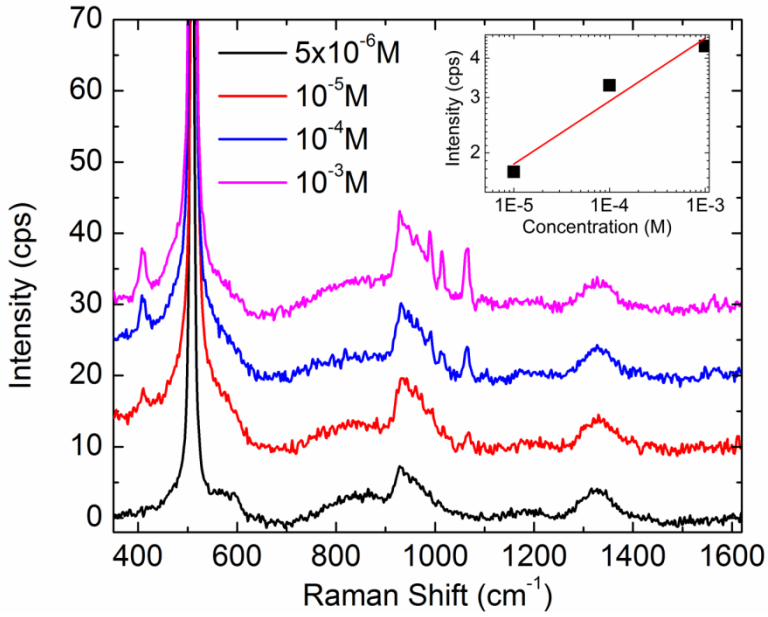

Figure 4-4 Comparison of SERS spectra of benzenthiol with various concentrations on grating-coupled Au-coated PSi waveguides. Inset shows the log-log plot of Raman intensity at the 1070 cm^{-1} band with various concentrations. A detection sensitivity of <5μM was achieved.

4.3 Conclusions

In conclusion, we have demonstrated the Au NPs coated PSi waveguide with a 1D grating coupler as an effective SERS substrate. The aggregated Au NPs on the porous surface provide the strong LSP effect, and the waveguide mode, activated via the grating coupler, provides an additional field enhancement and

thus more than 20 times stronger SERS response compared to the substrate without a grating coupler. Unlike what is achievable with conventional LSP devices with very broad resonant features, which cannot achieve selective amplification, a clear selective amplification of various Raman bands was observed due to the low loss of the dielectric waveguide and the resulting narrower resonance width. A 5-10 μM detection limit was achieved for benzenethiol deposited on the substrate surface. Note that the detection limit of this SERS substrate is only based on a 5 nm thick Au NPs layer. Porous structures with optimized pore openings might enable deeper infiltration of Au NPs, which should lead to a stronger SERS signal as discussed in CHAPTER 3, section 3.3.2. Similar SERS structures based on other dielectric materials with optimized design might lead to stronger SERS enhancement. For example, other porous materials with higher allowable index contrast between the guiding and cladding layer might lead to stronger field confinement, and therefore stronger near field in the waveguide modes. Also, this additional waveguide mode might be adapted in alternative non-porous systems with various types of precisely defined LSP nanostructures.

CHAPTER 5.

PATTERNED NANOPOROUS GOLD AS AN EFFECTIVE SERS SUBSTRATE

5.1 Overview

Numerous LSP based metallic nanostructures have been intensively investigated for SERS, such as silver or gold-coated silicon nanopores[13, 101] and silicon nanopilars,[113] arrays of nanodomes,[7] nanoparticles,[24] and nanogaps,[29] where significantly enhancing the Raman signal strongly relies on the laterally confined strong field in the deep sub-wavelength regions. However, these small features (e.g. on the order of a few nanometers) either require relatively complex, expensive, and high resolution fabrication processes, such as electron beam lithography and lift-off procedure which is often low throughput, or a manual search for 'hot spots' on the randomly oriented nanoscale metallic structures. The surface plasmon polariton (SPP), meanwhile, is a propagating plasmonic mode at a planar noble metal and dielectric interface, and can produce an overall strong field enhancement uniformly across the substrate surface where molecules are attached, therefore enabling a strongly enhanced SERS signal and higher uniformity. Unlike the waveguide mode utilized in CHAPTER 5, which is based on total internal reflection, the SPP is based on collective surface electron oscillations and can only be activated under TM-polarized light. A strong SPP effect can be easily activated at designated wavelengths via the optimization of the coupling configuration. Moreover, several SERS templates have recently taken advantage of the SPP field enhancement in combination with a LSP effect to further amplify the SERS response.[27, 107, 108] Recently, nanoporous gold (NPG) became a particularly attractive SERS substrate due to its low-cost and straightforward fabrication, as well as its relatively uniform SERS enhancement across large areas. As-prepared NPG consists of a nanoscale sponge-like porous structure that provides a large surface area for molecule binding and supports LSP over a broad wavelength range.[114] Various modified NPG films,

such as NPG with nanoscale wrinkles,[73, 115] fractures,[72] and ultra small pores,[21, 22] have been reported to promote improved SERS intensity due to the increased electromagnetic field intensity, or improved LSP activity, in the vicinity of the nanoscale pores and sharp features. Considered as a metamaterial, as-prepared NPG films also have the appropriate optical constants to support SPP in the near infrared (NIR) wavelength range, and both prism- and grating-coupled SPPs on NPG films have recently been reported for refractive index-based plasmonic sensors with high detection sensitivity.[46, 47]

In this work, we report an easy-to-fabricate, uniform, and highly sensitive SERS-active substrate that combines the self-organized and highly interacting nanoscale morphology of NPG with the advantages of reproducibly nanopatterned periodic structures. NPG is a low cost material (~3 cents per cm^2 of external surface area) that can be fabricated in a straightforward manner and chemically bound as a thin film to glass or gold supports.[70] Although as-prepared NPG films have been reported to show a strong SERS signal,[20, 22, 114] we will show that utilizing a straightforward process to imprint two-dimensional (2D) square grating patterns in NPG films significantly enhances the SERS signal and further yields uniform SERS substrates, eliminating the need to search for hotspots.

5.2 Materials and methods

5.2.1 Fabrication of nanoporous gold

Fabrication of nanoporous gold (NPG) films has been demonstrated using a straightforward and scalable process.[70] In this work, as described in section 1.3.2, a $Ag_{50}Au_{50}$ film with thickness of approximately 100 nm is dealloyed in 70% HNO_3 for 15 min at room temperature to dissolve the silver. The dealloyed NPG is then transferred from the HNO_3 solution to DI water for rinsing using a glass slide. Finally, the NPG is transferred to a 1,6-hexandedithiol-modified gold substrate on a silicon support for robust anchoring. The feature size of the NPG produced by this method can be controlled by adjusting the

dealloying time. Based on SEM imaging, our NPG has pore openings of approximately 15 nm after the 15 min dealloying period at room temperature.

5.2.2 Imprinting method for nanoporous gold gratings

Our NPG SERS substrates are fabricated by imprinting as-prepared NPG films using a newly developed one-step stamping technique, 'direct imprinting of porous substrates' (DIPS).[116] Figure 5-1 (a) shows the schematic fabrication process of our patterned nanoporous gold (P-NPG) SERS substrate. Reusable silicon stamps (area = 9 mm^2) consisting of 2D gratings with variable periodicity were first fabricated using standard electron beam lithography and reactive-ion etching techniques, although projection lithography could also be used, if available.[116] The silicon stamp was then pressed against the NPG substrate by applying a force in the range of 4.5×10^2 N – 2.7×10^3 N to fully transfer the 2D grating pattern into the NPG. In addition to creating the 2D grating pattern, the DIPS process simultaneously forms a locally compressed NPG network, which we will show also contributes to the significantly enhanced SERS intensity that is observed. Figure 5-1 (b) shows a plan view SEM image of a representative surface morphology of a P-NPG structure prepared at 1.5×10^3 N with grating period Λ = 350 nm and duty cycle f = 70%. The SEM image reveals that the pore openings on the grating ridges (unstamped region) are unaffected, while the pore openings on the grating grooves (stamped region) are reduced in size due to compression. The silicon stamp can be reused multiple times without any degradation of the pattern transfer,[116] which makes our P-NPG SERS substrates highly reproducible and cost-effective, especially compared to other nano- and micro-scale patterned SERS substrates.

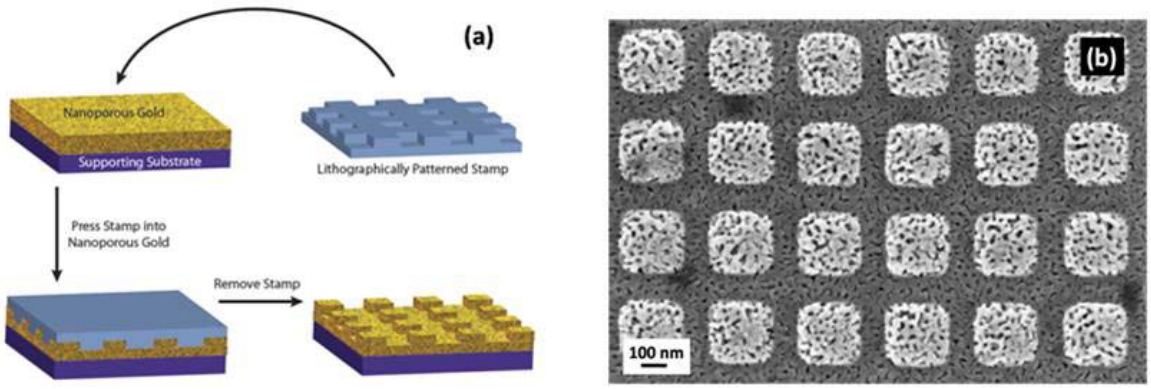

Figure 5-1 (a) Schematic of the fabrication process for P-NPG. A silicon stamp lithographically patterned with a 2D grating is pressed into the surface of NPG that is attached to a supporting substrate. Removal of the stamp yields the 2D P-NPG SERS-active substrate. (b) Plan view SEM image of a representative surface morphology of a P-NPG structure prepared at 1.5×10^3 N with grating period Λ = 350 nm and duty cycle f = 70%. (Adapted from Ref. [117])

5.2.3 SERS measurement

The SERS enhancement of our P-NPG substrate was investigated through the detection of a monolayer of adsorbed benzenethiol molecules. Each P-NPG sample was immersed in a 0.2 mM benzenethiol solution in ethanol for 1 h, and the samples were subsequently rinsed with ethanol and dried with nitrogen. SERS spectra were collected over an angular range of $2\theta \approx 128°$ (NA = 0.9) using an XploRA 730 Raman microscope (Horiba Jobin Yvon) with 100× magnification, integration time of 20 s, and accumulations of five scans. The Raman microscope was run under low power of 0.9 mW from a 780 nm diode laser with a spot size on the order of 1 μm. Normal incidence of light was used in all SERS measurements, which enabled stable and reproducible SERS signals.

5.2.4 Reductive desorption measurements

Reductive desorption of benzenethiolate molecules in a deaerated phosphate buffer (pH 8.3) was performed in order to quantify the number of molecules per geometric area adsorbed to various SERS substrates. Using this technique, the accessible surface area provided by a P-NPG substrate as compared to a planar gold substrate and to Klarite®, a commercially available gold standard substrate often employed in surface enhanced Raman spectroscopy, was determined. It is assumed that the area

occupied by a benzenethiolate molecule is identical on the three substrates; hence, the integrated current measured by the reductive desorption technique scales with the relative surface area of the substrates. Voltammetric scans were performed with a Gamry Instruments CMS300 electrochemical system using a Ag/AgCl reference electrode, a gold counter electrode, and a working electrode that consisted of P-NPG that had been exposed to a 1 mM solution of benzenethiol in ethanol for at least 1 h. Two independently prepared samples of P-NPG substrates were used for the experiments. For comparison, a gold-coated silicon wafer and a Klarite® substrate that were similarly exposed to a 1 mM ethanolic solution of benzenethiol were also used as working electrodes. Likewise, two independently prepared samples were used for each control. The potential was swept from 0 to -1.2 V, with a scan rate of 200 mV/s.

5.3 Results and discussion

5.3.1 SERS measurements from 2D P-NPG with various grating periods

5.3.1.1 Surface uniformity

Figure 5-3 (a) show the SERS spectrum from a P-NPG substrate with a grating period of 650 nm along with that from an as-prepared NPG film. A significant enhancement of the SERS signal intensity is observed for the P-NPG sample. Since the spot size of the laser beam used for the SERS measurements is larger than both the small pores of the NPG film and the imprinted grating squares, reproducible and uniform spectral intensity was observed across large areas. Figure 5-2 shows SERS spectra of benzenethiol collected from seven different spots within a >100 μm^2 area of a 2D P-NPG substrate with grating period of 650 nm. The intensities of the SERS signals are stable with <10% intensity variation across the different measurement spots, which demonstrates the excellent uniformity of the P-NPG substrate.

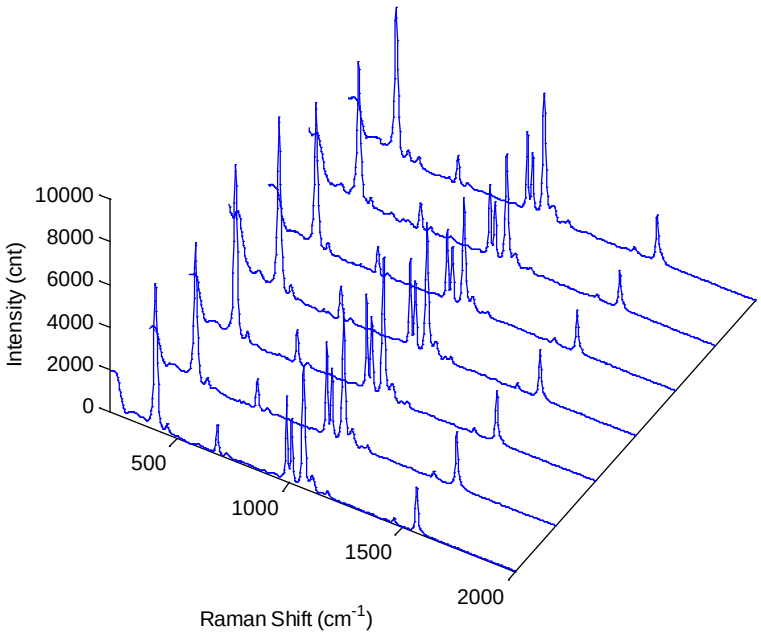

Figure 5-2 SERS spectra of benzenethiol measured from seven different spots randomly selected within a >100 μm^2 area of a 2D P-NPG substrate with grating period of 650 nm. (Adapted from Ref. [117])

The uniformity of the P-NPG substrate was limited primarily by nanoscale wrinkles on the NPG film, which leads to the local variations in thickness, porosity and pore size of NPG film. The SERS intensities collected from three identically prepared P-NPG substrates varied by approximately 10-15%, again likely due to non-uniformity in the NPG film to which DIPS was applied, and repeated SERS measurements on a specific region of a P-NPG substrate exhibited no detectable SERS intensity change over the course of 15 days. In order to understand the origin of the enhancement due to the patterning of the NPG film, two sets of experiments were performed to isolate the influence of the grating pattern and the influence of the NPG film densification that occurs during the DIPS fabrication process.

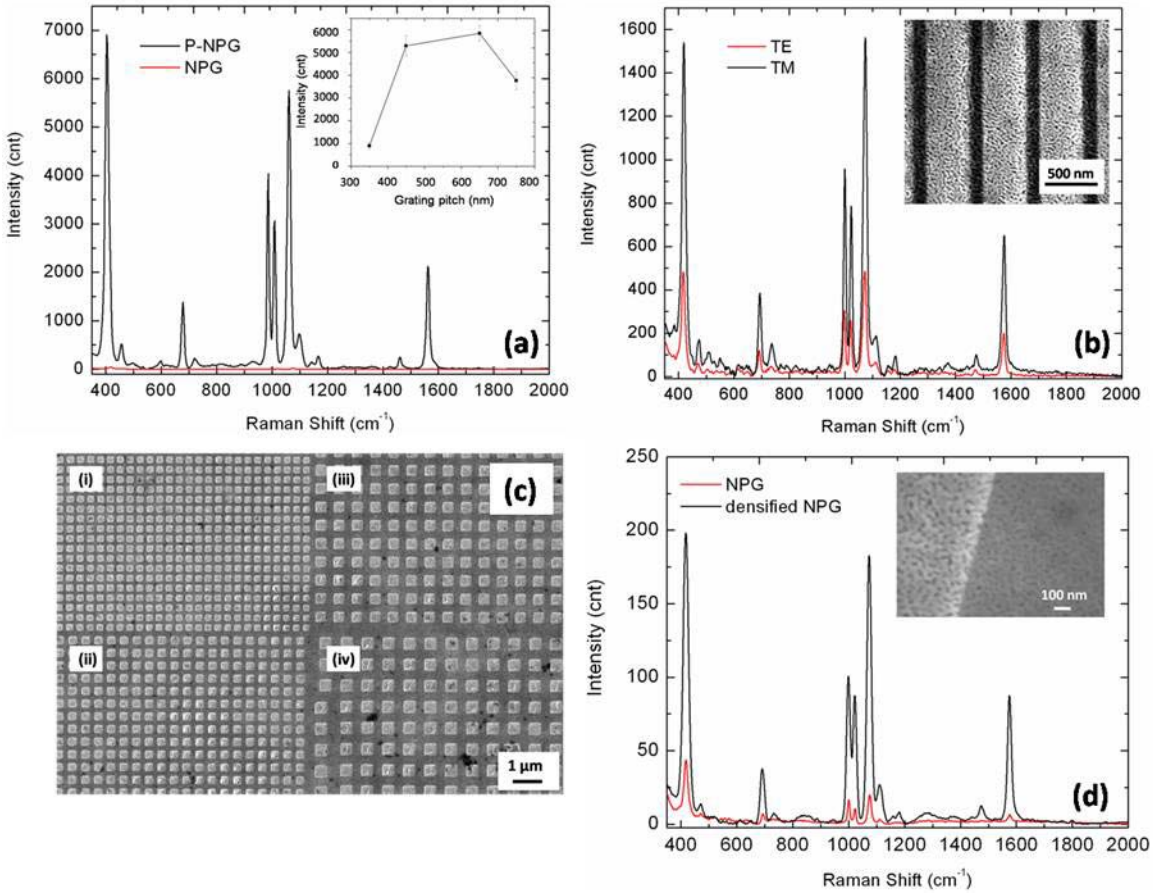

Figure 5-3 (a) SERS spectra of benzenethiol molecules adsorbed on as-prepared NPG (red) and a 2D P-NPG substrate with grating period of 650 nm (black). Inset shows the relationship between the grating period and the SERS intensity at the band of 1071 cm^{-1}. (b) SERS spectra of benzenethiol molecules adsorbed on 1D P-NPG substrate with 550 nm grating period, activated by TE (red) and TM (black) polarized light, respectively. (c) SEM images of stamped P-NPG SERS substrates with grating periods of (i) 350 nm, (ii) 450 nm, (iii) 650 nm, and (iv) 750 nm, respectively. The air duty cycle of all the samples is approximately 40% (±10%). (d) SERS spectra of benzenethiol adsorbed on as-prepared NPG (red) and unpatterned, densified NPG (black). Inset shows the SEM image of as-prepared NPG (left) and densified NPG (right). (Adapted from Ref. [117])

5.3.1.2 Role of SPP

In order to determine the potential influence of the surface plasmon polaritons (SPP) mode, P-NPG samples with various grating periods ranging from 350 - 750 nm were fabricated using the DIPS process (Figure 5-3 (c)). As shown in the inset of Figure 5-3 (a), we observe a variation in the SERS response depending on grating period. The SERS intensity reported for each grating period is the average SERS intensity measured on 8-10 different spots on each sample. It has been reported that a grating period-

dependent SERS response from grating-based SERS substrates can be attributed to the activation of a SPP mode, which we believe also plays a role in the grating-dependent SERS response of the P-NPG substrates.[5, 27] Further evidence suggesting the important role of the SPP is found when comparing the SERS response of a simple 1D P-NPG grating (Λ = 550 nm) under TE and TM excitation (Figure 5-3 (b)). Activation of a SPP mode is only expected for TM polarized light, and we indeed observe a stronger SERS response under TM excitation. Note that the 1D gratings are utilized since 2D gratings are polarization-independent for Raman laser excitation at normal incidence. 1D P-NPG substrates with other grating periods ranging from 450 to 950 nm are also investigated under both TE and TM excitations, as shown in Figure 5-4. The maximum TM excited SERS intensity is achieved around Λ = 550 nm. The SERS responses for larger grating periods of 750-950 nm are found to be comparable between TE and TM excitation, suggesting that these grating periods cannot satisfy the SPP excitation condition and that the anisotropy of the 1D structure is not the dominant factor in the polarization-dependent SERS intensity measured at shorter grating periods.

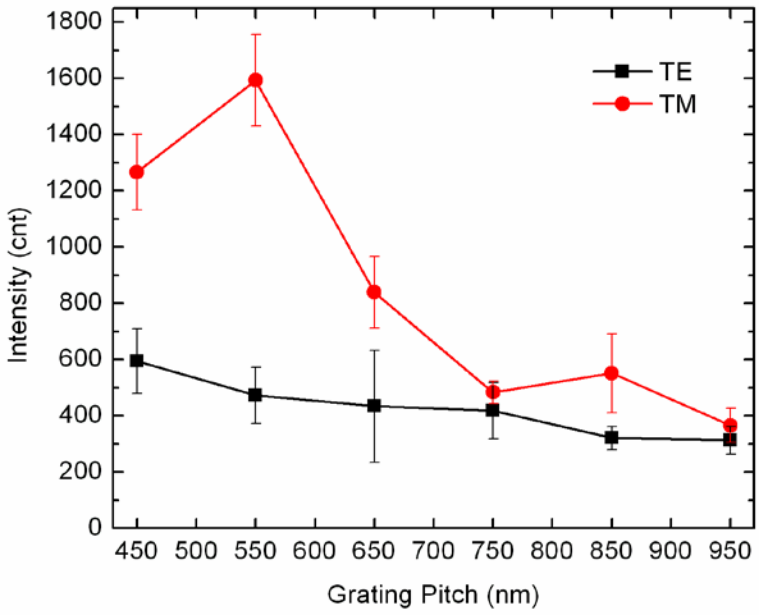

Figure 5-4 The relationship between the 1D grating period and the SERS intensity at the benzenethiol vibrational band of 1071 cm^{-1} under TE (black squares) and TM (red circles) excitation. (Adapted from Ref. [117])

Generally, the maximum SERS signal is detected at an emission angle that corresponds to the plasmon resonance angle. However, since our measurement configuration available for this study utilizes a high magnification objective with a large numerical aperture, it is not possible to accommodate narrow angular selection for the observation of the highest SERS enhancement. Hence, our P-NPG structures were fabricated with relatively deep gratings (~60 nm, as determined by AFM) that enable activation of a SPP and collection of the SERS emitted signal over a broad angular range.[27] The SERS response trend shown in the inset of Figure 5-3 (a) suggests that activation of a plasmon is possible for grating periods between 450-750 nm, but not likely for 350 nm. We note that the measurable SERS response does depend on the grating depth, and further tuning of the grating height, as discussed in CHAPTER 6, can lead to a stronger SERS signal. . We also note that P-NPG substrates with smaller grating periods results in larger available surface area within the excitation laser beam, which leads to a ~15% difference in surface area available for benzenethiol adsorption between 350 nm gratings and 750 nm gratings. The number of benzenethiol molecules adsorbed to a substrate contributes linearly to the SERS intensity;

therefore, the trend shown in Figure 5-3 (a) cannot be solely due to the different number of adsorbed molecules on each substrate.

5.3.2 SERS measurements from densified NPG

The potential contribution of the densified NPG network surrounding the NPG grating squares to the SERS enhancement from P-NPG substrates was isolated by imprinting a NPG film with an unpatterned 9 mm^2 silicon square, which effectively densified the porous substrate to ~30% of its original thickness without imprinting any grating pattern. Figure 5-3 (d) illustrates the SERS spectra of benzenethiol adsorbed on as-prepared NPG and on uniformly densified NPG. The inset shows the SEM image of the interface between the imprinted (right) and as-prepared NPG film (left). The surface topology and corresponding SERS response of the densified NPG film is significantly modified by the applied pressure during the DIPS process; the densified NPG shows ~10 - 15 times higher SERS intensity than that of the as-prepared NPG substrate. Although use of the unpatterned stamp results in a reduced imprint depth compared to the 1D or 2D grating due to the larger contact area, variations in the SERS intensity measured with slightly different imprint depths were far less than the one order of magnitude SERS enhancement over as-prepared NPG substrates. We believe the enhancement produced by densified NPG can be partly attributed to nanoscale morphological changes. Under the pressure applied during the DIPS process, the pore size and distance between neighboring gold ligaments is decreased, promoting stronger localized fields at pores where SERS-active molecules are attached. Previous work similarly showed that NPG films with smaller pores,[21, 22] and compressed metal pellets,[118] generate stronger SERS signals due to the enhancement of localized electromagnetic fields. It is worth mentioning that besides the reduced pore size, the densification effect also leads to an increased metallic behavior of NPG film, which will be further demonstrated via the dielectric constant measurements in CHAPTER 6.

By examining the peak heights of the SERS spectra in Figure 5-3 (a) and (d), we can compare the relative contributions of densified NPG and the 2D grating pattern to the overall SERS enhancement exhibited by our P-NPG substrates. While straightforward densification contributes approximately one

order of magnitude SERS enhancement over as-prepared NPG, the dominant contribution to the overall SERS enhancement is due to the imprinted grating patterns, providing two orders of magnitude enhancement.

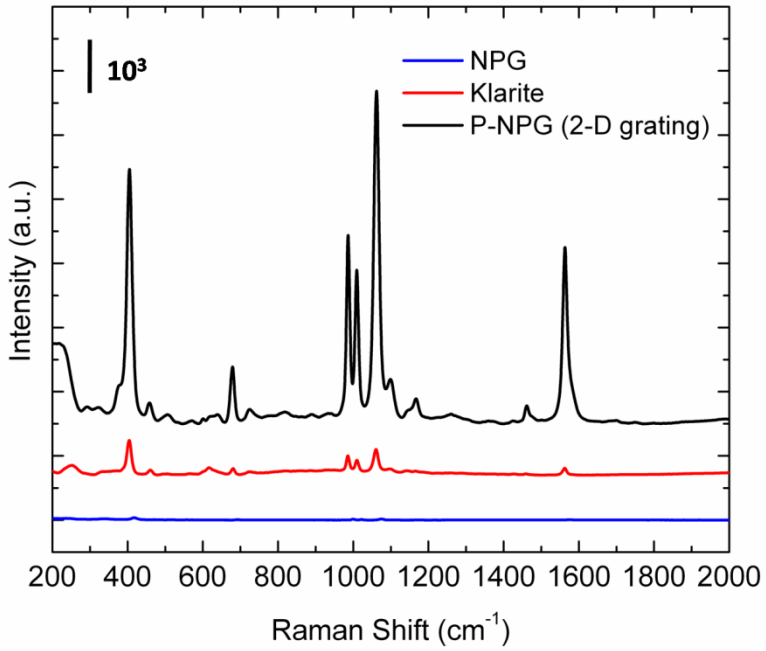

Figure 5-5 SERS spectra of benzenethiol molecules adsorbed on NPG (blue), Klarite® commercial SERS substrate (red), and 2D P-NPG SERS substrate with 650 nm period and air fill fraction of ~30% (black). The spectra are offset for ease of comparison. The 2D P-NPG SERS substrate exhibits one order of magnitude higher SERS enhancement compared to the Klarite® substrate. (Adapted from Ref. [117])

5.3.3 Calculation of SERS enhancement

In order to estimate an overall SERS enhancement factor relative to non-enhancing substrates, we compare the SERS signal from our $\Lambda = 650$ nm grating period P-NPG substrate with a Klarite® commercial SERS substrate, as shown in Figure 5-5. The Klarite® SERS substrate consists of gold-coated textured silicon (regular arrays of inverted pyramids ~1.5 μm wide and ~1 μm deep) mounted on a glass microscope slide. The enhancement factor for the inverted pyramid structure of Klarite® substrates relative to a non-enhancing surface is rated to have a lower bound of ~10^6.[119] Using this lower bound

enhancement factor specified for Klarite® as a reference, we estimate the SERS enhancement factor of our Λ = 650 nm P-NPG substrates using the following equation

$$EF_{P-NPG} = EF_{Klarite} \cdot \frac{N_{Klarite}}{N_{P-NPG}} \cdot \frac{I_{P-NPG}}{I_{Klarite}}, \quad (5.1)$$

where EF_{Klarite} is taken as 10^6, N_{Klarite} and $N_{\text{P-NPG}}$ are the estimated number of benzenethiol molecules adsorbed on the Klarite® and P-NPG samples, respectively, and $I_{\text{P-NPG}}$ and I_{Klarite} are the respective SERS intensities at the 1070 cm^{-1} band, one of the well-known and most distinct benzenethiol Raman signatures. Voltammetric scans for the reductive desorption of benzenethiol molecules were performed to estimate the number of adsorbed benzenethiol molecules on P-NPG and Klarite substrates, as well as on a planar gold electrode for comparison. As shown in Figure 5-6, each voltammetric scan exhibits two cathodic current peaks that we ascribe to thiolates bound at different surface sites on these gold surfaces.[120] As compared to the planar gold electrode, the P-NPG electrode shows broader current peaks that we attribute to the different gold surface structures within this nanoporous metal film. Integration of these peaks is used to obtain a charge that is proportional to the number of benzenethiolate molecules desorbed from the surface. For planar gold, the integrated charge of the two peaks (56 ± 2 μC/cm^2) corresponds to an average of 3.5 × 10^{14} molecules/cm^2, which is similar to the value of 3.2 × 10^{14} molecules/cm^2 reported by Wan et al.[121] and translates into a fractional coverage of 0.25. The integrated charges for the nanoporous gold and Klarite® were 108 ± 1 and 75 ± 3 μC/cm^2, respectively. The average integrated charge ratio of stamped nanoporous gold to planar gold, both shown on a basis of 1 cm^2 of geometric area, was approximately 1.9, meaning that the stamped electrode has ~90% more bound benzenethiolate molecules than does the planar gold electrode. The reductive desorption of benzenethiolate molecules from Klarite® exhibits two broad current peaks that are shifted to lower potentials than those on nanoporous gold or planar gold. The comparison between the stamped nanoporous gold substrate and Klarite® resulted in a current ratio of approximately 1.4, suggesting that 40% more molecules are adsorbed onto the P-NPG sample such that $N_{\text{Klarite}}/N_{\text{P-NPG}}$ = 0.71. From

Figure 5-5, the measured SERS intensity ratio at 1070 cm^{-1} ($I_{P\text{-}NPG}/ I_{Klarite}$) is 14. Therefore, we estimate that the lower bound enhancement factor of the P-NPG substrate is on the order of 10^7, which is one order of magnitude higher than that of the standard Klarite® commercial substrate.

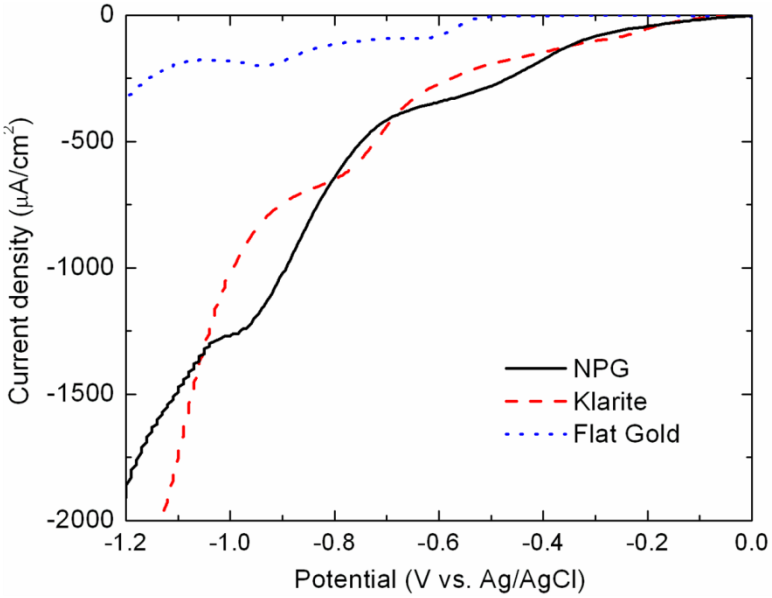

Figure 5-6 Voltammetric scans for the reductive desorption of benzenethiolate molecules from flat gold, Klarite®, and stamped NPG substrates. The scan rate was 200 mV/s. Desorption was performed in a pH 8.3 phosphate buffer (aq). (Adapted from Ref. [117])

5.4 Conclusions

In summary, we have used a simple one-step stamping technique, DIPS, to demonstrate the rapid, cost-effective nanofabrication of P-NPG SERS-active substrates. The P-NPG SERS templates exhibited efficient and reproducible SERS enhancement of at least 10^7. The well-organized 2D periodic NPG gratings and surrounding densified NPG film were both shown to contribute to the significantly enhanced SERS activity. At least one order of magnitude higher SERS intensity was observed based on our stamped 650 nm period, 60 nm deep grating structure compared to that of a commercial Klarite® substrate. Higher SERS intensity can be expected by properly tuning the period, depth, and shape of the gratings as discussed in CHAPTER 6.

CHAPTER 6.

CONTROLLING SERS USING GRATING-TYPE PATTERNED NANOPOROUS GOLD SUBSTRATES

6.1 Overview

In CHAPTER 5 we demonstrated 2D grating patterned NPG (P-NPG) films that, for the first time, utilized both LSP and SPP effects to dramatically enhance the already strong SERS intensity of as-prepared NPG.[117] In this chapter, we carefully study the contribution of the SPP effect on the strong SERS intensity measured from the grating-type P-NPG substrates. We theoretically and experimentally demonstrate that the SPP resonance and the resulting SERS response can be systematically controlled by tuning of the grating depth and duty cycle on a given NPG film. Activation of a strong SPP effect and its strong coupling with the LSP effect on P-NPG samples, with appropriate grating dimensions, gives rise to SERS enhancements up to 10^8, compared to non-enhancing substrates for benzenethiol molecules.

6.2 Materials and methods

6.2.1 Fabrication of NPG and P-NPG

The same NPG films (~100 nm) described in section 5.2 were fabricated and utilized for SERS measurments.[70, 117] 2D P-NPG SERS substrates with fixed grating period (Λ = 650 nm) and various grating duty cycles and imprint depths were fabricated via DIPS.[116] Note that 2D P-NPG substrates are polarization-symmetric at normal incidence, and therefore a SPP mode can be launched on the substrate surface with unpolarized light without any strict sample alignment.

6.2.2 SERS measurements

SERS measurements were performed with benzenethiol as described in sections 5.2.3. All P-NPG samples were immersed in 10 mM benzenethiol in ethanol solution for 1 hour to form a SAM of

benzenethiol, and the samples were subsequently rinsed with ethanol and dried with nitrogen. A standard 500 µm thick polydimethylsiloxane (PDMS) cell containing pure benzenethiol was also prepared as the control, non-enhancing substrate for the calculation of the enhancement factor (EF) of the SERS substrates.[107] SERS spectra were measured at normal incidence with a DXR Raman microscope (Thermo Scientific) utilizing a 780 nm diode laser at 0.9 mW power. A 10× magnification objective (NA = 0.25) was used to focus the laser beam and collect the SERS signal. The low magnification objective is preferred due to the larger laser illumination spot (~3.1 µm), which contains many periods of the P-NPG pattern and promotes high reproducibility and uniformity of the SERS measurements. Data was collected with an integration time of 10 s and averaging of 5 scans.

6.3 Results and discussion

6.3.1 P-NPG grating design parameters

A schematic of the P-NPG substrate with 2D gratings is shown in Figure 6-1 (a), where Λ is the grating period, h is the grating depth, and f is the duty cycle, which is defined as the ratio between grating ridge width and the grating period. In order to investigate the effect of tuning the grating parameters on the SERS response, 2D P-NPG samples with fixed grating period Λ = 650 nm, various duty cycles ranging from ~15% to 90%, and various grating heights ranging from ~20 to 70 nm were fabricated. The grating period of 650 nm was chosen based on prior studies (Figure 5-3 (a)) that demonstrated that this specific period most effectively excites a SPP on 2D P-NPG samples using excitation light near 780 nm.[117] Note that the grating period needs to be correspondingly tuned for other excitation wavelengths based on the dielectric constant of NPG.

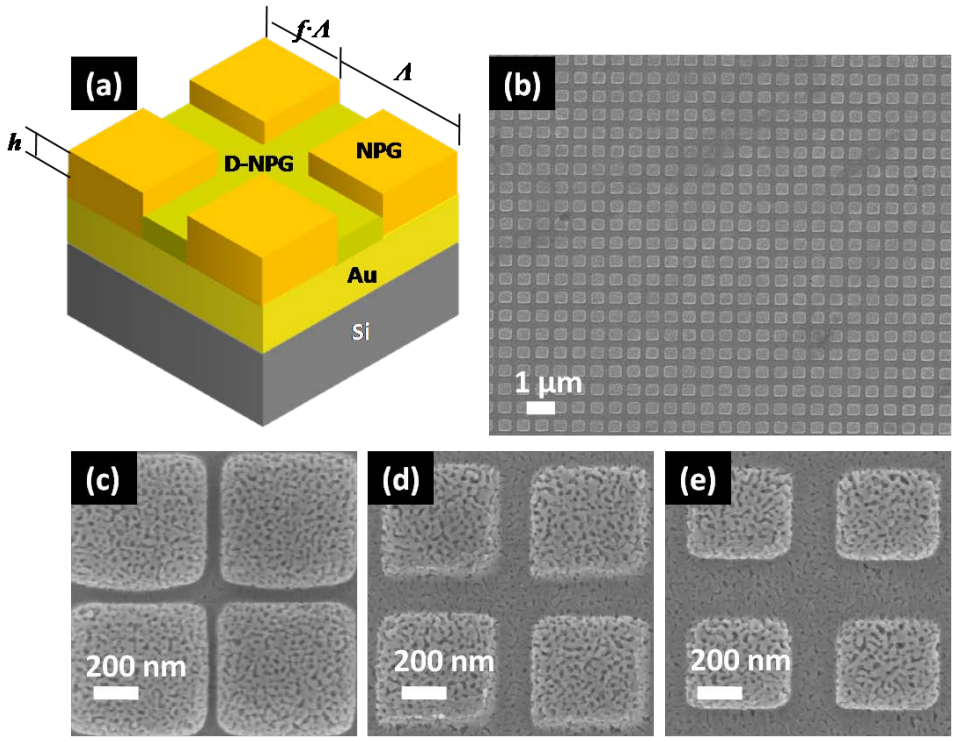

Figure 6-1 (a) Schematic configuration of 2D grating-type P-NPG substrates (*f*: duty cycle, *Λ*: period, *h*: depth). (b) Plan-view SEM image showing a large area P-NPG film with 650 nm period and ~60% duty cycle. (c) – (e) Zoomed-in plan-view SEM images of 650 nm period P-NPG films with decreasing duty cycles of ~90%, 75% and 60% respectively. (Adapted from Ref.[122])

Figure 6-1 (b) shows a representative top-view SEM image of a 2D P-NPG substrate with Λ = 650 nm and f = 60%, which reveals the uniformity of the P-NPG substrates over a large area. Figure 6-1 (c) – (e) show a series of zoomed-in SEM images of 2D P-NPG substrates with duty cycles of ~92%, 77% and 65%, respectively, revealing the surface morphology of both the densified-NPG (D-NPG) grating grooves and unstamped NPG grating ridges.

6.3.2 Role of plasmonic effects

6.3.2.1 Measurement of dielectric functions

In order to theoretically examine the presence of a SPP on the proposed 2D P-NPG structures at normal incidence, the material optical properties and grating geometry must be considered. Therefore, the dielectric constants (ε_r+$i\varepsilon_i$) of bulk Au, NPG, and D-NPG were first measured using a J.A. Woolam

M-2000 VI spectroscopic ellipsometer in a wavelength range of 400 – 900 nm. The measured complex dielectric constants of the bulk Au (black curve), NPG (red curve), and D-NPG (blue curve) film are shown in Figure 6-2 (a). Compared to bulk Au, the NPG and D-NPG are found to exhibit weaker metallic behavior, especially in the visible wavelength range where the real part of its dielectric constant is not sufficiently negative to support a SPP mode. A SPP mode requires that the real part of the dielectric constant of NPG must be negative with an absolute value exceeding that of air. Based on the measured dielectric constant of NPG, Maxwell-Garnett theory suggests a value of ~65% porosity for the NPG film; the measured dielectric constants of D-NPG suggest lower porosities and therefore stronger metallic behavior than NPG.

6.3.2.2 Numerical simulation

Using the measured dielectric constants of NPG and D-NPG films, we utilized rigorous coupled wave analysis (RCWA) to simulate the far field reflectance of P-NPG substrates with 1D grating lines (1D P-NPG) under TM polarized light at 780 nm, a simplified but representative structure for the polarization symmetric 2D P-NPG structure. As an example, simulated angle-interrogated reflectance curves from three 1D P-NPG substrates with fixed f = 60% duty cycle and different grating depths h = 20, 40, and 70 nm are shown in Figure 6-2 (b). Clear resonances located at near normal incidence were observed as marked with black arrows, which is strong evidence indicating SPP mode activation on each substrate. It is important that the SPP resonance is excited at or near normal incidence so that it can be efficiently activated via a standard Raman microscope. The microscope objective with NA = 0.25 utilized in this work provides a $\theta = 0 – 14.5°$ angular window for activating the SPP resonance and collecting the SERS signal, as marked with the dashed box in Figure 6-2 (b). It can be seen from Figure 6-2 (b) that the resonance depth decreases with decreasing grating height, implying reduced SPP activity and therefore reduced electromagnetic field intensity on the P-NPG surface.[95] We also note that the coupling resonance angle is slightly shifted for the different heights, which indicates a shifted wave vector of the activated SPP mode. These wave vector shifts can be explained as the change of the near field distribution of the activated SPP modes. For relatively shallow gratings, the SPP mode can be approximated as a

propagating wave existing on a continuous NPG surface, while for relatively deep gratings, the activated SPP modes in fact exist on top of the grating-modulated meta-surfaces. This series of SPP modes associated with relatively deep gratings are due to the localized Fabry-Perot resonances formed in consecutive vertical metallic cavities between neighboring grating ridges.[105, 123] Similar observations of SPP resonance shifts and different resonance depths with a change of grating height have also been reported in previous studies.[27, 124]

In order to analyze the influence of duty cycle on the SPP effect, we used the FDTD method to simulate the wavelength-interrogated absorbance for P-NPG samples with a fixed grating depth (70 nm) and various duty cycles (f = 30%, 60%, and 90%), as shown in Figure 6-2 (c). Note that the SPP resonance continuously red shifts with the increase of the duty cycle. For P-NPG samples with 30% (dashed curve) and 90% (dot dashed curve) duty cycle, SPP resonance peaks are located at ~700 and 1000 nm, respectively, which is not spectrally overlapped with the wavelength of excitation (780 nm) and most of the Raman bands of benzenethiol (800 – 900 nm). The 60% (solid curve) duty cycle sample results in a strong and broad SPP resonance occurring at 850 nm, which completely covers the wavelengths of excitation and all Raman bands of benzenethiol. The clear SPP resonance or wave vector shift with different grating duty cycles can be explained by the change of near field distributions on meta-surfaces with various duty cycles. The near field intensity of the P-NPG samples with different duty cycles was also simulated by using the FDTD method. The inset of Figure 6-2 (c) shows the corresponding near field intensities of the three samples at the Stokes wavelength of the 1070 cm^{-1} band (850 nm). It is clear that the 60% duty cycle sample leads to the strongest near field intensity over a large area molecule accessible surface, which is consistent with our observation from the far field absorbance spectra and proves that a SPP mode can be efficiently achieved when the grating parameters are designed appropriately. Hence for a particular wavelength of light, correct specification of the grating period, height, and duty cycle gives rise to efficient scattering and coupling of light to the SPP mode. Gratings with inappropriate dimensions will result in a significantly decreased scattering and therefore decreased coupling efficiency of a SPP mode.[124] The theoretical calculations shown in Figure 6-2 (b, c) show that both the grating depth and duty

cycle influence the resonance wavelength as well as the activation efficiency of the SPP mode, and are correspondingly expected to strongly influence the achievable SERS intensity. Reflectance spectra and near electric field intensity were also simulated for these and similar P-NPG structures for an excitation wavelength of 532 nm, another commonly used SERS laser wavelength known to promote LSP activation in NPG films; however, no resolvable resonance was observed, suggesting that the SPP effect could not be efficiently activated on our P-NPG substrates at this wavelength. As shown in Figure 6-2 (a), the real part of the dielectric constant of NPG is not sufficiently negative at 532nm to exhibit the strongly metallic behavior required to support efficient activation of a SPP at this wavelength.[47]

6.3.2.3 Experimental measurements of absorption spectra

In order to further elucidate the roles of the SPP and LSP effects in the SERS response of our P-NPG substrates, we experimentally measured the absorption spectra for NPG, D-NPG, and P-NPG films at normal incidence. In Figure 6-2 (d), broad absorption resonances with similar peak wavelengths near 510 nm are observed from all three films indicating the existence of the LSP effect due to the nanoscale porous structure of NPG, which is consistent with prior work.[21, 114] Since the broad LSP resonance ranging from 500 to 900 nm encompasses the excitation laser wavelength of 780 nm, the LSP effect contributes to the enhanced SERS response of NPG-based SERS substrates. Note that although both the D-NPG and P-NPG films show overall reduced absorption intensities due to the densification effect, the LSP condition and its coupling in the smaller densified pores leads to a larger SERS enhancement compared to as-prepared NPG films. Note that densification and pore size reduction enhances the peak near field intensity, which is not directly determined from this far field measurement. A second clear absorption resonance located at ~ 800 nm is only observed from the P-NPG sample (Λ = 650 nm, f = 70%, h = 70 nm), which indicates the activation of SPP mode that also contributes to the SERS enhancement of P-NPG substrates. The activated SPP subsequently introduces a stronger LSP effect via strong coupling between the two modes since the SPP resonance occurs within the broad range of the LSP resonance.[46] The width of SPP resonance is strongly dependent on the dielectric constant of NPG; NPG films with a

relatively small imaginary part and large negative real part of the dielectric function exhibit narrower and stronger SPP resonances.

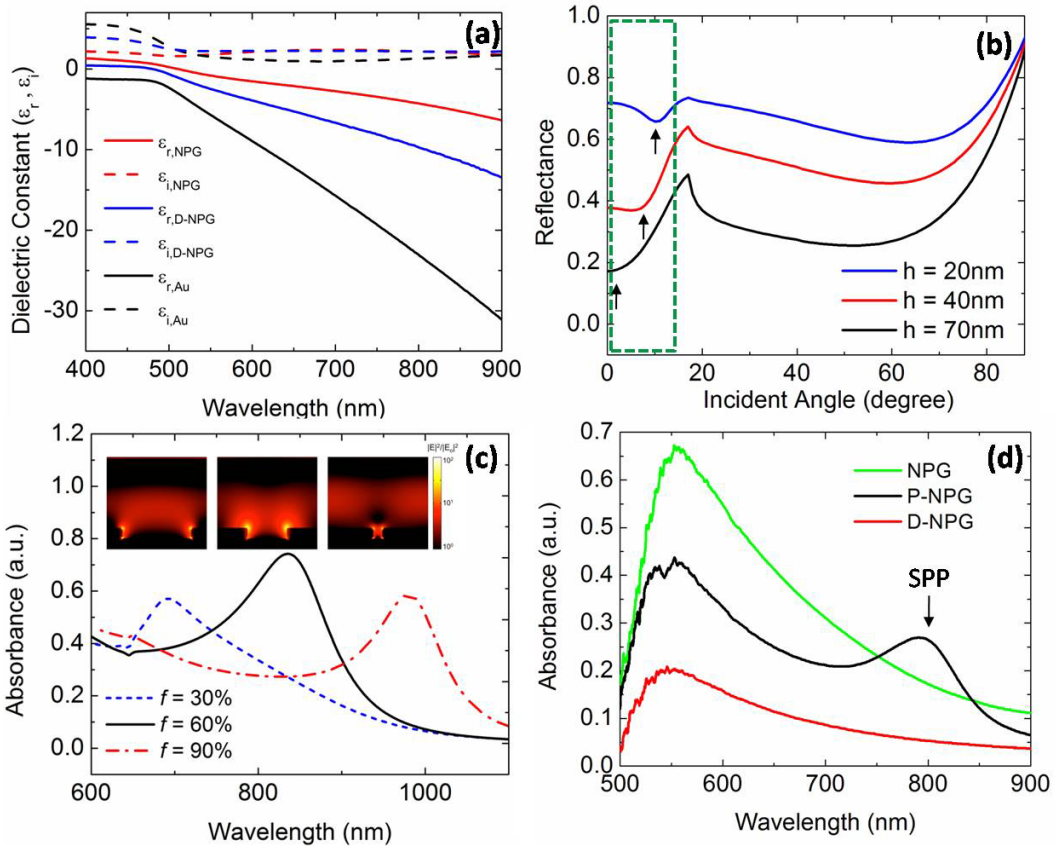

Figure 6-2 (a) Measured dielectric constants of Au (black curve), NPG (red curve), and D-NPG (blue curve) as a function of wavelength. (b) Simulated far field reflectance curves for 1D grating-type NPG substrates (Λ = 650 nm, f = 60%) with various grating depths (h = 20, 40, and 70 nm). Dashed box indicates the angular range of the 10× magnification, 0.25 NA, objective. Resonances indicate the presence of SPP. (c) Simulated far field absorbance and corresponding near field intensity $|E|^2/|E_0|^2$ (inset) within a whole grating period for 2D grating-type NPG substrates (Λ = 650 nm, h = 70 nm) with various duty cycles (f = 30%, 60%, and 90%). (d) Measured absorbance spectra of NPG, D-NPG, and P-NPG in UV-visible range. (Adapted from Ref.[122])

6.3.3 Controlling of SERS response

Based on the promising simulation studies demonstrating that the efficiency of activating a SPP mode and its resonance wavelength can be tuned via the control of various grating parameters, we next experimentally examined the influence of these grating parameters on SERS intensity by fabricating 2D P-NPG samples with varied parameters (duty cycle and grating depth) using the DIPS imprinting

technique.[116] With this fabrication method, the grating depth can be easily tuned by applying different pressures ranging from 75 N mm^{-2} to 300 N mm^{-2}, which results in a range of corresponding grating depths from approximately 20 to 75 nm (as determined by atomic force microscopy). The grating duty cycle is adjusted using different stamp designs. In all of the experiments, the grating period was fixed at 650 nm, as was the case for our simulation studies. Figure 6-3 (a – c) shows the experimentally measured relationship between SERS intensity, duty cycle, and grating depth at three standard Raman bands of benzenethiol (414, 1070, and 1570 cm^{-1}). Error bars were calculated based on 5 – 10 measurements on different spots across each sample. A clear variation in SERS intensity with duty cycle was observed from each respective Raman band. As explained previously, for a given grating period and grating height, there is an optimal duty cycle that leads to the most efficient activation of a SPP mode. For the relatively deep 70 nm gratings (black triangle), the SERS response is considerably increased with increasing duty cycle (or grating ridge width) within the range from ~15% to 67%. After reaching a maximum SERS intensity near 67%, for each of the three chosen Raman peaks, further increasing the duty cycle results in reduced SERS intensities. This observed phenomenon indicates not only a continuous red shift of the SPP resonance with increased grating duty cycle, as shown in Figure 6-3 (c), but also the importance of the resonance wavelength to the resulting SERS intensity. A color plot of SERS intensity for all Raman peaks as a function of duty cycle is shown in Figure 6-3 (e) for the 70 nm deep grating sample, which indicates that $f \sim 67\%$ is the optimal design across all measured Raman bands. Note that the SERS amplification is not very band selective as was the case for the PSi waveguide discussed in CHAPTER 4. Similar phenomenon showing an optimized duty cycle for a given grating depth has been predicted in previous study.[27] It also can be seen that decreased grating depth leads to a reduced maximum SERS intensity, which agrees well with our calculations shown in Figure 6-2 (b). Note that decreasing the grating height also shifts the optimum grating duty cycle towards larger values, which is required for shallow gratings to enable strong coupling of SPPs. For the 40 nm (red circle) and 20 nm (blue square) deep gratings, maximum SERS intensities were achieved at larger duty cycles of ~77% and 92%, respectively. The SERS spectra from benzenethiol on the 2D P-NPG samples with different grating depths and their

corresponding optimized duty cycles are shown in Figure 6-3 (d). The optimal grating design parameters for our NPG films are: Λ = 650 nm, f = 67%, h = 70 nm.

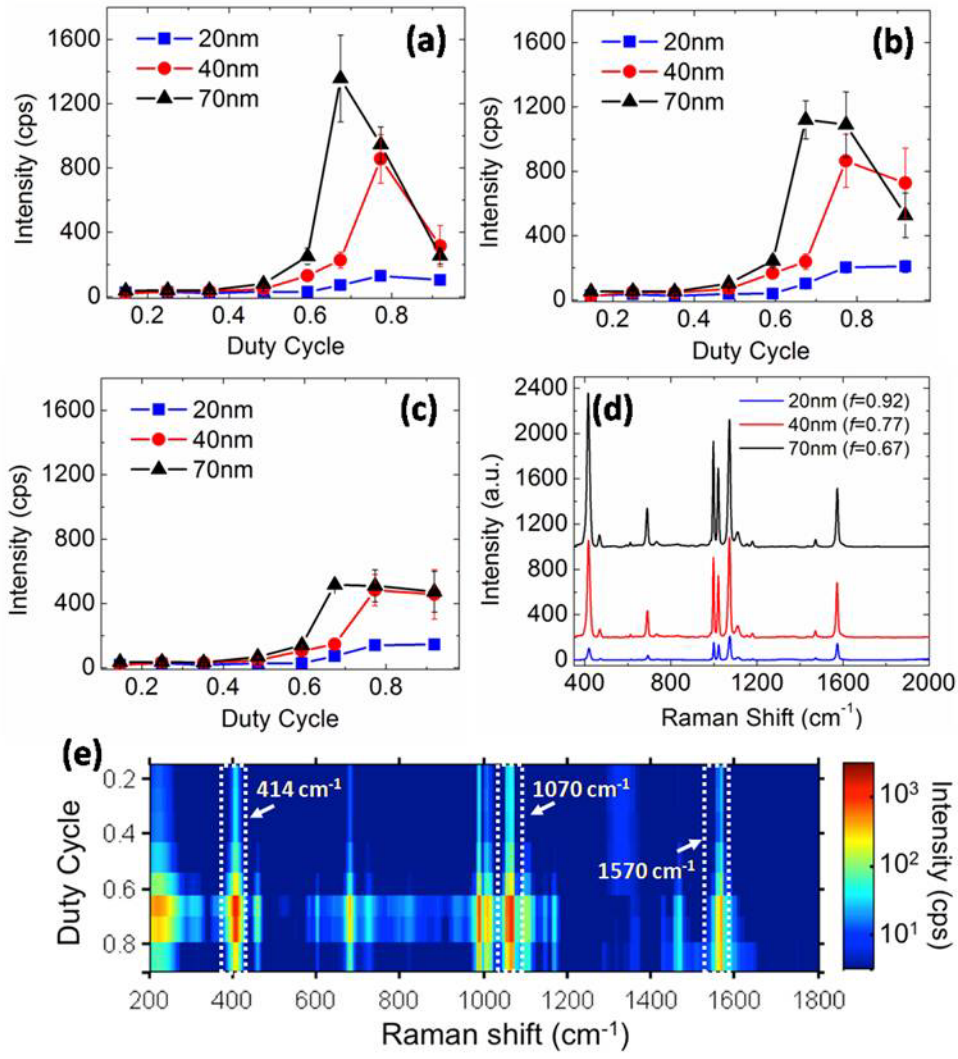

Figure 6-3 (a) - (c) Relationship between SERS intensity and duty cycle with respect to various grating depths for benzenethiol bands 414 cm^{-1}, 1070 cm^{-1}, and 1570 cm^{-1}, respectively. The chosen bands are indicated with arrows and dotted boxes. (d) Summary of SERS spectra of benzenethiol adsorbed on three optimized substrates with various grating depths. (e) SERS intensity distribution of benzenethiol adsorbed on 2D P-NPG substrates with various duty cycles ranging from ~15% to 90%. (Adapted from Ref.[122])

6.3.4 Enhancement factor calculation

In order to determine the SERS enhancement effect of the 2D P-NPG substrates, a reference sample of pure benzenethiol contained in a 500 μm thick PDMS cell was also measured with the same experimental setup.[107] Figure 6-4 shows the comparison of the SERS intensity from a 2D P-NPG substrate (Λ = 650

nm, h = 70 nm, f = 67%) and the reference sample. The enhancement factor (EF) of the optimized 2D P-NPG substrate was calculated using the following equation:[125]

$$EF = \frac{I_{2D\ P-NPG}}{I_{ref}} \frac{N_{ref}}{N_{2D\ P-NPG}} \tag{6.1}$$

where $I_{2DP\text{-}NPG}$ and I_{ref} are Raman intensities at 1070 cm^{-1} band measured from the 2D P-NPG substrate and the reference sample, respectively. $N_{2D\ P\text{-}NPG}$ and N_{ref} are the estimated number of molecules within a unit area of the 2D P-NPG substrate and the reference sample, respectively. Previously, in section 5.3.3, we found that the accessible surface area of 2D P-NPG (Λ = 650 nm, h = 60 nm, f = 50%) for benzenethiol is ~90% larger than that of planar gold,[117] and the estimated number of benzenethiol molecules per unit area on that 2D P-NPG substrate was 6.65×10^{14} cm^{-2}. Since the parameters of the 2D P-NPG substrates in our current work are very similar to those studied previously, we take $N_{2D\ P\text{-}NPG}$ to be 6.65×10^{14} for our current samples. N_{ref}, the number of probed molecules per unit area within the 500 μm thick cell, is estimated to be 2.94×10^{20} cm^{-2} based on $N_{ref} = N_A \rho d/M$, where N_A is Avogadro's number, ρ is the benzenethiol density, d is the thickness of the pure benzenethiol sample, and M is the molar mass of benzenethiol. From Figure 6-4, the measured intensity ratio ($I_{2DP\text{-}NPG}/I_{ref}$) at the 1070 cm^{-1} band is 275, and therefore the spatially averaged EF of the 2D P-NPG substrate with Λ = 650 nm, h = 70 nm, f = 67% is estimated to be 1.2×10^{8}.

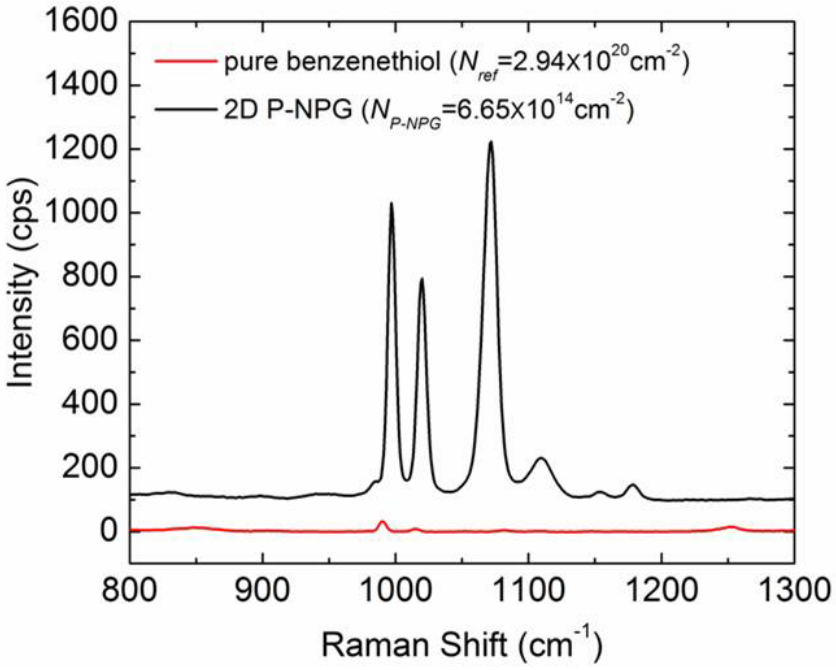

Figure 6-4 Comparison of SERS spectra between the optimized 2D P-NPG substrate (red curve) and a reference sample (500 μm thick pure benzenethiol in PDMS cell, black curve). 2D P-NPG shows an EF of ~1.2×10^{8}. (Adapted from Ref.[122])

6.4 Conclusions

In summary, 2D P-NPG substrates were utilized to demonstrate the influence of grating parameters on the SERS enhancement. The importance of a strongly activated SPP for achieving large SERS enhancement has been theoretically and experimentally demonstrated. By precisely and systematically tuning the gratings parameters, the SERS response of 2D P-NPG substrates was controlled and a SERS enhancement factor of 1.2×10^{8} was reported based on a 2D P-NPG substrate with appropriate grating period, duty cycle, and grating height. This enhancement factor is estimated to be approximately another order of magnitude improved over the initial P-NPG demonstration, where only grating period is varied. Unlike solely LSP based SERS substrates, 2D P-NPG is found to provide SERS enhancement relying on both the LSP and SPP of NPG with no requirement for using sophisticated lithography to achieve ultra-small lateral features or the need to search for a hot spot. Further refinement of the NPG morphology or the grating geometry, for example use of blazed grating design, may lead to additional increase of the EF.

The straightforward and low-cost of fabrication, large area uniformity, and high SERS enhancement factor make the 2D P-NPG substrate attractive as a high performance SERS substrate for chemical and biological molecule identification with high detection sensitivity.

CHAPTER 7.

CONCLUSIONS

7.1 Overview

In this work, label-free optical sensing structures based on porous silicon (PSi) and nanoporous gold (NPG) were investigated via design, theoretical calculation, numerical simulation, fabrication, and characterization. Combining nanoscale porous materials with appropriately designed optical structures enables high sensitivity detection of small molecules in terms of both molecular quantification via refractive index based sensing and molecular identification via the Raman scattering/surface enhanced Raman scattering (SERS) based sensing.

7.1.1 Refractive index based sensing

For refractive index based sensing, a prism-coupled polymer-cladded PSi membrane waveguide was theoretically and experimentally investigated in CHAPTER 2. Compared to a planar device, the increased available surface area for molecular attachment and enhanced mode overlap between the electric field and analyte enables the polymer-cladded PSi waveguide to perform small molecule detection with high sensitivity. Transfer matrix methods and perturbation theory were utilized for deriving an analytical expression for the sensitivity of small molecule detection in the porous waveguide. This formula quantitatively demonstrates how the choice of waveguide porosity and mode order directly impact detection sensitivity, which can also be applied to other dielectric porous materials based on layered structures. We found that if the thickness and porosity of a waveguide layer are properly chosen, very high detection sensitivity can be achieved at a resonant angle approaching 90°. We also found that for a given mode order, decreasing the porosity of the PSi waveguide layer leads to an increased resonant angle, which monotonically increases the small molecule detection sensitivity. Experimental

measurements for detecting 3-APTES and 16-mer PNA molecules in PSi waveguides with different porosities verified the porosity and mode order-dependent sensitivity trends predicted by our theory.

In order to achieve a sufficient molecular infiltration into nanoscale pores to perform sensing, the optimized ratio between pore opening size and molecule size was also studied experimentally with the polymer-cladded PSi membrane waveguide structure. PSi waveguides with controllable pore diameters between 15 and 60 nm were exposed to nucleic acids of length between approximately 1.76 and 5.28 nm. We found that incremental increases in pore diameter allow for selectivity toward target molecules of a particular length (or size). The appropriate choice of pore size will allow the infiltration of specific sized molecules of interest while excluding larger contaminant molecules. Therefore, high sensitivity detection of a particular sized molecule not only relies on optical design parameters (i.e., mode order, porosity, and thickness of waveguide layer), but also the nanoscale geometry and chemistry (i.e., pore dimensions relative to target analyte dimensions).

7.1.2 Dual mode sensing

In CHAPTER 3, a dual mode sensing platform was demonstrated as a proof-of-concept study based on small (~4.5 nm) gold nanoparticles (Au NPs) coated on a single layer PSi interferometer. Measurements of the reflectance fringe pattern and SERS spectrum enabled both molecular quantification and identification within a single sensing substrate, respectively. A detection sensitivity of ~400 nm/RIU was reported based on reflectance measurements following benzenethiol adsorption. In addition, clear SERS signals of benzenethiol were observed from the Au NPs coated porous surface due to the strong localized surface plasmon (LSP) effect activated on closely packed Au NPs. In this study, PSi not only provided a large surface area for the molecule immobilization to improve the detection sensitivity, but also acts as a template for the Au NPs deposition and aggregation to enhance the SERS signal.

7.1.3 SERS based sensing

Two effective SERS substrates, a Au NPs coated PSi waveguide and a patterned nanoporous gold (P-NPG) substrate were studied and developed in CHAPTER 4, CHAPTER 5, and CHAPTER 6. Compared to the Au NPs coated single layer PSi discussed in CHAPTER 3, where the SERS signal only relies on the LSP effect, both Au NPs coated PSi waveguide and P-NPG SERS substrates utilize a guided wave to further enhance the SERS signal.

In CHAPTER 4, a grating-coupled two-layer PSi waveguide structure was fabricated underneath the Au NPs layer in order to provide a waveguide mode to further increase the LSP enhanced SERS signal. At the resonance condition of the waveguide, an additional 10-15 times SERS enhancement was achieved, compared to the single layer Au NPs coated PSi structure. The waveguide structure provides an effective method to enhance the SERS signal in a large area without rigorous requirements for precisely defined nanostructures on top of the structure, which would require small lateral patterned features (e.g. < 10 nm).

In CHAPTER 5 and CHAPTER 6, an effective SERS substrate based on NPG film was studied. NPG is a cost-effective metamaterial (3 cents/cm^2) consisting of a unique 3D sponge-like porous structure, which itself has been demonstrated as an effective SERS substrate since its nanoscale pores support a strong LSP effect over a broad visible wavelength range. In our P-NPG substrate, a straightforward direct imprinting technique developed specifically for porous materials, 'direct imprinting of porous substrates' (DIPS), was utilized to transfer 2D periodic gratings into the top part of a NPG film. Therefore, a surface plasmon polariton (SPP) mode, a propagating plasmonic effect, can be launched on the surface of NPG via periodic gratings in addition to the LSP mode. Both SPP and LSP effects were simultaneous excited to enhance the SERS signal. By appropriately choosing the grating period, duty cycle and height of the grating, the coupling strength and resonance wavelength of the SPP mode can be precisely controlled. Hence, a strong SERS signal for benzenethiol detection, with enhancement factor of ~1.2×10^8, was achieved with optimal grating parameters, which shows ~1000 times enhancement

compared to the as-prepared NPG film. This significant SERS enhancement can be attributed to the simultaneous excitation of SPP and LSP modes on the NPG.

7.2 Future work

This work represents a significant contribution to improve the sensing performances of label free optical sensors via the understanding of porous material properties and optimization of layered structures. Importantly, this work also provides guidelines of using engineering methods to systematically study the layered structures for sensing applications in terms of material choice and structure design. Therefore, more sensing applications based on PSi and NPG with further improved sensing performances (e.g. higher sensitivity, compatibility, design flexibility) can be expected in the future work.

7.2.1 Bloch surface wave (BSW) based sensing

Bloch surface waves (BSWs), propagating and vertically confined surface waves existing on dielectric materials can also be utilized in both refractive based sensing and SERS based sensing. Similar to the waveguide mode, the BSW is an electromagnetic wave guided in a very thin layer on the top surface of a multilayer structure with a semi-infinite periodic multilayer dielectric medium (i.e., 1D photonic crystal structure). Therefore, BSW modes are generated due to the photonic bandgap and total internal reflection from the cladding. As a surface wave existing in a dielectric medium, BSW modes are treated as dielectric analogues of the SPP mode, but they do not suffer from the large absorption loss of the metals. Therefore, narrower resonances in far field reflection or transmission can be expected from BSW structures with appropriate structure design, which can be utilized to improve the resolution of the refractive index based sensing. In addition to the narrower far field resonance, stronger near-field intensities of the confined electromagnetic field due to the activation of a BSW mode can also be utilized to enhance the SERS intensity. Figure 7-1 shows a schematic of a 1D grating-coupled Au-coated PSi BSW structure for the SERS application. Compared to the PSi waveguide SERS structure described in CHAPTER 4, a periodic multilayer layer structure (with alternating layer thicknesses of *a* and *b*) is used

for the BSW activation. With appropriate tunings of multilayer structure, a significantly enhanced near field due to the BSW mode can be expected on the top surface (with thickness of *d*) to enhance the SERS signal.

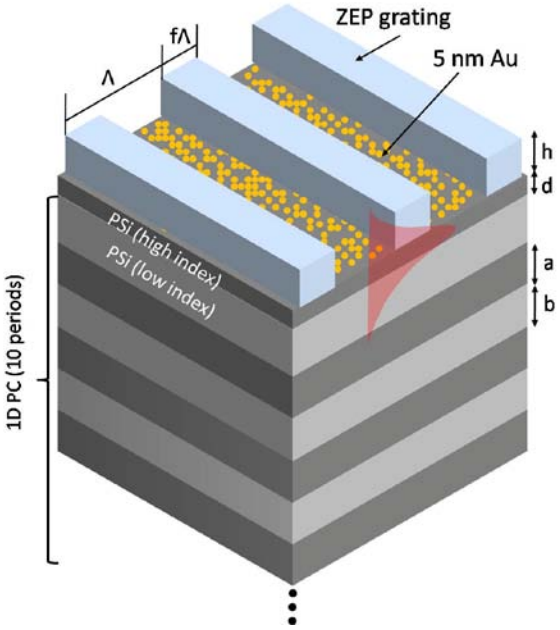

Figure 7-1 Schematic configuration of a 1D grating-coupled Au-coated PSi Bloch surface wave (BSW) structure

7.2.2 NPG based SERS substrates for liquid based detection

In some cases SERS measurements are required to be performed in liquid environments in order to enable fast sensing or avoid the non-uniformity of molecular distributions due to the potential coffee ring effects where higher concentrations of particles or molecules tend to deposit at the outer edge of a liquid spot when it dries. In liquid based SERS detection on NPG films, the nanoscale pores are completely filled with high refractive index liquid, such as water or ethanol (with refractive index of 1.33 or 1.36, respectively). Therefore, the dielectric constant of the NPG film will be correspondingly increased, which results in a less negative or even positive real part of the dielectric constant within the visible-NIR wavelength regions. As discussed in CHAPTER 6, at an excitation wavelength of 780 nm, the dielectric constant of NPG in air (black curve) satisfies the prerequisite of a SPP mode since the real part of

dielectric constant (r_{NPG}) at this wavelength is sufficiently negative and its absolute value exceeds the imaginary part of its dielectric constant, i.e., $|r_{NPG}|>i_{NPG}$ as shown in Figure 7-2. However, if the NPG film (65% porosity) is immersed in ethanol, its dielectric constant curve (red curve) will be shifted to longer wavelength compared to the case for NPG in air so that the real part of the dielectric constant of NPG in ethanol ($r_{NPG+Ethanol}$) in the 400 – 900 nm wavelength range is no longer sufficiently negative to support a SPP mode, i.e., $|r_{NPG+Ethanol}|<i_{NPG+Ethanol}$. However, we also note that in Figure 7-2 when the wavelength reaches ~1 μm and above, the real part of dielectric constant of NPG in ethanol ($r_{NPG+Ethanol}$) becomes comparably negative as to that of NPG in air at 780 nm. Therefore, in order to excite SPP modes on our current NPG films immersed in liquid environment, longer wavelength laser excitation is required, which may also necessitate the use of a more costly detector as the bandgap of silicon is approached. Alternatively, a more metallic-like NPG film with lower porosity and larger negative dielectric constant could be synthesized using a two metal co-deposition approach with higher gold content so that the resulting NPG in liquid can still perform as a metallic material to support the SPP modes.

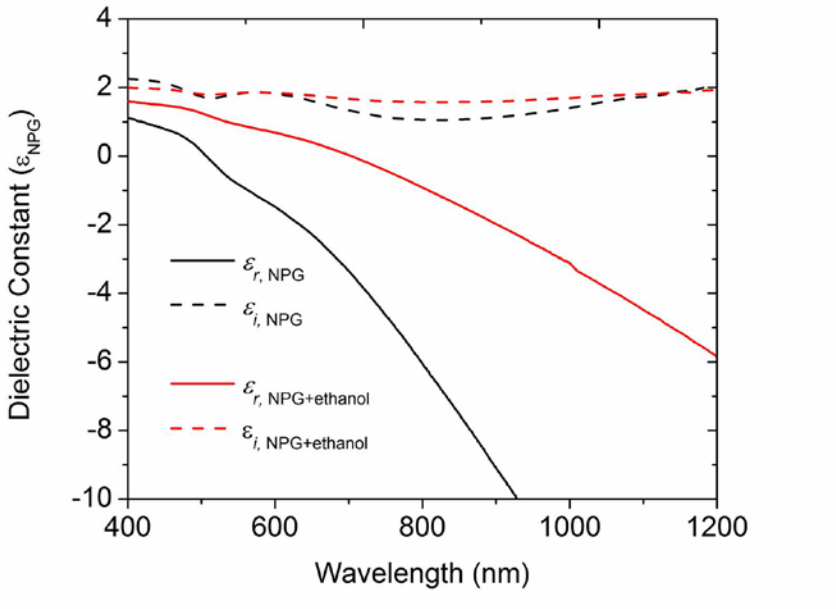

Figure 7-2 Measured dielectric constant of NPG in air (black curve) and calculated dielectric constant of NPG in ethanol (red curve) as a function of wavelength by assuming NPG has a porosity of 65%.

7.2.3 Enhancement of the LSP effect in NPG films

In CHAPTER 5 and CHAPTER 6, we fully examined the enhanced SERS arising primarily from a dominant SPP enhancement on the given NPG film. Further SERS enhancement can be expected by increasing the contribution of the LSP effect to the SERS response. Preliminary results (Figure 7-3) show that our as-prepared (unpatterned) NPG film infiltrated with ~4.5 nm Au NPs inside the pores (NPG + Au) results in a ~10 times higher SERS signal than that from as-prepared NPG. This phenomenon can be explained as the increased surface roughness and reduced pore size due to the infiltration of Au NPs. This result shows good agreement with previous work reporting that NPG films with larger gold ligaments and smaller pores lead to a stronger LSP effect.[21, 22]

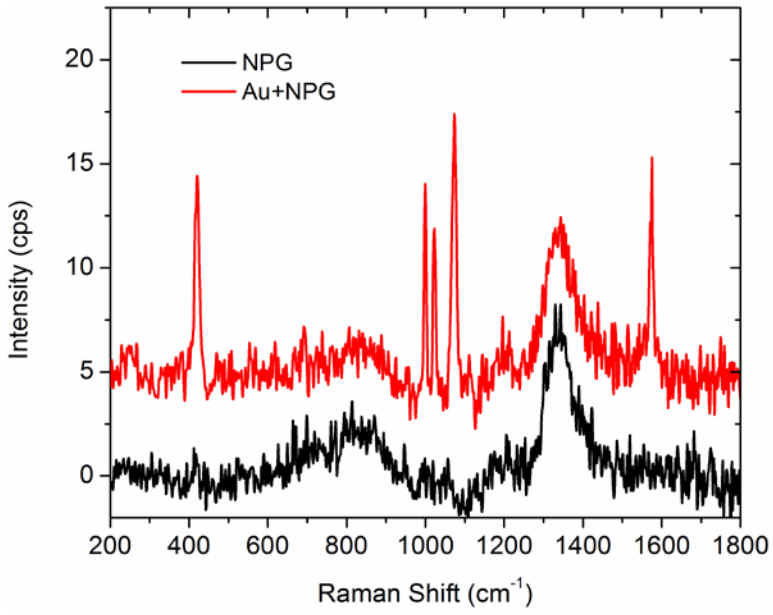

Figure 7-3 SERS signal comparison between NPG film and Au NPs coated NPG film

7.2.4 Microfluidic integration of P-NPG substrate as an SPR sensor

The same P-NPG SERS substrate described in CHAPTER 5 and CHAPTER 6 can also be utilized as a conventional grating-coupled SPR sensor.[47] Similar to the PSi waveguide structure described in CHAPTER 2, NPG also provides a large surface area for small molecule binding. Further, the activated SPP mode has a relatively long evanescent tail of electromagnetic field that can interact with large molecules that cannot infiltrate inside the pores. The far field reflection, transmission or absorption can be utilized as the optical sensing signal to indicate the presence of molecules on the surface. In order to improve the sensing resolution, the grating structure needs to be optimized. In this case, shallow gratings may be preferable due to the improved detection limit. Compared to the prism-coupling method, an imprinted grating coupler on the top surface of the NPG film enables direct light coupling without obstructing the top surface, allowing the integration of a microfluidic flow cell for real time liquid based sensing.

REFERENCES

1. Vo-Dinh, T.; Cullum, B., Biosensors and biochips: advances in biological and medical diagnostics. *Fresenius Journal of Analytical Chemistry* **2000,** *366* (6-7), 540-551.

2. Moerner, W. E., New directions in single-molecule imaging and analysis. *Proceedings of the National Academy of Sciences of the United States of America* **2007,** *104* (31), 12596-12602.

3. Brecht, A.; Gauglitz, G., Optical probes and transducers. *Biosensors & Bioelectronics* **1995,** *10* (9-10), 923-936.

4. Jiao, Y.; Weiss, S. M., Design parameters and sensitivity analysis of polymer-cladded porous silicon waveguides for small molecule detection. *Biosensors & Bioelectronics* **2010,** *25* (6), 1535-1538.

5. Moskovits, M., Surface-enhanced Raman spectroscopy: a brief perspective. *Surface-Enhanced Raman Scattering: Physics and Applications* **2006,** *103*, 1-17.

6. Sun, M. T.; Xia, L. X.; Chen, M. D., Self-assembled dynamics of silver nanoparticles and self-assembled dynamics of 1,4-benzenedithiol adsorbed on silver nanoparticles: Surface-enhanced Raman scattering study. *Spectrochimica Acta Part a-Molecular and Biomolecular Spectroscopy* **2009,** *74* (2), 509-514.

7. Choi, C. J.; Xu, Z.; Wu, H. Y.; Liu, G. L.; Cunningham, B. T., Surface-enhanced Raman nanodomes. *Nanotechnology* **2010,** *21* (*14*), 415301.

8. Michaels, A. M.; Nirmal, M.; Brus, L. E., Surface enhanced Raman spectroscopy of individual rhodamine 6G molecules on large Ag nanocrystals. *Journal of the American Chemical Society* **1999,** *121* (43), 9932-9939.

9. Campion, A.; Kambhampati, P., Surface-enhanced Raman scattering. *Chemical Society Reviews* **1998,** *27* (4), 241-250.

10. Kneipp, K.; Wang, Y.; Kneipp, H.; Perelman, L. T.; Itzkan, I.; Dasari, R.; Feld, M. S., Single molecule detection using surface-enhanced Raman scattering (SERS). *Physical Review Letters* **1997,** *78* (9), 1667-1670.

11. Xu, H. X.; Bjerneld, E. J.; Kall, M.; Borjesson, L., Spectroscopy of single hemoglobin molecules by surface enhanced Raman scattering. *Physical Review Letters* **1999,** *83* (21), 4357-4360.

12. Williamson, T. L.; Guo, X. Y.; Zukoski, A.; Sood, A.; Diaz, D. J.; Bohn, P. W., Porous GaN as a template to produce surface-enhanced Raman scattering-active surfaces. *Journal of Physical Chemistry B* **2005,** *109* (43), 20186-20191.

13. Chan, S.; Kwon, S.; Koo, T. W.; Lee, L. P.; Berlin, A. A., Surface-enhanced Raman scattering of small molecules from silver-coated silicon nanopores. *Advanced Materials* **2003,** *15* (19), 1595-1598.

14. Fleischmann, M.; Hendra, P. J.; McQuillan, A. J., Raman spectra of pyridine adsorbed at a silver electrode. *Chemical Physics Letters* **1974,** *26* (2), 163-166.

15. Freeman, R. G.; Grabar, K. C.; Allison, K. J.; Bright, R. M.; Davis, J. A.; Guthrie, A. P.; Hommer, M. B.; Jackson, M. A.; Smith, P. C.; Walter, D. G.; Natan, M. J., Self-assembled metal colloid monolayers - an approach to sers substrates. *Science* **1995,** *267* (5204), 1629-1632.

16. Zhang, X. Y.; Young, M. A.; Lyandres, O.; Van Duyne, R. P., Rapid detection of an anthrax biomarker by surface-enhanced Raman spectroscopy. *Journal of the American Chemical Society* **2005,** *127* (12), 4484-4489.

17. Jackson, J. B.; Halas, N. J., Surface-enhanced Raman scattering on tunable plasmonic nanoparticle substrates. *Proceedings of the National Academy of Sciences of the United States of America* **2004,** *101*(*52*), 17930-17935.

18. Lu, Y.; Liu, G. L.; Lee, L. P., High-density silver nanoparticle film with temperature-controllable interparticle spacing for a tunable surface enhanced Raman scattering substrate. *Nano Letters* **2005,** *5* (1), 5-9.

19. Tao, A.; Kim, F.; Hess, C.; Goldberger, J.; He, R. R.; Sun, Y. G.; Xia, Y. N.; Yang, P. D., Langmuir-Blodgett silver nanowire monolayers for molecular sensing using surface-enhanced Raman spectroscopy. *Nano Letters* **2003,** *3* (9), 1229-1233.

20. Kucheyev, S. O.; Hayes, J. R.; Biener, J.; Huser, T.; Talley, C. E.; Hamza, A. V., Surface-enhanced Raman scattering on nanoporous Au. *Applied Physics Letters* **2006,** *89* (5), 053102.

21. Lang, X. Y.; Chen, L. Y.; Guan, P. F.; Fujita, T.; Chen, M. W., Geometric effect on surface enhanced Raman scattering of nanoporous gold: Improving Raman scattering by tailoring ligament and nanopore ratios. *Applied Physics Letters* **2009,** *94* (21), 213109.

22. Qian, L. H.; Yan, X. Q.; Fujita, T.; Inoue, A.; Chen, M. W., Surface enhanced Raman scattering of nanoporous gold: Smaller pore sizes stronger enhancements. *Applied Physics Letters* **2007,** *90* (15), 153120.

23. Zhang, L.; Lang, X.; Hirata, A.; Chen, M., Wrinkled Nanoporous Gold Films with Ultrahigh SERS Enhancement. *ACS nano* **2011,** 5(6), 4407-4413.

24. Kahl, M.; Voges, E.; Kostrewa, S.; Viets, C.; Hill, W., Periodically structured metallic substrates for SERS. *Sensors and Actuators B-Chemical* **1998,** *51* (1-3), 285-291.

25. Oran, J. M.; Hinde, R. J.; Abu Hatab, N.; Retterer, S. T.; Sepaniak, M. J., Nanofabricated periodic arrays of silver elliptical discs as SERS substrates. *Journal of Raman Spectroscopy* **2008,** *39* (12), 1811-1820.

26. Zhang, X. Y.; Yonzon, C. R.; Van Duyne, R. P., Nanosphere lithography fabricated plasmonic materials and their applications. *Journal of Materials Research* **2006,** *21* (5), 1083-1092.

27. Kahl, M.; Voges, E., Analysis of plasmon resonance and surface-enhanced Raman scattering on periodic silver structures. *Physical Review B* **2000,** *61* (20), 14078-14088.

28. Ayas, S.; Guner, H.; Turker, B.; Ekiz, O. O.; Dirisaglik, F.; Okyay, A. K.; Dana, A., Raman Enhancement on a Broadband Meta-Surface. *ACS Nano* **2012,** *6* (8), 6852-6861.

29. Im, H.; Bantz, K. C.; Lindquist, N. C.; Haynes, C. L.; Oh, S. H., Vertically Oriented Sub-10-nm Plasmonic Nanogap Arrays. *Nano Letters* **2010,** *10* (6), 2231-2236.

30. Hatab, N. A.; Hsueh, C. H.; Gaddis, A. L.; Retterer, S. T.; Li, J. H.; Eres, G.; Zhang, Z. Y.; Gu, B. H., Free-Standing Optical Gold Bowtie Nanoantenna With Variable Gap Size For Enhanced Raman Spectroscopy. *Nano Letters* **2010,** *10* (12), 4952-4955.

31. Hsueh, C.-H.; Lin, C.-H.; Li, J.-H.; Hatab, N. A.; Gu, B., Resonance modes, cavity field enhancements, and long-range collective photonic effects in periodic bowtie nanostructures. Optics Express **2011**, *19* (20), 19660-19667.

32. Lesuffleur, A.; Kumar, L. K. S.; Brolo, A. G.; Kavanagh, K. L.; Gordon, R., Apex-enhanced Raman spectroscopy using double-hole arrays in a gold film. *Journal of Physical Chemistry C* **2007,** *111* (6), 2347-2350.

33. Hou, Y.; Xu, J.; Zhang, X.; Yu, D., SERS on periodic arrays of coupled quadrate-holes and squares. *Nanotechnology 21*, 195203.

34. Pacholski, C.; Sartor, M.; Sailor, M. J.; Cunin, F.; Miskelly, G. M., Biosensing using porous silicon double-layer interferometers: Reflective interferometric Fourier transform spectroscopy. *Journal of the American Chemical Society* **2005,** *127* (33), 11636-11645.

35. Strehlke, S.; Bastide, S.; Guillet, J.; Levy-Clement, C., Design of porous silicon antireflection coatings for silicon solar cells. *Materials Science and Engineering B-Solid State Materials for Advanced Technology* **2000,** *69* (*14*), 81-86.

36. Ilyas, S.; Bocking, T.; Kilian, K.; Reece, P. J.; Gooding, J.; Gaus, K.; Gal, M., Porous silicon based narrow line-width rugate filters. *Optical Materials* **2007,** *29* (6), 619-622.

37. Weiss, S. M.; Fauchet, P. M., Porous silicon one-dimensional photonic crystals for optical signal modulation. *IEEE Journal of Selected Topics in Quantum Electronics* **2006,** *12* (6), 1514-1519.

38. Zhang, Z.; Lu, D. F.; Qi, Z. M., Application of Porous TiO2 Thin Films as Wavelength-Interrogated Waveguide Resonance Sensors for Bio/Chemical Detection. *Journal of Physical Chemistry C* **2012,** *116* (5), 3342-3348.

39. Rong, G.; Weiss, S. M., Biomolecule size-dependent sensitivity of porous silicon sensors. *Physica Status Solidi a-Applications and Materials Science* **2009,** *206* (6), 1365-1368.

40. Lau, K. H. A.; Tan, L. S.; Tamada, K.; Sander, M. S.; Knoll, W., Highly sensitive detection of processes occurring inside nanoporous anodic alumina templates: A waveguide optical study. *Journal of Physical Chemistry B* **2004,** *108* (30), 10812-10818.

41. Amato, G.; Boarino, L.; Borini, S.; Rossi, A. M., Hybrid approach to porous silicon integrated waveguides. *Physica Status Solidi a-Applied Research* **2000,** *182* (1), 425-430.

42. Saarinen, J. J.; Weiss, S. M.; Fauchet, P. M.; Sipe, J. E., Optical sensor based on resonant porous silicon structures. *Optics Express* **2005,** *13* (10), 3754-3764.

43. Yamaguchi, A.; Hotta, K.; Teramae, N., Optical Waveguide Sensor Based on a Porous Anodic Alumina/Aluminum Multilayer Film. *Analytical Chemistry* **2009,** *81* (1), 105-111.

44. Densmore, A.; Xu, D. X.; Waldron, P.; Janz, S.; Cheben, P.; Lapointe, J.; Delage, A.; Lamontagne, B.; Schmid, J. H.; Post, E., A silicon-on-insulator photonic wire based evanescent field sensor. *IEEE Photonics Technology Letters* **2006,** *18* (21-24), 2520-2522.

45. Liedberg, B.; Nylander, C.; Lunstrom, I., Surface plasmon resonance for gas detection and biosensing. *Sensors and Actuators* **1983,** *4*, 299-304.

46. Yu, F.; Ahl, S.; Caminade, A. M.; Majoral, J. P.; Knoll, W.; Erlebacher, J., Simultaneous excitation of propagating and localized surface plasmon resonance in nanoporous gold membranes. *Analytical Chemistry* **2006,** *78* (20), 7346-7350.

47. Ruffato, G.; Romanato, F.; Garoli, D.; Cattarin, S., Nanoporous gold plasmonic structures for sensing applications. *Optics Express* **2011,** *19* (14), 13164-13170.

48. Homola, J., Present and future of surface plasmon resonance biosensors. *Analytical and bioanalytical chemistry* **2003,** *377* (3), 528-539.

49. Yeh, P., *Optical waves in layered media*. Wiley New York: 1988.

50. Moharam, M. G.; Gaylord, T. K., Diffraction analysis of dielectric surface-relief gratings. *J. Opt. Soc. Am.* **1982,** *72* (10), 1385-1392.

51. Moharam, M. G.; Gaylord, T. K., Rigorous coupled-wave analysis of metallic surface-relief gratings. *J. Opt. Soc. Am. A* **1986,** *3* (11), 1780-1787.

52. Kane, Y., Numerical solution of initial boundary value problems involving maxwell's equations in isotropic media. *Antennas and Propagation, IEEE Transactions on* **1966,** *14* (3), 302-307.

53. Rong, G.; Najmaie, A.; Sipe, J. E.; Weiss, S. M., Nanoscale porous silicon waveguide for label-free DNA sensing. *Biosensors & Bioelectronics* **2008,** *23* (10), 1572-1576.

54. Rong, G. G.; Ryckman, J. D.; Mernaugh, R. L.; Weiss, S. M., Label-free porous silicon membrane waveguide for DNA sensing. *Applied Physics Letters* **2008,** *93* (16), 161109.

55. Qi, Z. M.; Honma, I.; Zhou, H. S., Nanoporous leaky waveguide based chemical and biological sensors with broadband spectroscopy. *Applied Physics Letters* **2007,** *90* (1), 011102.

56. Lin, V. S. Y.; Motesharei, K.; Dancil, K. P. S.; Sailor, M. J.; Ghadiri, M. R., A porous silicon-based optical interferometric biosensor. *Science* **1997,** *278* (5339), 840-843.

57. Chan, S.; Horner, S. R.; Fauchet, P. M.; Miller, B. L., Identification of gram negative bacteria using nanoscale silicon microcavities. *Journal of the American Chemical Society* **2001,** *123* (47), 11797-11798.

58. Talian, I.; Mogensen, K. B.; Orinak, A.; Kaniansky, D.; Hubner, J., Surface-enhanced Raman spectroscopy on novel black silicon-based nanostructured surfaces. *Journal of Raman Spectroscopy* **2009,** *40* (8), 982-986.

59. Canpean, V.; Astilean, S., Multifunctional plasmonic sensors on low-cost subwavelength metallic nanoholes arrays. *Lab on a Chip* **2009,** *9* (24), 3574-3579.

60. Ko, H.; Chang, S.; Tsukruk, V. V., Porous Substrates for Label-Free Molecular Level Detection of Nonresonant Organic Molecules. *ACS Nano* **2009,** *3* (1), 181-188.

61. Awazu, K.; Rockstuhl, C.; Fujimaki, M.; Fukuda, N.; Tominaga, J.; Komatsubara, T.; Ikeda, T.; Ohki, Y., High sensitivity sensors made of perforated waveguides. *Optics Express* **2007,** *15* (5), 2592-2597.

62. Richter, A.; Steiner, P.; Kozlowski, F.; Lang, W., Current-induced light-emission from a porous silicon device. *IEEE Electron Device Letters* **1991,** *12* (12), 691-692.

63. Weiss, S. M.; Ouyang, H. M.; Zhang, J. D.; Fauchet, P. M., Electrical and thermal modulation of silicon photonic bandgap microcavities containing liquid crystals. *Optics Express* **2005,** *13* (4), 1090-1097.

64. Zheng, J. P.; Jiao, K. L.; Shen, W. P.; Anderson, W. A.; Kwok, H. S., Highly sensitive photodetector using porous silicon. *Applied Physics Letters* **1992,** *61* (4), 459-461.

65. Lehmann, V., *Electrochemistry of silicon*. Wiley Online Library: 2002.

66. Ouyang, H.; Christophersen, M.; Viard, R.; Miller, B. L.; Fauchet, P. M., Macroporous silicon microcavities for macromolecule detection. *Advanced Functional Materials* **2005,** *15* (11), 1851-1859.

67. Beale, M. I. J.; Chew, N. G.; Uren, M. J.; Cullis, A. G.; Benjamin, J. D., Microstructure and formation mechanism of porous silicon. *Applied Physics Letters* **1985,** *46* (1), 86-88.

68. Lehmann, V.; Gosele, U., Porous silicon formation - a quantum wire effect. *Applied Physics Letters* **1991,** *58* (8), 856-858.

69. Smith, R. L.; Collins, S. D., Porous silicon formation mechanisms. *Journal of Applied Physics* **1992,** *71* (8), R1-R22.

70. Ciesielski, P. N.; Scott, A. M.; Faulkner, C. J.; Berron, B. J.; Cliffel, D. E.; Jennings, G. K., Functionalized Nanoporous Gold Leaf Electrode Films for the Immobilization of Photosystem I. *ACS Nano* **2008,** *2* (12), 2465-2472.

71. Lang, X.; Hirata, A.; Fujita, T.; Chen, M., Nanoporous metal/oxide hybrid electrodes for electrochemical supercapacitors. *Nature Nanotechnology* **2011,** *6* (4).232-236.

72. Qian, L. H.; Inoue, A.; Chen, M. W., Large surface enhanced Raman scattering enhancements from fracture surfaces of nanoporous gold. *Applied Physics Letters* **2008,** *92* (9), 093113.

73. Zhang, L.; Lang, X. Y.; Hirata, A.; Chen, M. W., Wrinkled Nanoporous Gold Films with Ultrahigh Surface-Enhanced Raman Scattering Enhancement. *ACS Nano* **2011,** *5* (6), 4407-4413.

74. Yu, F.; Yao, D. F.; Knoll, W., Surface plasmon field-enhanced fluorescence spectroscopy studies of the interaction between an antibody and its surface-coupled antigen. *Analytical Chemistry* **2003,** *75* (11), 2610-2617.

75. Vallet-Regi, M. A.; Ruiz-Gonzalez, L.; Izquierdo-Barba, I.; Gonzalez-Calbet, J. M., Revisiting silica based ordered mesoporous materials: medical applications. *Journal of Materials Chemistry* **2006,** *16* (1), 26-31.

76. Li, Y. Y.; Cunin, F.; Link, J. R.; Gao, T.; Betts, R. E.; Reiver, S. H.; Chin, V.; Bhatia, S. N.; Sailor, M. J., Polymer replicas of photonic porous silicon for sensing and drug delivery applications. *Science* **2003,** *299* (5615), 2045-2047.

77. Zhang, J.; Dong, J. H.; Luo, M.; Xiao, H.; Murad, S.; Normann, R. A., Zeolite-fiber integrated optical chemical sensors for detection of dissolved organics in water. *Langmuir* **2005,** *21* (19), 8609-8612.

78. Stewart, M. P.; Buriak, J. M., Chemical and biological applications of porous silicon technology. *Advanced Materials* **2000,** *12* (12), 859-869.

79. Yerokhov, V. Y.; Melnyk, II, Porous silicon in solar cell structures: a review of achievements and modern directions of further use. *Renewable & Sustainable Energy Reviews* **1999,** *3* (4), 291-322.

80. Rolison, D. R., Catalytic nanoarchitectures - The importance of nothing and the unimportance of periodicity. *Science* **2003,** *299* (5613), 1698-1701.

81. Jain, A.; Rogojevic, S.; Ponoth, S.; Agarwal, N.; Matthew, I.; Gill, W. N.; Persans, P.; Tomozawa, M.; Plawsky, J. L.; Simonyi, E., Porous silica materials as low-k dielectrics for electronic and optical interconnects. *Thin Solid Films* **2001,** *398*, 513-522.

82. Weiss, S. M.; Haurylau, M.; Fauchet, P. M., Tunable photonic bandgap structures for optical interconnects. *Optical Materials* **2005,** *27* (5), 740-744.

83. Tiefenthaler, K.; Lukosz, W., Sensitivity of grating couplers as integrated-optical chemical sensors. *Journal of the Optical Society of America B-Optical Physics* **1989,** *6* (2), 209-220.

84. Lukosz, W., Principles and sensitivities of integrated optical and surface-plasmon sensors for direct affinity sensing and immunosensing. *Biosensors & Bioelectronics* **1991,** *6* (3), 215-225.

85. Sipe, J. E.; Becher, J., Surface-energy transfer enhanced by optical cavity excitation - a pole analysis. *Journal of the Optical Society of America* **1982,** *72* (2), 288-295.

86. Lugo, J. E.; delRio, J. A.; TaguenaMartinez, J., Influence of surface coverage on the effective optical properties of porous silicon modeled as a Si-wire array. *Journal of Applied Physics* **1997,** *81* (4), 1923-1928.

87. Lugo, J. E.; Lopez, H. A.; Chan, S.; Fauchet, P. M., Porous silicon multilayer structures: A photonic band gap analysis. *Journal of Applied Physics* **2002,** *91* (8), 4966-4972.

88. Ouyang, H.; Striemer, C. C.; Fauchet, P. M., Quantitative analysis of the sensitivity of porous silicon optical biosensors. *Applied Physics Letters* **2006,** *88* (16), 163108.

89. Jiao, Y.; Rong, G.; Weiss, S. M., Porous waveguide in the Kretschmann configuration for small molecule detection. *Proceedings of SPIE* **2009**, 7322, 732205.

90. Wei, X.; Kang, C.; Liscidini, M.; Rong, G.; Retterer, S. T.; Patrini, M.; Sipe, J. E.; Weiss, S. M., Grating couplers on porous silicon planar waveguides for sensing applications. *Journal of Applied Physics* **2008,** *104* (12), 123113.

91. Steinem, C.; Janshoff, A.; Lin, V. S. Y.; Volcker, N. H.; Ghadiri, M. R., DNA hybridization-enhanced porous silicon corrosion: mechanistic investigators and prospect for optical interferometric biosensing. *Tetrahedron* **2004,** *60* (49), 11259-11267.

92. Jiao, Y.; Weiss, S. M., Enhanced PNA detection sensitivity based on polymer-cladded porous silicon waveguide. *Proceedings of SPIE,* **2010**, 7553, 75530O.

93. Lawrie, J. L.; Jiao, Y.; Weiss, S. M., Size-Dependent Infiltration and Optical Detection of Nucleic Acids in Nanoscale Pores. *IEEE Transactions on Nanotechnology* **2010,** *9* (5), 596-602.

94. Wokaun, A., Surface-enhanced electromagnetic processes. *Solid State Physics-Advances in Research and Applications* **1984,** *38*, 223-294.

95. Xu, Z. D.; Chen, Y.; Gartia, M. R.; Jiang, J.; Liu, G. L., Surface plasmon enhanced broadband spectrophotometry on black silver substrates. *Applied Physics Letters* **2011,** *98* (24), 241904.

96. Westcott, S. L.; Oldenburg, S. J.; Lee, T. R.; Halas, N. J., Formation and adsorption of clusters of gold nanoparticles onto functionalized silica nanoparticle surfaces. *Langmuir* **1998,** *14* (19), 5396-5401.

97. Westcott, S. L.; Oldenburg, S. J.; Lee, T. R.; Halas, N. J., Construction of simple gold nanoparticle aggregates with controlled plasmon-plasmon interactions. *Chemical Physics Letters* **1999,** *300* (5-6), 651-655.

98. Xue, C.; Millstone, J. E.; Li, S. Y.; Mirkin, C. A., Plasmon-driven synthesis of triangular core-shell nanoprisms from gold seeds. *Angewandte Chemie-International Edition* **2007,** *46* (44), 8436-8439.

99. Kimling, J.; Maier, M.; Okenve, B.; Kotaidis, V.; Ballot, H.; Plech, A., Turkevich method for gold nanoparticle synthesis revisited. *Journal of Physical Chemistry B* **2006,** *110* (32), 15700-15707.

100. Toderas, F.; Baia, M.; Baia, L.; Astilean, S., Controlling gold nanoparticle assemblies for efficient surface-enhanced Raman scattering and localized surface plasmon resonance sensors. *Nanotechnology* **2007,** *18*(*25*), 255702.

101. Jiao, Y.; Koktysh, D. S.; Phambu, N.; Weiss, S. M., Dual-mode sensing platform based on colloidal gold functionalized porous silicon. *Applied Physics Letters* **2010,** *97* (15), 153125.

102. Whelan, C. M.; Barnes, C. J.; Walker, C. G. H.; Brown, N. M. D., Benzenethiol adsorption on Au(111) studied by synchrotron ARUPS, HREELS and XPS. *Surface Science* **1999,** *425* (2-3), 195-211.

103. Njoki, P. N.; Lim, I. I. S.; Mott, D.; Park, H. Y.; Khan, B.; Mishra, S.; Sujakumar, R.; Luo, J.; Zhong, C. J., Size correlation of optical and spectroscopic properties for gold nanoparticles. *Journal of Physical Chemistry C* **2007,** *111*, 14664-14669.

104. Lee, S.; Hahm, M. G.; Vajtai, R.; Hashim, D. P.; Thurakitseree, T.; Chipara, A. C.; Ajayan, P. M.; Hafner, J. H., Utilizing 3D SERS Active Volumes in Aligned Carbon Nanotube Scaffold Substrates. *Advanced Materials* **2012,** *24* (38), 5261-5266.

105. Dhawan, A.; Canva, M.; Vo-Dinh, T., Narrow groove plasmonic nano-gratings for surface plasmon resonance sensing. *Optics Express* **2011,** *19* (2), 787-813.

106. Gopinath, A.; Boriskina, S. V.; Premasiri, W. R.; Ziegler, L.; Reinhard, B. M.; Dal Negro, L., Plasmonic Nanogalaxies: Multiscale Aperiodic Arrays for Surface-Enhanced Raman Sensing. *Nano Letters* **2009,** *9* (11), 3922-3929.

107. Chu, Y. Z.; Banaee, M. G.; Crozier, K. B., Double-Resonance Plasmon Substrates for Surface-Enhanced Raman Scattering with Enhancement at Excitation and Stokes Frequencies. *ACS Nano* **2010,** *4* (5), 2804-2810.

108. Wu, H. Y.; Cunningham, B. T., Plasmonic coupling of SiO2-Ag "post-cap" nanostructures and silver film for surface enhanced Raman scattering. *Applied Physics Letters* **2011,** *98* (15), 153103.

109. Li, J. J.; Fattal, D.; Li, Z. Y., Plasmonic optical antennas on dielectric gratings with high field enhancement for surface enhanced Raman spectroscopy. *Applied Physics Letters* **2009,** *94* (26), 263114.

110. Kim, S. M.; Zhang, W.; Cunningham, B. T., Photonic crystals with SiO_2-Ag "post-cap" nanostructure coatings for surface enhanced Raman spectroscopy. *Applied Physics Letters* **2008,** *93* (14), 143112.

111. Delfan, A.; Liscidini, M.; Sipe, J. E., Surface enhanced Raman scattering in the presence of multilayer dielectric structures. *Journal of the Optical Society of America B-Optical Physics* **2012,** *29* (8), 1863-1874.

112. Jiao, Y.; Ryckman, J. D.; Rodriguez, G. A.; Weiss, S. M., Guided mode enhanced Raman scattering on porous silicon resonant structures functionalized with gold nanoparticles. (*In preparation*)

113. Gartia, M. R.; Xu, Z. D.; Behymer, E.; Nguyen, H.; Britten, J. A.; Larson, C.; Miles, R.; Bora, M.; Chang, A. S. P.; Bond, T. C.; Liu, G. L., Rigorous surface enhanced Raman spectral characterization of large-area high-uniformity silver-coated tapered silica nanopillar arrays. *Nanotechnology* **2010,** *21* (39), 395701.

114. Lang, X. Y.; Qian, L. H.; Guan, P. F.; Zi, J.; Chen, M. W., Localized surface plasmon resonance of nanoporous gold. *Applied Physics Letters* **2011,** *98* (9), 093701.

115. Liu, H. W.; Zhang, L.; Lang, X. Y.; Yamaguchi, Y.; Iwasaki, H. S.; Inouye, Y. S.; Xue, Q. K.; Chen, M. W., Single molecule detection from a large-scale SERS-active $Au_{79}Ag_{21}$ substrate. *Scientific Reports* **2011,** *1*, 112.

116. Ryckman, J. D.; Liscidini, M.; Sipe, J. E.; Weiss, S. M., Direct Imprinting of Porous Substrates: A Rapid and Low-Cost Approach for Patterning Porous Nanomaterials. *Nano Letters* **2011,** *11* (5), 1857-1862.

117. Jiao, Y.; Ryckman, J. D.; Ciesielski, P. N.; Escobar, C. A.; Jennings, G. K.; Weiss, S. M., Patterned nanoporous gold as an effective SERS template. *Nanotechnology* **2011,** *22* (29), 295302.

118. Xia, L. X.; Jia, Y.; Liu, G. Y.; Yang, Z. L.; Chen, X. W.; Zhang, H. L.; Sun, M. T., Adjustment and control of SERS activity of metal substrates by pressure. *Journal of Raman Spectroscopy* **2010,** *41* (4), 398-405.

119. Perney, N. M. B.; Baumberg, J. J.; Zoorob, M. E.; Charlton, M. D. B.; Mahnkopf, S.; Netti, C. M., Tuning localized plasmons in nanostructured substrates for surface- enhanced Raman scattering. *Optics Express* **2006,** *14* (2), 847-857.

120. Walczak, M. M.; Alves, C. A.; Lamp, B. D.; Porter, M. D., Electrochemical and x-ray photoelectron spectroscopic evidence for differences in the binding-sites of alkanethiolate monolayers chemisorbed at gold. *Journal of Electroanalytical Chemistry* **1995,** *396* (1-2), 103-114.

121. Wan, L. J.; Noda, H.; Hara, Y.; Osawa, M., Effect of solution pH on the structure of a 4-mercaptopyridine monolayer self-assembled on Au(111). *Journal of Electroanalytical Chemistry* **2000,** *489* (1-2), 68-75.

122. Jiao, Y.; Ryckman, J. D.; Koktysh, D. S.; Weiss, S. M., Controlling the surface enhanced Raman scattering on grating-type patterned nanoporous gold. *Nanoscale* (under review).

123. Ayas, S., Raman enhancement on a broadband meta-surface. *ACS Nano*, **2012**, *6* (8), 6852-6861.

124. Neviere, M.; Reinisch, R., Electromagnetic study of the surface-plasmon-resonance contribution to surface-enhanced Raman-scattering. *Physical Review B* **1982,** *26* (10), 5403-5408.

125. Stiles, P. L.; Dieringer, J. A.; Shah, N. C.; Van Duyne, R. R., Surface-Enhanced Raman Spectroscopy. In *Annual Review of Analytical Chemistry*, Annual Reviews: Palo Alto, **2008**, 1, 601-626.